Manuscript wcd-2019-3

'Potential vorticity structure of embedded convection in a warm conveyor belt and its relevance for the large-scale dynamics'

Oertel, A., Boettcher, M., Joos, H., Sprenger, M., and Wernli, H.

Response to reviewers

We would like to thank both reviewers, Florian Pantillon and Jeffrey Chagnon, very much for their positive, detailed and constructive feedback that helped to further improve the quality of this manuscript. We tried to address all the comments by the reviewers. The major changes in the revised version of the manuscript are the following:

1. We restructured the introduction and parts of the results section and streamlined the text to improve its quality and to avoid jumping between figures too often.

2. We added a new overview figure to introduce the WCB case study (in geographical coordinates) and its embedded convection to avoid too many references to Oertel et al. (2019) and to improve the flow of the manuscript. Additionally, we included two animations of PV at 320 K and the detailed WCB trajectory ascent in the online supplementary material.

3. The quality of the figures (essentially former Figs. 6 and 8) was improved.

4. After careful consideration of the structure, we combined (former) sections 4 and 5 to avoid repetitions and to streamline the text. Moreover, we changed the order of sections 3.1-3.4 to streamline and simplify the structure.

5. We added additional explanations in section 4 about the use of offline trajectories and our interpretation of the influence of the negative PV band on the larger-scale flow. A general comment by Florian Pantillon concerned the analysis of only one example in former section 5. Our conclusions are based on the analysis of several of such PV dipole bands (which are, however, not shown in the manuscript). We provided two more examples in this document (Figs. 3 and 4 in this document) and mention it in the revised manuscript. We now also discuss the limitations of our analysis more clearly.

6. Finally, we slightly restructured the discussion and added a new figure in the discussion section that schematically outlines the concept of the interaction of the negative PV band with the upper-level trough.

Below are the detailed replies to the individual comments.

1 Response to Jeffrey Chagnon

Comments to the author

General comments

1. General comment 1
   The headlining results in this paper concern the different behavior of convective versus slantwise trajectories. It is presumed that the convective nature of one group of particles is responsible for the deeper, larger-amplitude, coherent PV structures that accompany those particles. I would like to offer an alternative perspective for the authors to consider. In addition to being distinguished by their rate of ascent, the two groups of trajectories are also located in different regions of the WCB at their time of maximum ascent; specifically, the convective particles are located equatorward of the slantwise particles. The environments in which these two groups of particles ascend may therefore be different. Could the differences in environmental shear be primarily responsible for the different PV dipole structures? Is it possible that the shear vector is oriented parallel to the front on the equatorward end of the front, whereas the shear vector is directed across the front on the poleward end? If so, then the PV dipoles should straddle the front on the equatorward end, whereas on the poleward end of the front they should be oriented along the front. According to this view, when compositing is performed, the dipoles on the equatorward side should retain a large amplitude PV dipole structures since there is less variance in the cross-frontal structure. On the other hand, the dipoles on the poleward side are subject to interference from neighboring dipoles along the front, resulting in a weaker PV structure in the composites. I suspect that the convective nature of the particles and the environmental shear are both important in determining the amplitude and structure of the PV anomalies.

   Reply Thanks for providing this alternative perspective on the PV signature of the slantwise WCB trajectories. While we agree that environmental shear is crucial to determine the amplitude, structure and orientation of the PV anomalies, we think that for the case of "Vladiana" the wind shear is not the relevant mechanism causing the observed differences between both categories. The analysis of the vertical wind shear profiles (Fig. 1 in this document) suggests that both the magnitude of the vertical wind shear and its direction are not substantially different for the ascent regions of the convective and the slantwise WCB trajectories. We rather think that in this case, the horizontal heating gradients ($\nabla_h \dot{\theta}$) are weaker for the slantwise WCB trajectories compared to the convective WCB trajectories because the rapid and localized convective ascent leads to more localized and stronger horizontal diabatic heating maxima (in agreement with the very localized increased hydrometeor production). The larger-scale slantwise WCB ascent, in contrast, produces weaker horizontal heating gradients. We added the direction of the vertical wind shear vector in the revised manuscript (green arrows in Fig. 7c,d in the revised manuscript).

2. General comment 2
   While I agree with the authors contention that the horizontally-oriented PV dipoles are most likely due to heating in the presence of background shear (e.g. Figure

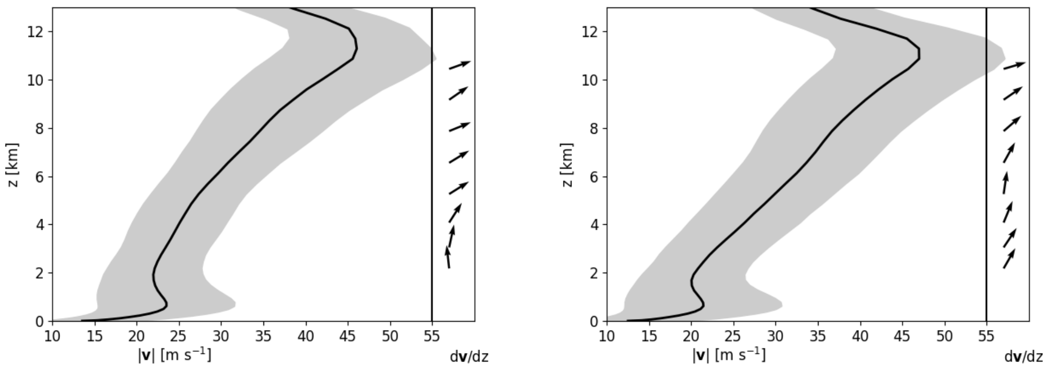

Figure 1: Vertical wind speed profile (mean and standard deviation) and direction of standardized vertical wind shear vector at selected altitudes for **(a)** the convective WCB trajectories 30 minutes and **(b)** the slantwise WCB trajectories 6 hours after the start of their fastest ascent phase.

1), an alternative explanation for the structures (e.g., in Fig. 6e) is that they are associated with a vertically-oriented dipole in PV tendency that is subject to non-linear advection in the cross-frontal plane that results in the horizontally-oriented dipoles in total PV that we see. Have the authors examined either the PV tendencies or the cross-frontal advection to eliminate this possibility?

Reply Thanks for providing this alternative perspective. Unfortunately, we cannot output the PV tendencies in our simulation and we did not specifically consider the cross-frontal circulation. Nevertheless, we believe that the described mechanism of the formation of the horizontally-oriented PV dipoles due to heating in the presence of background shear is the relevant mechanism in this case due to the following two reasons: On the one hand, a recent study by Harvey et al. (2020) has theoretically deduced that the vertical components of the PV tendency equation cannot form negative PV (only decrease PV). Thus, the horizontal components are essential to form absolute negative-PV air (in contrast to just a negative PV anomaly). On the other hand, the analysis of the standard deviation of PV for the convective updrafts shows that the standard deviation is largest in the vertical column directly centered at the convective updraft (Fig. 2 in this document), where the ascent strongly modifies PV and large-amplitude PV anomalies occur. This suggests that there the PV modification is strongest, because small differences in the shape, widths, and intensity of the individual convective updrafts and small spatial displacements of the exact position of the individual PV dipoles result in a large standard deviation (see also reply to specific comment 1). In contrast, if the PV dipoles were to be formed by the cross-frontal advection of vertical PV dipoles, we would expect also a larger standard deviation in the region where the PV poles are supposed to be advected (i.e., more to the right and left of the convective updraft). Moreover, we are not sure, why the cross-frontal advection of vertical PV dipoles is supposed to form the horizontal PV dipoles and does not further distort the shape of the PV anomalies.

Specific comments

1. In addition to calculating the composite mean maps, have the authors analyzed the variance? Variance maps could establish whether the mean maps are robust. For example, where the composite mean amplitude is large but the variance is low, the mean fields could be considered robust.

   Reply We computed the standard deviation (Fig. 2 in this document), however, interpret the signal differently. We agree, that theoretically, one would expect a lower standard deviation for a robust signal. However, in the high-resolution 2-km simulation, the PV field is extremely patchy and fragmented (e.g., Figs. 9e and 10b in the manuscript); each individual PV dipole is slightly different, and only a small displacement of the exact convective WCB trajectory position in the vertical or the horizontal can result in large differences in the grid-point PV field between two individual convective PV dipoles (see also reply to general comment 2). We rather assume that the enhanced standard deviation directly at the center of the convective ascent is an indication that there very strong and localized PV gradients arise due to the localized diabatic heating. We think that generally one can expect a stronger standard deviation of PV in the region where the "action takes place", i.e., where strong diabatic PV modification occurs. In contrast, the surroundings of the convective ascent are characterized by lower standard deviation as only weak PV modification takes place. Thus, we think that the presence of the distinct coherent PV dipole field centered around the convective ascent - despite the very fragmented instantaneous PV fields - is a robust signal. In particular, because at such a high resolution each individual convective updraft (which each also vary in shape and size) is accompanied by a slightly differing PV structure, resulting in increased grid-point variability.

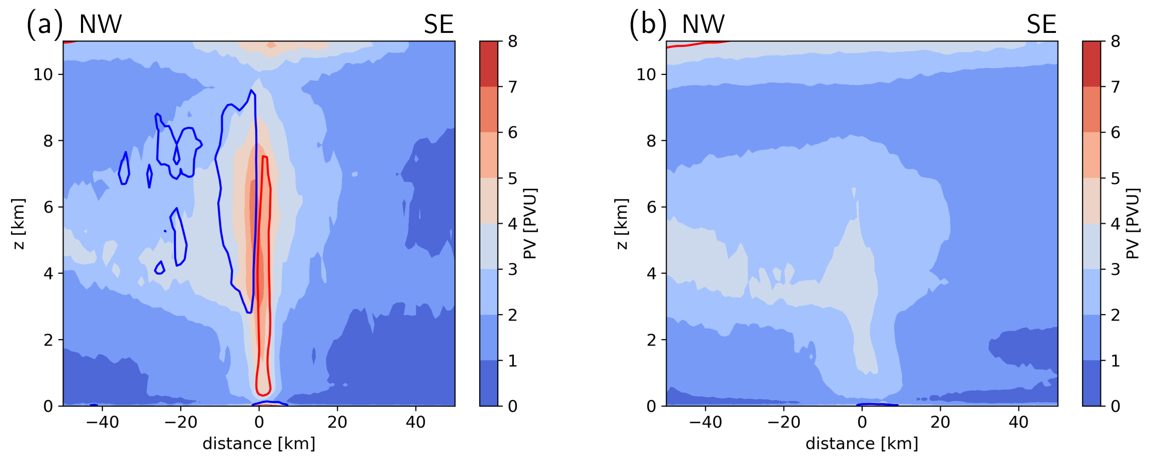

Figure 2: **(a,b)** Northwest-southeast oriented vertical cross-section composite of PV (blue and red lines at 0 PVU and 2 PVU, respectively) and its standard deviation (colors, in PVU) for **(a)** convective WCB trajectories 30 minutes and **(b)** slantwise WCB trajectories 60 minutes after the start of the fastest ascent.

2. Figure 2 gives the impression that there is a large separation in time and space between the slantwise and convective particles, but the figure only shows the times and

locations of maximum ascent. At any fixed time, would these groupings of particles occupy distinct regions of the WCB, or are they distributed more uniformly?

Reply The convective WCB trajectory positions at the presented times in Fig. 2 are directly embedded within the regions where also slantwise WCB ascent takes place. Unfortunately, this is difficult to see as convective and slantwise WCB trajectories directly coincide frequently (l. 241 ff. "Despite the differing ascent behaviour between both WCB categories, the convective WCB ascent is directly embedded in the region of large-scale ascent in close proximity to the more slowly ascending WCB trajectories, indicating that although their ascent rates differ, both WCB categories are not distinctly spatially separated"). However, the slantwise WCB trajectories occupy in general a wider region in the warm sector than the convective WCB trajectories and they occur during a longer time period (see Fig. 1b). For clarification, we added the mean latitude of convective and slantwise WCB ascent in the manuscript ["The convective WCB trajectories start their ascent on average slightly further southward at the cold front ($45.2° \pm 3°$) compared to the slantwise WCB trajectories whose ascent region extends further poleward ($47.7° \pm 4°$), but the overall region of origin overlaps (Fig. 2) and the convective WCB ascent is indeed embedded in the region of slower WCB ascent."]. After the start of the fastest ascent, the convective WCB trajectories ascend very rapidly through the entire troposphere, i.e., they reach the upper troposphere further south compared to the slantwise WCB trajectories. Thus, with respect to the first arrival in the upper troposphere, the location of convective versus slantwise WCB ascent differs.

3. Does the 2000 to 7000 split in the number of convective versus slantwise particles imply that 3.5 times more mass ascends slantwise?

   Reply All WCB trajectories should approximately represent equal mass. However, it is difficult to state explicitly that 3.5 times more mass ascends in a slantwise than a convective way, due to the selection criteria we applied. We specifically selected the 10% fastest ascending WCB trajectories for the convective category (cf. section 2c), while for the slantwise WCB trajectories we selected trajectories with ascent rates between the 25^{th} and 75^{th} percentiles. Consequently, a subset of WCB trajectories that ascends rapidly (but more slowly than the 10% fastest ones) exists, and furthermore, the slowest ascending WCB trajectories (which are also considered as slantwise) are also not considered in the composite analysis. However, the compositing technique requires the selection of trajectories with a coherent ascent behaviour to not smear out the signals.

4. In Figure 5c, it is very difficult to distinguish the thick black lines from the thick blue lines.

   Reply Thanks for the comment, we adjust this figure (see also reply to comment 50 to Florian Pantillon).

5. Line 277. Should SWC and RWC be swapped?

   Reply Yes, thank you very much for spotting this typo!

6. Line 426. "is" $\rightarrow$ "are"? (or make "hydrometeors" singular?)

   Reply We corrected this, thank you.

2 Response to Florian Pantillon

Comments to the Author

General comments

1. General comment 1
   Unlike the systematic analysis of convective ascents based on composites, the impact on the large scale is investigated based on a single convective PV dipole band, is rather qualitative and uses offline instead of online trajectories. Either extend toward a more quantitative framework, e.g. also based on composites, or at least carefully discuss the results and implications throughout the paper (including in title and abstract) considering these limitations.

   Reply Thanks for the comment. The conclusions drawn from the illustration of the large-scale impact is derived from the analysis of several of such larger-scale PV dipole bands, which are consistently approaching the waveguide and coincide with an accelerated jet. We did not specifically mention this in the submitted manuscript, but will mention this in the revised version. Moreover, we will also discuss these limitations more carefully. Two additional examples of the propagation of these PV dipole bands are provided here for your information (Figs. 3 and 4 in this document). We think that for the larger-scale PV dipoles a composite analysis is not meaningful, because (i) the PV dipoles all have a different size, (ii) they occur at differing distances to the jet, and (iii) the propagation towards the waveguide strongly distorts the negative PV features which results in different shapes and sizes of the negative PV features. Thus, a composite analysis would smear out the signals, especially the formation of sharp boundaries, such as the enhanced isentropic PV gradient.

2. General comment 2
   The "big picture" is diluted in the introduction: the contrast between small and large scale is clear but what is referred to as mesoscale? There is a confusion between isolated cells and organized convection, and embedded convection needs a proper definition (from the example in Fig. 8 it appears to develop along the cold front only). Citations need to be revised and the organization should be improved (see next comment).

   Reply Thanks for your suggestion, we restructured the introduction, revised the references, and tried to be more explicit about the differences between individual convective cells and organized convection. We added an overview figure to show the occurrence of embedded convection (new Fig. 2 in the revised manuscript), which hopefully helps to better understand WCB-embedded convection and its occurrence in this WCB case study. Moreover, section 2 provides details about the used criteria to select the convective WCB trajectories.

3. General comment 3
   Theoretical considerations on PV production need reorganization: they appear too early in the introduction and are largely repeated in sections 3.4.3 and 3.4.4. Consider moving the detailed PV discussion to a short theoretical section, which could

later be referred to. Some elements may be moved from the discussion section and grouped with either the introduction or the theoretical considerations.

Reply Thanks for the comment on the structure of the theoretical considerations. We agree and restructured the introduction following your suggestions and adjust the theoretical considerations in the results sections accordingly. We still would like to keep the theoretical explanation in the results section to highlight the similarities between our results and theory. This paragraph (l. 380-390 in the revised manuscript), however, was revised and is more concise. In particular, we strengthened the link between our results and theory.

4. General comment 4
Most of the paper is based on composites of Lagrangian trajectories, which is a very interesting approach but may look abstract to the reader; sometimes a figure in geographical coordinates would be helpful. Placed earlier, section 4 would well introduce the case study and illustrate the different concepts that are developed in sections 3 and 5, thus remove the need to constantly refer to Oertel et al. (2019) and to Fig. 8(d) early in the paper.

   Reply Thanks for your suggestions. We agree that it is problematic to often refer to Oertel et al. (2019) in the introduction of the case study. Thus, we added a figure in geographical coordinates to introduce the WCB case study and to illustrate the occurrence of embedded convection and the associated upper-level PV field (Fig. 2 in the new manuscript). This also removes the need to refer to Fig. 8d too early in the manuscript. We believe that the placement of section 4 in the beginning is not meaningful because the reader has not yet been explicitly familiarized with the concept of PV dipole formation (see also reply to comment 81). Thus, the identification and detection of the coherent PV dipole features in the fragmented PV field in Figs. 8d and 9b is rather difficult. Moreover, due to the patchy PV structure, the argument of the coherent dipole signature for convective WCB ascent might not be convincing before the composite analysis. In contrast, after the composite analysis, the reader has already been familiarized with the PV dipole structure and the signal arising from WCB-embedded convection has already been established previously. Moreover, the illustrative example serves as an introduction and transition to (former) section 5 ("PV anomalies on a larger scale and relevance for large-scale dynamics"). After careful consideration, we combined sections 4 and 5 (see also general author comment 4), and for clarification, we added a statement at the beginning of section 4 that this example will further be discussed in the following sections.

5. General comment 5
The text contains several repetitions and frequently jumps back and forth between figures. In addition, it often refers to Oertel et al. (2019) and other papers to explain results, which creates a confusion between what is expected from previous work and what is actually found here. Please streamline and clarify to improve the flow.

   Reply Thanks for your comment, we tried to improve the structure and avoid to jump between figures as much as possible. Moreover, the integration of the additional overview figure (see also reply to general comment 2 and 4) will remove the need to refer to Oertel et al. (2019) too often.

Specific comments

1. l. 4-5 not sure this sentence is needed

   Reply We would like to keep this sentence to emphasize that the impacts of embedded convection have not previously been analysed and to highlight the novelty of this study.

2. l. 8-10 the sentence somehow suggests that graupel is part of surface precipitation

   Reply We clarified this by adding "and the formation of graupel in the upper troposphere".

3. l. 11 what does "they" refer to?

   Reply We replaced "they" by "the convective WCB trajectories" for clarification.

4. l. 17 perhaps insist on negative PV values? (not just anomaly)

   Reply We added PV "values" to this sentence.

5. l. 17-19 this is speculative, as only one example is presented

   Reply We specifically included "can". Moreover, we added later in the manuscript that this process can be seen several times in this case study (see also reply to general comment 1): "The formation of these PV dipole bands on either side of elongated convective ascent regions can be observed at various times ahead of the upper-level trough in this WCB case study (not shown)." Besides, the limitations of our analysis are more carefully discussed in the revised manuscript.

6. l. 21-23 this is also speculative, for the same reason

   Reply This sentence directly refers to the example that is shown in the manuscript ("An illustrative example of such a convectively generated ..."). We also use the word "can" to emphasize that the described process does not necessarily occur in differing synoptic situations. In the conclusions, this is also carefully stated: "On the larger-scale, the individual mesoscale PV dipoles can, *in certain synoptic situations as in this case*".

7. l. 27 "their"?

   Reply "their" was supposed to refer to "extratropical cyclones". We slightly changed this sentence to "Moist diabatic processes are known to play an important role for the evolution of extratropical cyclones".

8. l. 29 The two references are not clearly related to moist diabatic processes in extratropical cyclones.

   Reply This sentence was slightly changed (see also comment above) to focus more generally on moist diabatic processes.

9. l. 35 "potentially affect": better "can affect"?

   Reply We changed "potentially affect" to "can affect".

10. l. 23-25 this basically repeats what is written above; what are broader implications of the study?

    Reply We added some potential broader implications: "They thus can be dynamically relevant, influence the jet stream and potentially the downstream flow evolution, which are highly relevant aspects for medium-range weather forecast." Additional broader implications are discussed in more detail in the discussion section. In the abstract, we would like to focus on the specific results from this study.

11. l. 37 The transition from general WCB dynamics to precise PV theory is abrupt.

    Reply Thanks, we agree. We changed the structure of the introduction and moved the PV theory in a separate subsection later in the introduction (see also reply to general comment 2 and 3).

12. l. 42 Please define terms in brackets (or omit).

    Reply We added the definitions for all terms.

13. l. 46 Please define f, zeta and theta_dot.

    Reply We added the definition of theta_dot; f and zeta are now defined previously in the revised manuscript.

14. l. 47-49 This sounds very similar to l. 34-36.

    Reply Thanks, this has been modified during the restructuring of the introduction.

15. l. 51 The first two references do not mention mesoscale convective systems.

    Reply Thanks for spotting this mistake, they do not belong there and were removed.

16. l. 52 What are "convective storms"? (vs. MCS above)

    Reply We use the word "convective storms" (cf. Chagnon and Gray, 2009) to contrast individual convective cells from the larger mesoscale convective systems. To avoid confusion, we replaced it with "at the scale of individual convective cells".

17. l. 58-59 Is this not what has just been stated in l. 53-57?

    Reply This sentence has been removed.

18. l. 61 The horizontal vorticity vector w_h must be defined when it is introduced first.

    Reply Thanks, we included the definition of w_h.

19. l. 60-63 This process is not obvious and requires more details. I appreciate it is supported by a schematic but I do not exactly understand what is what in Fig. 1. Can you make the schematic more reader-friendly, e.g. by illustrating why the vectors are oriented as they are, using more explicit colors and referring to them in the text?

    Reply Thanks for this helpful comment. We adjusted the schematic, revised the text and more explicitly refer to the colors in the text.

20. l. 71-75 There is a confusion between negative PV, the different types of instabilities and their consequences. Schultz and Schumacher (1999) rather discuss conditional symmetric instability, which is another type of (slantwise) instability.

    Reply It is true that Schultz and Schumacher (1999) elaborate on CSI, however, they also provide an overview of the other types of (dry) instabilities related to negative PV. Nevertheless, we removed this reference.

21. l. 79 "observed" is not the appropriate word for model data. Better "found"?

    Reply We replaced "observed" by "found".

22. l. 81-93 This general paragraph would rather better appear before the previous, more specific one.

    Reply We restructured the introduction such that l. 81-93 appear before the detailed PV modification section (see also general comment 3).

23. l. 87 The cited studies use very different types of "remote-sensing data". More specifically?

    Reply We think that for the purpose of this study it is not relevant to specify the types of remote-sensing data that were used in the mentioned studies. For your information, Binder (2016) and Crespo and Posselt (2016) used radar observations and retrievals from the polar-orbiting CloudSat satellite, while Flaounas et al. (2016) used microwave measurements from the NOAA-18 and 19 satellites and Flaounas et al. (2018) combined microwave diagnostics from several different satellites.

24. l. 89-93 There is a confusion between what impact and which study relates to WCB or convective systems. Furthermore, the link with forecast errors would better fit with the modification of the large-scale flow in the first paragraph.

    Reply We modified this paragraph during the restructuring of the introduction.

25. l. 94-114 Rather than pointing what has not been done yet and focusing on very precise questions, this part would better motivate the study if it would emphasize what are open questions (e.g., contribution of embedded convection to WCB dynamics), why they are important (e.g., reconcile small- and large-scale views) and how they are addressed here (e.g., convection-permitting simulations of a case study).

    Reply The introduction section has been restructured and we included some open questions. The applied methodology (e.g., convection-permitting simulations of a case study) is als included in this paragraph.

26. l. 94 MCSs are not just "individual convective updrafts".

    Reply Thanks, we are aware that MCS are not just "individual convective updrafts". This sentence was supposed to refer mainly to studies actually related to the analysis of individual convective cells (e.g., Chagnon and Gray, 2009; Weijenborg et al., 2015, 2017). However, we realised that in the context this might be misleading. Hence, we added "Previous studies analysed the PV modification by individual convective updrafts *and mesoscale convective systems*".

27. l. 116 which case study?

    Reply We added "analysed" case study. Moreover, we added a statement earlier that states that this study analyses specifically one case study.

28. Past and present tenses are often mixed in this Section, please stick to one or the other.

    Reply We corrected this, thank you.

29. l. 123 is it the same setup or the same simulation?

    Reply It is the same setup but a different simulation (because this analysis requires a higher temporal resolution of the 3D fields, i.e., every 15 minutes).

30. l. 125 "grid spacing" rather than "resolution".

    Reply We replaced "resolution" by "grid spacing".

31. l. 142-158 It is difficult to get a general picture of the cyclone evolution without reading Oertel et al. (2019). A graphical summary would be helpful, e.g. by adding the cyclone track (and the upper-level trough) on Fig. 2(a).

    Reply Thanks, we agree. Hence, we added a new figure (new Fig. 2 in the revised manuscript) to better introduce the WCB case study (see also reply to general comments 4 and 5) to show the temporal evolution of the cyclone, the WCB ascent and the according upper-level PV structure in geographical coordinates. We will include the previously mentioned animations (see general comment 2 in the beginning of the manuscript) to show the evolution of the cyclone and the WCB.

32. l. 142 explicit NAWDEX

    Reply We changed it to "North Atlantic Waveguide and Downstream Impact EXperiment".

33. l. 150 more than 400 or 600 hPa?

    Reply The ascent rates exceed 400 hPa and sometimes even 600 hPa in 2 h.

34. l. 156-157 this last sentence is unnecessary

    Reply We would like to keep this sentence because we think that it is helpful to state that – despite the continuous distribution of ascent rates – two distinct categories of WCB trajectories can be meaningfully selected for the analysis.

35. l. 163-166 Why combine two criteria? (400 hPa in 1 h and 600 hPa in 3 h) Is a fast ascent (top 10%) sufficient to be considered "convective"?

    Reply To get a coherent signal in the composite analysis, the selected trajectories are required to show a similar ascent behaviour and cannot diverge too much during their ascent; otherwise any signals along the ascent would be smeared out. Due to the very diverse ascent behaviour of all (convective) online WCB trajectories, we combined the mentioned two criteria to get a coherent signal (i) in the lower troposphere at the start of fastest ascent and (ii) in the middle- to upper troposphere during the ascent and outflow phase.

We think that one distinct and fixed threshold for "embedded convection" in WCBs has not yet been defined. Rasp et al. (2016) and Oertel et al. (2019) considered a threshold of 400 hPa ascent in 2.5 hours as convective. The ascent rate criteria used for the composite analysis in this study is much higher. We consider these localized and strongly enhanced ascent rates as embedded convection (especially compared to the much slower slantwise WCB ascent), however, we also believe that there is not a fixed ascent rate threshold.

36. l. 170-172 The description is confusing: temporal evolution of what? is it really the position relative to the cold front? Where is the upper-level trough?

    Reply We show the temporal evolution of the location of the start of the fastest WCB ascent in the lower troposphere. Shown are geographical coordinates of the WCB trajectory positions for each timestep. We modified the caption for clarification. The cold frontal surface is also approximately shown, i.e., the initial ascent position of the WCB trajectories in relation to the cold front is illustrated. Moreover, we simplified the figure (see also reply to comment 119). Combined with the new Fig. 2 (evolution of the cyclone and WCB), this figure is now hopefully easier to understand. We also added the position of the cyclone center for clarification. The position of the upper-level trough can also be seen in the new Fig. 2d-f and in the online supplemental material.

37. l. 174 behind rather than "ahead of"?

    Reply The convective activity occurs ahead of the surface cold front (i.e., east of the cold front) in the warm sector (cf. Fig. 3a in the original manuscript).

38. l. 176 again, showing the cyclone position would be helpful for the general picture.

    Reply The location of the cyclone can now be seen in the new Fig. 2 that was included (see also reply to comment 31).

39. l. 183-184 what about the vertical coordinate?

    Reply The averaging of the fields for the composite analysis was performed on the original model levels, i.e., the vertical coordinate of the composites was not changed. This is (only) possible because the selected WCB trajectories (centered relative to the start of the fastest 400-hPa ascent phase) perform a very similar ascent and do not diverge too much in the vertical during their ascent. Hence, also the two ascent criteria are based on the fastest 400-hPa and 600-hPa ascent (see also reply to comment 35).

40. l. 188-189 not only the impact but also the environment of trajectories

    Reply We added this, thanks.

41. l. 190 is this shown somewhere?

    Reply This can now be seen in the new Fig. 2 and in the online supplemental material, which shows the location of (convective) WCB ascent and the according upper-level PV field.

42. l. 193-194 does it mean that circles in Fig. 2(a) are also at 00 UTC 23 and 24 Sep mainly?

    Reply The maximum number of circles indeed occurs at 00 UTC 23 and 24 Sep mainly, however, also at the times between convective ascent takes place (see Fig. 2b in the original manuscript).

43. l. 201-204 "warmer and moister region": is it really warmer? Fig. 3(a,b) does not explicitly show the contribution of theta to theta_e and Fig. 4(a,b) suggests that the difference in absolute temperature T is due to a different height. Also, some indication about how much the two composites overlap is needed, either by showing statistical significance on cross-sections at least by giving the standard deviation around mean values.

    Reply Thanks for noting this. We replaced temperature by potential temperature to overcome the mentioned issues. In addition, we also included the standard deviation for the initial θ, q_v, and θ_e in the manuscript.

44. l. 205-211 apart from highlighting low-level convergence, it seems that these lines do not add any new information to "the region is warmer and moister"; clarify or streamline.

    Reply In addition to highlighting low-level convergence and upper-level divergence, this figure shows the WCB ascent ahead of the cold front, the strong and localized θ_e gradients and their almost vertical alignment relative to the WCB ascent.

45. l. 214-215, 222-223 what about the difference in height? Is it significant?

    Reply We included the standard deviation for the distribution of WCB outflow heights in the manuscript and find that the differences are robust [10 km ($\pm$1.0 km) versus 9 km ($\pm$1.2 km)]. Besides, we performed a Welch's t-test assuming non-identical variances for the outflow heights of both WCB categories. The test suggested that the difference in means between both outflow heights is highly significant ($p \ll 0.01$).

46. l. 218-219 can you be more precise about where to find this information in Oertel et al. 2019?

    Reply It is found in Fig. 6 and section 5.1.2 in Oertel et al. (2019) (this information was added to the manuscript).

47. l. 221 "the observed rapid convective updrafts" and associated references: it sounds like a conceptual description of potential instability but not necessarily of what happens here

    Reply Thanks, we realised that the references were not ideally placed and moved them to the previous sentence. We think that this process actually happens in our case due to the combination of large potential instability and almost saturated conditions and substantial quasi-geostrophic forcing for ascent in the same region.

48. l. 222 mention somewhere the different time scale to emphasize the different ascent rate

Reply We mentioned in l. 224 that the ascent takes approximately 18 h ["In contrast, the slantwise WCB trajectories are characterized by a substantially slower ascent and perform a gradual slantwise ascent until they reach their final outflow level at, on average, 9 km ($\pm$ 1.2 km) height after approximately 18 h, after an initially swift ascent (due to the centering relative to the fastest 400-hPa ascent) in the lower troposphere.", l. 225ff in the revised manuscript]. Moreover, the figure caption includes an according statement: "Note the different time axis in (a,c,e) and (b,d,f)." Finally, we slightly restructured the results section to emphasize the different ascent rates earlier in the manuscript.

49. l. 226-228 can you be more precise by giving a value of attained height (average+/-std)

    Reply In the manuscript we added the standard deviations for the outflow heights for both WCB categories (see also reply to comment 45).

50. l. 230 Please design new panels for the time evolution of surface precipitation in Fig.5; panels (c,d) are already very busy and mixing vertical profiles with a scalar value is extremely confusing. It should also be mentioned somewhere that (a,b) are instantaneous values taken at the respective time of max surface precipitation.

    Reply Thanks for the suggestions; the figure was improved accordingly.

51. l. 236 "comparatively thick cirrus cloud" compared to what?

    Reply The word "comparatively" was misleading and was removed.

52. l. 237 turquoise contours?

    Reply Yes, thank you.

53. l. 237-241 it is unclear how the cirrus cloud related to convection, as its core is located well above the composite trajectory; is it due to a fraction of faster-ascending trajectories?

    Reply The cirrus cloud above the convectively ascending WCB trajectories is not necessarily formed by the trajectories themselves, but due to mass conservations, the air above the convective ascent region also has to be lifted which subsequently leads to the formation of the upper-level cirrus cloud and the locally elevated cloud top. The formation of (in situ) cirrus clouds above the actual WCB trajectories can also be seen for the slantwise WCB ascent. Previous studies showed that the formation of in situ cirrus clouds is a common feature above the WCB [cf. Spichtinger et al. (2005), ACP and Wernli et al. (2016), GRL]. Nevertheless, some of the trajectories also ascend to higher altitudes, which is however not the main reason for the high ice water content above the convective and slantwise WCB trajectories.

54. l. 243-244 "horizontally more homogeneous": can this really be seen in time-height plots?

    Reply We concluded that, as the slantwise WCB ascent extends over a long distance, the homogeneity in the time-height plot can be also transferred to horizontal homogeneity. As this statement could be misleading, we removed it.

55. l. 246-247 this is interesting indeed, but may it be due to the compositing process, or are there actual profiles where ice water extends above the tropopause level?

    Reply Thanks for this comment. We removed this statement because we can indeed not rule out that to some extent this signal arises from the compositing process. We checked individual instantaneous cross-sections, which reveal that only a fraction of convective WCB trajectories effectively contributes to the moistening of the lowermost stratosphere. Figure 5 in this document shows an example where the ice water content above the dynamical 2 PVU tropopause exceeds $0.05\,\mathrm{g\,kg^{-1}}$.

56. l. 251-253 this largely repeats what is written above and is thus unnecessary

    Reply We removed this part.

57. l. 255-256 number of trajectories starting their ascent at that time?

    Reply Yes, we show the number of WCB trajectories that start their ascent and specified this in the revised manuscript. As the maximum surface precipitation occurs approximately 30 minutes and 1 h after the start of the convective and slantwise WCB trajectories, respectively, the time lag between the precipitation and the number of trajectories is at most 1 h.

58. l. 256 is the precipitation area roughly constant, i.e., are variations in Fig. 2(b) due to variations in intensity or in concentration?

    Reply For the computation of the domain-averaged precipitation, we only considered precipitating grid points (the number of precipitating grid points does not vary very much), i.e., it is predominantly an intensity effect. The pattern is very similar if either the precipitation sum in the domain or the domain-averaged precipitation including non-precipitating regions are considered.

59. l. 257 "Nevertheless": furthermore?

    Reply We replaced "Nevertheless" with "In particular".

60. l. 258-259 what is the citation here needed for? Clarify or omit

    Reply Oertel et al. (2019) also showed that embedded convection can influence the surface precipitation pattern, but with a different methodology. We specified where to find this information in Oertel et al. (2019).

61. l. 278-282 where is this effect seen in Fig. 5(c,d)?

    Reply Sorry for the confusion, we now corrected/clarified the references. The former Fig. 5 (Fig. 4 in the revised manuscript) shows the melting level, the 0°C isotherm, and the transition from the solid (SWC and GWC) to the liquid (RWC) phase. The effect on θ_e is shown in former Fig. 4 (Fig. 5 in the revised manuscript).

62. l. 286 "observed PV distribution": more specifically? Avoid "observed" if from model

    Reply We removed "observed". The resulting PV distribution is discussed in detail in the following paragraphs, hence, it does not need to be specified in this first paragraph.

63. l. 294-295 "in particular" seems to contradict "despite" above

    Reply We removed "In particular".

64. l. 301-302 why that time? (maximum precipitation rate?)

    Reply We chose this time because it coincides with the maximum hydrometeor content in the mid-troposphere (i.e., also strongest latent heat release). Hence, this time corresponds to the strongest PV modification in the mid-troposphere, and thus, to the clearest and strongest PV dipole signal. Because of this, it also coincides with the maximum precipitation rate.

65. l. 303-306 mention the different scales in (a,b) or add box of (a) in (b)?

    Reply The different spatial scales are already mentioned in the caption, and we explicitly state the dimensions also in the text (l. 302-308 in the original manuscript; l. 332ff in the revised version): "Note the different spatial dimensions for the convective and slantwise WCB trajectories."

66. l. 308-309 "as a consequence" appears to repeat "due to"

    Reply We think that the direct effect of convective WCB ascent is the stronger and more localised diabatic heating, while the PV modification is a consequence of this. Hence, we would like to keep this sentence as it is.

67. l. 317 Fig. 5(c) does not explicitly show diabatic heating

    Reply It is true that Fig. 5c does not show diabatic heating but the hydrometeor contents. However, we state in the text that the diabatic heating maximum is associated with the maximum of graupel and snow formation. We slightly modified the sentence to clarify this: "The maximum amplitude of the PV dipole occurs at about 315-320 K (Fig. 7e) and coincides with the diabatic heating maximum associated with the maximum of the formation of snow and graupel (Fig. 4c)."

68. l. 322-324 this statement appears speculative

    Reply We believe that to a large extent the patchy PV dipole pattern in the instantaneous PV field corresponds to individual convective PV dipoles, as (i) the PV dipoles mostly coincide with the convective WCB ascent region (e.g., Fig. 8d in the original manuscript), (ii) the composites show a coherent signal, and (iii) the analysis of several individual cross-sections through convective updrafts clearly shows the dipole structure (e.g., Fig. 9 a in the original manuscript).

69. l. 323 specify what to look at in Oertel et al., 2019, Fig. A1

    Reply We removed this reference, because the patchy PV field is now shown in the overview of the WCB case study (new Fig. 2d-f in the revised manuscript).

70. l. 330-332 I do not clearly see the vertical PV dipole expected in this case according to the previous sentence

    Reply Fig. 6b shows the positive low-level PV anomaly, while Fig. 6d shows the upper-level low-PV air. However, the slantwise WCB ascent does not lead to PV dipoles with a similar extent as the horizontal PV dipoles formed by convection.

Hence, the vertical PV dipole is formed by the regions of enhanced positive low-level PV and decreased upper-level PV.

71. l. 345-346 how is this shown in Fig. 7(a)?

    Reply Fig. 7a shows the enhanced low-level vorticity, not the vortex stretching. As this might be unclear, we removed the reference to the figure.

72. l. 346-350 is it an interpretation or is it really shown somewhere?

    Reply This is an interpretation based on the enhanced low-level vertical vorticity (Fig. 7a) and the rapid convective ascent leading to vertical diabatic heating gradients due to enhanced hydrometeor formation in the mid-troposphere.

73. l. 351-358 similar to above, is this shown somewhere for the composite or does it refer to the theoretical schematic only?

    Reply This refers to both the theoretical considerations and our results. In this section, we explain the formation of the convective PV dipoles in our analysis. In the revised manuscript we clarify the references to our results, which have not been stated very clearly in the original manuscript.

74. l. 359-366 This largely confirms what is explained in the introduction

    Reply We agree that this paragraph confirms the theoretical considerations, which is why we would like to keep it. It highlights that in agreement with theory the processes in the convective and the slantwise WCB trajectories differ.

75. l. 368 again, Schultz and Schumacher (1999) mainly discuss conditional symmetric instability

    Reply We removed this reference here (see also reply to comment 20).

76. l. 382-384 this partly repeats l. 373-375

    Reply We shortened these sentences to avoid the repetition.

77. l. 395-398 does it occur here? Is it shown anywhere?

    Reply Unfortunately, we cannot isolate this process, hence, this sentence remains speculative. We clarified this by stating that "In this way convective activity *could* be maintained".

78. l. 402 "is accelerated by" contradicts "hardly exceeds" above

    Reply We added that the acceleration in the composite analysis is very small. It now reads "is very slightly accelerated" to point out that the direction of the induced wind anomaly points in the same direction as the low-level jet.

79. l. 406 "PV dipoles" plural or singular?

    Reply We changed it to "PV dipole" to be more precise.

80. l. 407-409 for comparison, what is the value of the vertical shear?

    Reply The vertical wind shear amounts to approximately 2-3 $\mathrm{m\,s^{-1}\,km^{-1}}$ in the 4-12 km layer. We added a sentence about the magnitude of the wind shear in the manuscript: "In this case, the vertical wind shear vector of magnitude 2-3 $\mathrm{m\,s^{-1}\,km^{-1}}$ between 4-12 km height points in the same direction as the upper-level wind vector, i.e., towards the northeast (Fig. 7c)."

81. An illustrative example of WCB-embedded convection. The purpose of this section is unclear at that point, as it mostly repeats ideas developed in the previous section; such an "illustrative example" would better fit early in the paper to motivate the systematic analysis based on composites.

    Reply We agree that studies often first show one example before proceeding with a systematic analysis and considered the possibility to show the example earlier in our manuscript. However, we decided to still first show the results of the composite analysis before the example (see also reply to general comment 4), because (i) the described PV dipole structure is more convincing in the composite analysis compared to the one example shown, (ii) it is difficult to clearly identify the relevant pattern in the instantaneous example when it is yet unclear for the reader what exactly to look for, and (iii) it prepares the reader for the following analysis of the larger-scale impact of the negative PV (section 5). Moreover, we combined sections 4 and 5 (see general comment 4). To better bridge sections 4.1 and 4.2 and provide a rational for placing section 4 after the composite analysis, we included a sentence in the first paragraph of section 4.1 that prepares for the following analyses: "Based on this example we will discuss the lifetime of the convectively generated PV dipoles and their potential for the interaction with the larger-scale flow (section 4.2)."

82. l. 420 at 09 UTC 23 Sep 2016

    Reply The time and date were added in the sentence.

83. l. 422-423 the previous section insists on the presence of graupel to distinguish convective from slatwise ascent: display graupel here only? And does it occur along the cold front?

    Reply We state that graupel is formed during the convective ascent and is absent for the slantwise WCB ascent. However, we are not sure if the formation of graupel is necessarily required in all cases. The localized and dense cloud with increased hydrometeor content, however, clearly shows the presence of a localised convective updraft. In this example graupel is also abundant and exceeds 2 $\mathrm{g\,kg^{-1}}$ in the mid-troposphere.

84. l. 423-424 "rapidly ascending WCB trajectories": convective WCB trajectories?

    Reply We use the term "rapidly ascending trajectories" because they meet the convective ascent criterion used by Rasp et al. (2016) and Oertel et al. (2019) of more than 320 hPa in about 2 h (400 hPa in 2.5 h), but not necessarily the strict criterion used for the composite analysis in this study. The very strict criterion required for the composite analysis results in fewer WCB trajectories for each time step, which is difficult to visualize (the selected convective WCB trajectories for the composite analysis are located within these outlined regions). However, as also mentioned in reply to comment 35, the composite analysis requires very strict criteria to get a coherent signal in both the lower and upper troposphere.

85. l. 427-429 this last sentence mostly repeats what has just been stated

    Reply We shortened this sentence, however, we would like to keep the statement about the similarity between the instantaneous example and the composite analysis.

86. l. 432 is PV on the original grid or aggregated in the cross-section?

    Reply PV shown in former Fig. 9b (Fig. 10b in the revised version) is on the original grid and not aggregated.

87. l. 434 PV below -2 PVU cannot be seen with the colour bar; horizontal PV gradients?

    Reply Thanks, we adjusted the colorbar and included "horizontal" PV gradients (which was missing before).

88. l. 435-436 is the heating maximum shown somewhere?

    Reply Unfortunately, we cannot output heating rates. However, we use the hydrometeor formation as proxy for latent heating in the convective updraft (see also comment 67). A sentence was added previously for clarification: "The maximum amplitude of the PV dipole occurs at about 315-320 K (Fig. 7e) and coincides with the diabatic heating maximum associated with the maximum of the formation of snow and graupel (Fig. 4c)."

89. l. 436 "lens" without e

    Reply Thanks, this is corrected.

90. l. 437-438 please motivate the statement and clarify "mesoscale PV dipole"

    Reply We include this sentence to highlight the agreement with the composite analysis (section 3.4.4 Partitioning of PV anomalies in vorticity and static stability), and now included a short statement for clarification. We also included the spatial dimension of the PV dipole: "Thus, the mesoscale PV dipole pattern with an extent of approximately 100 km across both poles originates predominantly from the spatial variability of vertical vorticity, in agreement with the composite analysis (Fig. 8b and section 3.4)."

91. l. 441 "rapid WCB ascent": convective WCB trajectories?

    Reply See also reply to comment 84. We specified "rapid WCB ascent" in the caption for the according figure: "WCB trajectory ascent >320 hPa in 2 h".

92. l. 445-446 "which are generated and further enhanced by convective ascent" sounds speculative

    Reply We can see that the regions of enhanced convergence are characterized by enhanced low-level PV and coincide with convective ascent. The continuous rapid ascent then additionally enhances the low-level PV. We added "which are generated and *potentially* further enhanced by *continuous* convective ascent".

93. l. 459-450 is the thermal wind vector shown somewhere?

    Reply We realize that the thermal wind vector (which we replaced by "vertical wind shear vector" to be more precise) has not been shown. The vertical wind shear vector is quasi-parallel to the horizontal wind speed in this case study. We added the direction of the vertical wind shear vector in Fig. 7c,d and mention it in the text.

94. l. 458-464 This belongs to the introduction

    Reply We agree that this paragraph deals with theoretical considerations that could be placed in the introduction. However, the discussion of this detailed concept might appear out of context in the more general introduction. Hence, we moved this paragraph to the discussion section (l. 665-674 in the revised manuscript).

95. l. 470 northwest

    Reply We replaced "west" by "northwest", thanks.

96. l. 478 is this supported by section 3 (for this case) or by Shutts 2017 (in general)?

    Reply The presence and spatial scale of the PV dipoles is shown in section 3. We did not explicitly analyse the interaction between these mesoscale PV anomalies with the large-scale flow. Thus, the second part of the sentence is supported by Shutts (2017).

97. l. 479-480 remove "these"

    Reply Done, thanks.

98. l. 480-483 this sounds as three times the same statement, clarify or streamline; "effective resolution" has a specific meaning for numerical modeling, better avoid

    Reply We shortened this paragraph and removed "effective resolution" (l. 456-458 in the revised manuscript).

99. l. 485 is this the case for all larger-scale PV anomalies, or for the example of section 4 only?

    Reply We find several examples of larger-scale PV dipole bands that are aligned with the convective updraft region. However, the exact size varies and depends on the shape and intensity of the convective updrafts. We slightly re-arranged the structure of this section to avoid repetition and clarify that the exact dimensions are only for the given example.

100. l. 486 is the cold front shown somewhere?

    Reply The cold front is not shown because the figures are already rather busy. We attached a figure (Fig. 6 in this document) that shows temperature at 850 hPa at 09 UTC 23 Sep 2016 to show the location of the PV dipole ahead of the cold front. Moreover, the composite analysis (Fig. 3a) shows that the convective ascent occurs ahead of the cold front.

101. l. 490 this seems to describe a specific feature rather than "PV dipole bands"

 Reply We changed "PV dipole bands" to singular to clarify that we analysed one specific PV dipole band.

102. l. 491 southeastward

 Reply Thanks, this sentence was modified (l. 513-514 in the revised manuscript) and now reads "At the time when the PV dipole bands are formed, the associated circulation anomalies do not reach the upper-level waveguide and jet stream in 250 km distance as they are confined to within about 100 km around the PV dipole band (Figs. 9c and 11a)".

103. l. 492 repetition of earlier statements

 Reply Thanks, we removed this sentence.

104. l. 493-497 what is seen where? (which contour, colour, panel)

 Reply The considered PV feature can be seen in Fig. 11 (blue contour with pink shading). We clarified this in the revised manuscript.

105. l. 502-509 more arguments are needed to support that the convectively-produced PV dipole in Fig. 10(a) evolves into the anticyclonic anomaly in Fig. 10(e): the trajectories spread over a much larger area than this specific feature at 18 UTC, and other PV structures exist during the evolution

 Reply The analysis of the PV field with hourly resolution clearly shows how the convectively produced negative PV band evolves in the specific feature at 18 UTC. The evolution of hourly fields actually allows for specifically tracing the evolution of all present larger-scale PV features and enables their distinction. However, we think that it is not necessary to show all timesteps in the manuscript, which would require a lot more panels. Moreover, at 18 UTC, the region of negative PV is still largely covered by trajectories (pink dots), indicating that to a large extent the air mass inside this region originates from the negative PV region at 09 UTC. The trajectories indeed spread over a much wider region at 18 UTC. There are two reasons for this. First, as mentioned in the text, only about 60% of all trajectories actually maintain their negative PV for that long. Secondly, the trajectories spread over several isentropic levels, while the PV contours are only shown at 320 K. At higher isentropic levels, the negative PV extends further equatorward and covers another fraction of the trajectories.

106. l. 514 why use offline trajectories, while online trajectories better follow convective ascent?

 Reply For the analysis of trajectories starting in the upper troposphere, offline (in contrast to online) trajectories were considered because the online trajectories were only started in the lower troposphere to obtain a large number of strongly ascending trajectories. The disadvantage of the online trajectories is that the starting region has to be defined a priori and that due to computational costs (memory allocation) only a limited number of online trajectories can be calculated. To obtain a maximum number of WCB trajectories, the online trajectories were only started in the lower troposphere. Hence, online trajectories arriving in the upper toposphere have all performed a deep ascent from lower levels. However, a large percentage of air parcels that gain negative PV are not directly strongly ascending, but experience PV modification through the "remote effect" of localised heating (note that $\nabla_h \dot{\theta}$ is relevant for PV modification, which extends beyond the most strongly heated region; see also section 5.2) as they pass the left side of the convective updraft regions in the upper troposphere. section 5.2 also shows that the largest fraction of trajectories that gain negative PV are advected quasi-isentropically and pass the left side of the convective ascent region (where the heating maximum is located; see also reply to comment 109). Hence, the number of available online trajectories in the target region in the upper troposphere is too small. Moreover, the online trajectories can only be computed forward, and do not allow for an analysis of their origin. Finally, as the majority of trajectories started within the negative PV region does not ascend directly within the convective updraft, we assume that the offline trajectories approximately represent the actual path of the air parcels. We agree, however, that for strongly ascending trajectories the online trajectories better represent the actual air parcel path than the offline trajectories.

107. l. 517-518 this largely repeats the previous sentence

    Reply We removed this sentence.

108. l. 525-534 the paragraph contradicts the last sentence in l. 523-524 and is confusing altogether; please clarify

    Reply We apologize, but we don't understand what is contradictionary and/or confusing in this paragraph. We tried to be more concise in the previous paragraph to make it easier to understand.

109. l. 538 how exactly do parcels "gain negative PV"?

    Reply What we mean is that air parcels gain "negative PV" as they pass the left side of a convective ascent region (which is strongly heated and represents a local horizontal heating maximum), where the diabatic heating gradient resulting from the localised convective ascent is antiparallel to the horizontal vorticity vector, which leads to PV reduction, and eventually negative PV in regions adjacent to the convective ascent region (cf. PV reduction to the left of the updraft region in Fig. 1). We clarified this in the revised manuscript (e.g., l. 549-555).

110. l. 544 indeed, a comparison with online trajectories is needed to support this result; but again, why use offline trajectories here?

    Reply Unfortunately, not enough online trajectories are available for a comparison (cf. reply to comment 106). Moreover, we assume that offline trajectories with 15 minute resolution are capable to approximately follow the larger-scale flow. As we use an average over more than 40 000 trajectories, we think that statistically the evolution of the number of trajectories with negative PV is a robust result, which also agrees with the long maintenance of the negative PV in the isentropic PV fields. Also because the majority of these trajectories does *not* ascend directly within the convective updrafts, we think that offline trajectories with a temporal evolution of 15 minutes are an appropriate approximation.

111. l. 565 what should be compared between these figures? (which contours)

     Reply We removed this reference, as it is unclear.

112. l. 569-570 this is not sufficiently supported; develop or omit

     Reply As these conclusions (and the previous sentences) are not essential for this study, we omitted the entire last paragraph (former section 5.3).

113. l. 575 not only one case study but one single PV dipole within a cyclone; a first step would be to look at other structures within this cyclone

     Reply To conclude with this statement in the discussion, we indeed analysed several of these PV dipole bands that occur in this WCB case study (see also reply to general comment 1). Unfortunately, we did not explicitly mention this in the submitted manuscript, but we included such a statement in the revised version ["The formation of these PV dipole bands on either side of elongated convective ascent regions can be observed at various times ahead of the upper-level trough in this WCB case study (not shown)."]. Moreover, we attached two more illustrative examples for your consideration (Figs. 3 and 4 in this document).

114. l. 568 avoid "observations" if model-based

     Reply We removed the word "observations".

115. l. 586-594 these various impacts of embedded convection appear speculative; please clearly distinguish between what is due to convectively-generated PV anomalies and to the WCB outflow in general, and be precise about what the cited studies have shown

     Reply We revised the discussion section and more carefully stated what the cited studies analysed.

116. l. 607 heating is also parameterized, even at convection-permitting resolution, through the microphysical scheme

     Reply Thanks, we specified this and added "localized heating from the convection parameterization scheme".

117. l. 611-612 "a horizontal resolution of at least 10 km would be required to resolve the convective updrafts": rather a grid spacing of a few km mostly, as in your simulation

     Reply We changed this sentence and replaced resolution by grid spacing: "a horizontal grid spacing of approximately 2 km would be required".

118. Figure captions: "shading" better than "colours"

     Reply We would like to keep "colours".

119. Providing titles to subfigures would be helpful, as most display rather complex content Fig. 2(a) is too busy: consider showing less trajectories (every second, fifth, tenth, . . .) and one representative, thicker theta contour per lead time. It took me a while to understand what is depicted and I still do not fully see the position of trajectories relative to the cold front.

Reply Thanks, we clarified (former) Fig. 2a (Fig. 3a in the revised manuscript). In addition with the new Fig. 2, the figure is hopefully easier to understand (see also reply to comment 36).

120. Fig. 4 are these really "Vertical cross-section composites"? l. 186-187 rather refers to "composites of vertical profiles along the trajectories, i.e. time-height sections along the flow"; (a,b) 300, 320 and 340-K isentropes; (c,d) "(moist-adiabatic) lapse rate" rather than "potential instability"; d_theta/dz or d_theta_e/dz?

    Reply We indeed show "composites of vertical profiles along the trajectories" and changed this in the according captions. Panels (c,d) show moist stability ($d\theta_e/dz$; this was corrected). We labelled the caption as "moist stability", as we associate one particular gradient with "lapse rate".

121. Fig. 5 "As Fig. 3a,b": not really, better explain again; what do RWP, SWP, RWC, SWC, . . . stand for? Check units; plot (a) box on (b) for comparison?

    Reply We adjusted the caption and simplified the figures.

122. Fig. 8 this figure does not meet the otherwise high quality standard of the paper: tickmarks are too small and need °N/°E to indicate geographical coordinates (in contrast to km in composites); white contours are hardly seen on panels (b-d); vectors and vector legends are too small on (c-d); the colour bar is not adapted to the noisy field in (d); colour bars are completely saturated for negative values in (d-f); finally, (a) is not standard infrared imagery, what does it show exactly?

    Reply Thanks, we have increased the quality of the figure, and more specifically added °N/°E tickmarks, increased the vector legend, and changed the color of the contours. We also adjusted the PV colorbar. Panel (a) shows cloud data from the IR10.8 channel; data are obtained from EUMETSAT and plotted to highlight the large-scale cloud band.

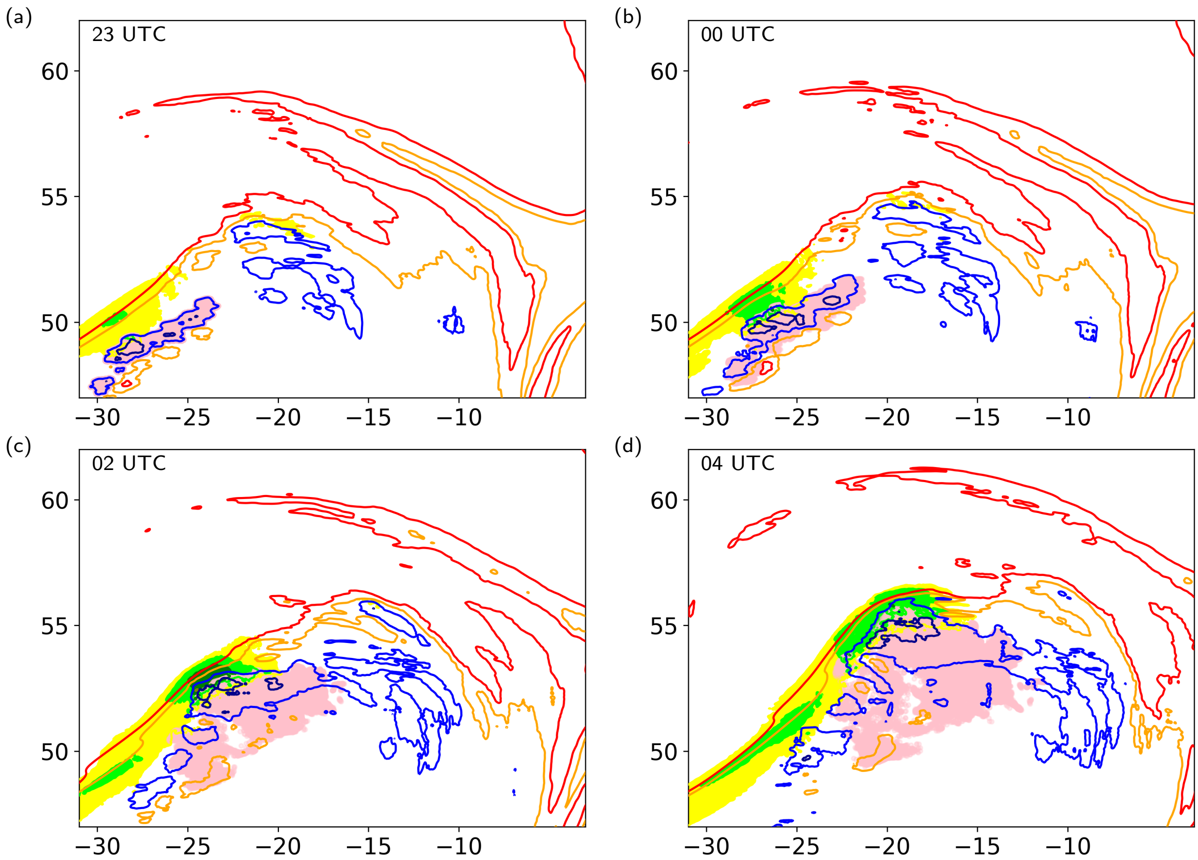

Figure 3: Spatially averaged upper-level PV at 320 K (dark blue, blue, orange and red contours at -1, 0, 1 and 2 PVU) and upper-level jet at 320 K (yellow and green colors at 55, 60 and 65 m s^{-1}) at **(a)** 23 UTC 22 Sep, **(b)** 00 UTC, **(c)** 02 UTC and **(d)** 04 UTC 23 Sep 2016. The pink shading shows the positions of forward trajectories initialized in a region of convectively produced negative PV between 315 and 325 K at 09 UTC.

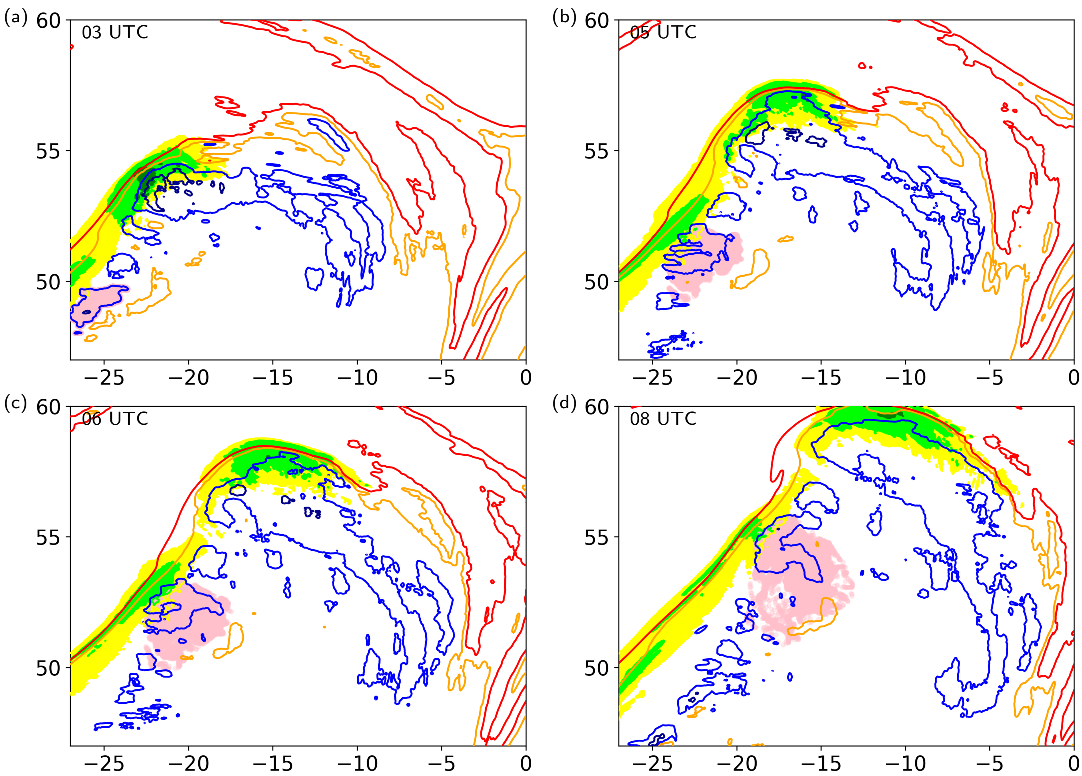

Figure 4: As Fig. 3 but at **(a)** 03 UTC, **(b)** 05 UTC, **(c)** 06 UTC and **(d)** 08 UTC 23 Sep 2016.

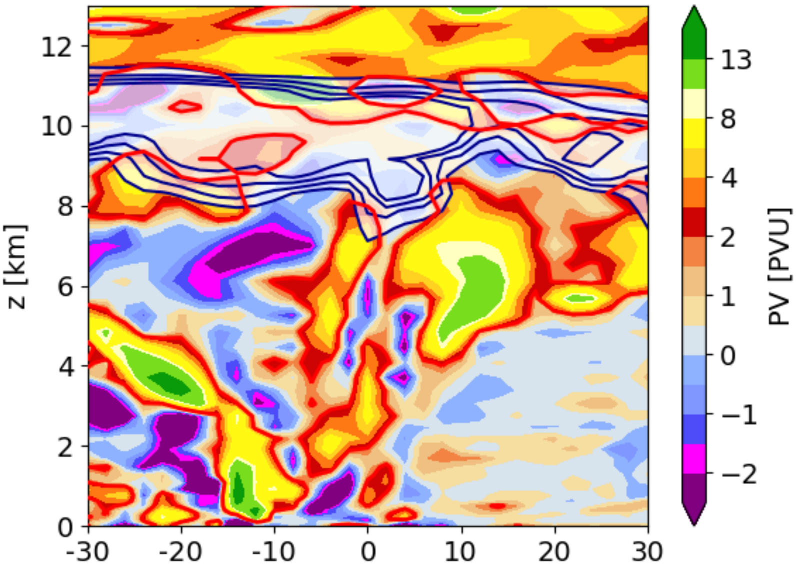

Figure 5: Vertical cross-section across an embedded convective updraft located at '**0**' for PV (colors, in PVU) and ice water content (blue contours, every $0.01\,\mathrm{g\,kg^{-1}}$ from $0.05\,\mathrm{g\,kg^{-1}}$) to illustrate the moisture intrusion across the dynamical tropopause (2 PVU contour, red line) and the moistening of the lower-most stratosphere.

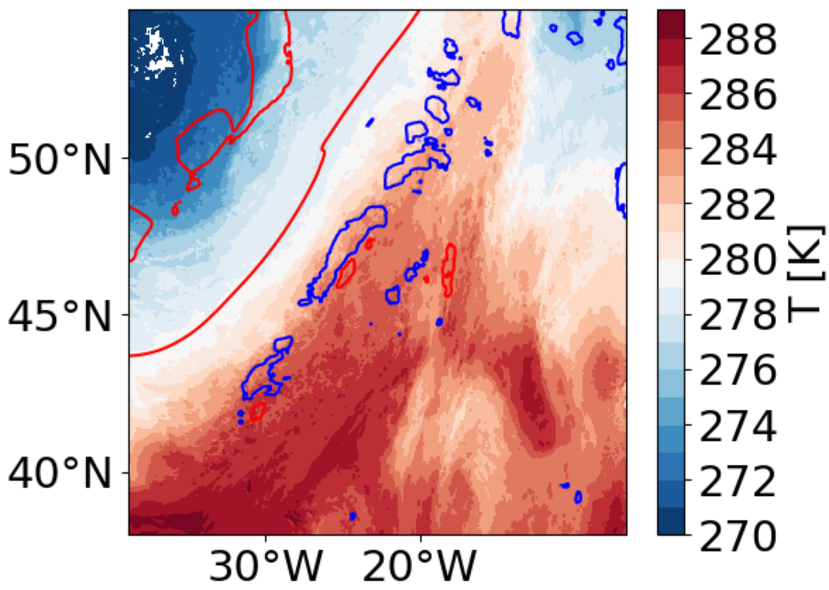

Figure 6: Temperature at 850 hPa (colors, in K) and 0 PVU and 2 PVU contour at 320 K (blue and red contours) at 09 UTC 23 Sep 2016 .

Potential vorticity structure of embedded convection in a warm conveyor belt and its relevance for the large-scale dynamics

Annika Oertel[1], Maxi Boettcher[1], Hanna Joos[1], Michael Sprenger[1], and Heini Wernli[1]

[1]IAC, ETH Zürich, Zürich, Switzerland

Correspondence: Annika Oertel (annika.oertel@env.ethz.ch)

Abstract. Warm conveyor belts (WCBs) are important airstreams in extratropical cyclones. They can influence the large-scale flow evolution ~~due to the modification of the~~ by modifying the potential vorticity (PV) distribution during their cross-isentropic ascent. Although WCBs are typically described as slantwise ascending and stratiform cloud producing airstreams, recent studies identified convective activity embedded within the large-scale WCB cloud band. Yet, the impacts of this WCB-embedded convection have not been investigated in detail. In this study, we systematically analyse the influence of embedded convection in an eastern North Atlantic WCB on the cloud and precipitation structure, on the PV distribution, and on the larger-scale flow. For this, we apply online trajectories in a high-resolution convection-permitting simulation and perform a composite analysis to compare quasi-vertically ascending convective WCB trajectories with typical slantwise ascending WCB trajectories. We find that the convective WCB ascent leads to substantially stronger surface precipitation ~~including~~ and the formation of graupel in the mid- to upper troposphere, which is absent for the slantwise WCB category, indicating the key role of WCB-embedded convection for precipitation extremes. Compared to the slantwise WCB trajectories, the initial equivalent potential temperature of the convective WCB trajectories is higher and ~~they~~ the convective WCB trajectories originate from a region of larger potential instability, which gives rise to more intense cloud diabatic ~~processes~~ heating and stronger cross-isentropic ascent. Moreover, the signature of embedded convection is distinctly imprinted in the PV structure. The diabatically generated low-level positive PV anomalies, associated with a cyclonic circulation anomaly, are substantially stronger for the convective WCB trajectories. ~~While the~~ The slantwise WCB trajectories ~~form~~ lead to the formation of a wide-spread ~~negative PV anomaly~~ region of low-PV air (but still with weakly positive PV values) in the upper troposphere, in agreement with previous studies. In contrast, the convective WCB trajectories ~~, in contrast,~~ form mesoscale horizontal PV dipoles at upper levels, with one pole reaching negative PV values. On the larger-scale, these individual mesoscale PV anomalies can aggregate to elongated PV dipole bands extending from the convective updraft region, which are associated with coherent larger-scale circulation anomalies. An illustrative example of such a convectively generated PV dipole band shows that within around 10 hours the negative PV pole is advected closer to the upper-level waveguide, where it strengthens the isentropic PV gradient and contributes to the formation of a jet streak. This suggests that the mesoscale PV anomalies produced by embedded convection upstream organise and persist for several hours, and therefore can influence the synoptic-scale circulation. They thus can be dynamically relevant, influence the jet stream and potentially the downstream flow evolution, which are highly relevant aspects for medium-range weather forecast. Finally, our results imply that a distinction between slantwise and convective WCB trajectories is meaningful

because the convective WCB trajectories are characterized by distinct properties, such as the formation of graupel and of an upper-level PV dipole, which are ~~absent for~~ not present for the slantwise WCB trajectories.

1 Introduction

1.1 Warm conveyor belts and embedded convection

Moist diabatic processes ~~in extratropical cyclones~~ are known to play an important role for ~~their evolution~~ the evolution of extratropical cyclones and are frequently associated with rapid cyclogenesis ~~(e.g., Anthes et al., 1983; Kuo et al., 1991; Stoelinga, 1996; Wernli and Davies, 1997)~~ (e.g., Anthes et al., 1983; Kuo et al., 1991; Stoelinga, 1996; Wernli et al., 2002) and increased forecast error growth (e.g., Davies and Didone, 2013; Selz and Craig, 2015). Diabatic processes are particularly important in warm conveyor belts (WCBs), which are coherent, typically poleward ascending airstreams associated with extratropical cyclones (Harrold, 1973; Browning, 1986, 1999; Wernli and Davies, 1997). During their typically slantwise cross-isentropic ascent from the boundary layer ahead of the cold front to the upper troposphere, they form large-scale mostly stratiform cloud bands and play a key role for the distribution of surface precipitation (e.g., Browning, 1986; Eckhardt et al., 2004; Madonna et al., 2014; Pfahl et al., 2014; Flaounas et al., 2018).

~~Furthermore, the~~ Although WCBs are typically described as gradually ascending and mainly stratiform cloud producing airstreams (e.g., Browning, 1986; Madonna et al., 2014), already in 1993 the concept of rapid convective motion embedded in the frontal cloud band of the WCB was proposed (Neiman et al., 1993). Recent studies suggested that the WCB is, at least in some cases, not a homogeneously ascending airstream: in contrast, the detailed ascent behavior of the individual WCB trajectories associated with one extratropical cyclone can vary substantially (e.g., Martínez-Alvarado et al., 2014; Rasp et al., 2016; Oertel et al., 2019) and convective activity can be frequently embedded in the large-scale baroclinic region of the WCB. This has been identified, e.g., with various remote-sensing data (Binder, 2016; Crespo and Posselt, 2016; Flaounas et al., 2016, 2018), with online trajectories in convection-permitting simulations (Rasp et al., 2016; Oertel et al., 2019) and in coarser simulations with parameterized convection (Agustì-Panareda et al., 2005; Martínez-Alvarado and Plant, 2014).

The strong cloud diabatic processes ~~during WCB ascent~~ in both WCBs and convection modify the potential vorticity (PV) distribution in the lower and upper troposphere and thereby ~~potentially affect the~~ can affect the larger-scale dynamics (e.g., Pomroy and Thorpe, 2000; Grams et al., 2011; Clarke et al., 2019). Hence, WCBs and convection can be associated with increased forecast uncertainty (Baumgart et al., 2019; Berman and Torn, 2019) and forecast errors (e.g., Martínez-Alvarado et al., 2016a; Clarke et al., 2019). Occassionally, convection and WCBs individually can be related to forecast busts (Rodwell et al., 2013; Grams et al., 2018). The specific PV signatures of (i) large-scale ~~flow evolution (e.g., Wernli and Davies, 1997; Wernli, 1997; Madonna et al., 2014; Joos and Forbes, 2016)~~ WCB ascent and (ii) smaller-scale convective updrafts, and their potential implications for the flow evolution differ substantially and are discussed in the following.

1.2 PV modification by WCBs and convection

PV is materially conserved along the flow only in the absence of friction and diabatic processes (Hoskins et al., 1985). Neglecting frictional processes, the Lagrangian rate of change $\frac{D}{Dt}PV$ can be expressed as

$$\frac{D}{Dt}PV = \frac{1}{\rho}\boldsymbol{\omega}\cdot\nabla\dot{\theta}, \tag{1}$$

where PV is defined as (Ertel, 1942)

$$PV = \frac{1}{\rho}\boldsymbol{\omega}\cdot\nabla\theta \tag{2}$$

and ρ is density, θ is potential temperature, $\dot{\theta}$ represents diabatic heating or cooling, and $\boldsymbol{\omega}$ is 3D absolute vorticity ($\boldsymbol{\omega} = \nabla\times\mathbf{u} + 2\boldsymbol{\Omega} = \xi\mathbf{i} + \eta\mathbf{j} + (f+\zeta)\mathbf{k}$, where $\mathbf{u}$ is the 3D wind vector, $\boldsymbol{\Omega}$ is the vector of earth rotation, ξ and η are the horizontal vorticity components in the x- and y-directions, f is the Coriolis parameter, and $f+\zeta$ is the absolute vertical vorticity).

For large-scale and predominantly slantwise WCB ascent it is frequently assumed that the first-order effect of latent heating on PV is dominated by the vertical gradient of diabatic heating (e.g., Wernli and Davies, 1997; Joos and Wernli, 2012; Madonna et al., 2014) resulting in PV generation below and PV destruction above the diabatic heating maximum according to Eq. 3:

$$\frac{D}{Dt}PV \approx \frac{1}{\rho}(f+\zeta)\cdot\frac{\partial\dot{\theta}}{\partial z}. \tag{3}$$

These diabatically produced low-level positive and upper-level negative PV anomalies can lead to cyclone intensification (Rossa et al., 2000; Binder et al., 2016) and modify the upper-level flow evolution ~~(Pomroy and Thorpe, 2000; Grams et al., 2011; Schäfler and Harnisch, 2015; Joos and Forbes, 2016; Martínez-Alvarado et al., 2016b)~~ (e.g., Pomroy and Thorpe, 2000; Grams et al., 2011; Schäfler and Harnisch, 2015; Joos and Forbes, 2016; Martínez-Alvarado et al., 2016b

PV is frequently considered for synoptic-scale dynamics (e.g., Hoskins et al., 1985; Stoelinga, 1996), but is also suited for the analysis of mesoscale convective systems ~~(e.g., Pomroy and Thorpe, 2000; Martínez-Alvarado et al., 2016b; Shutts, 2017; Clarke et al., 2019)~~ (e.g., Conzemius and Montgomery, 2009; Shutts, 2017; Clarke et al., 2019) and has already been applied at the scale of ~~convective storms~~ individual convective cells (Chagnon and Gray, 2009; Weijenborg et al., 2015, 2017). While for PV modification in synoptic-scale systems the horizontal ~~gradients~~ gradient of diabatic heating ~~are~~ is frequently neglected (as in Eq. 3), this assumption breaks down in the case of intense local diabatic heating such as embedded mesoscale convective updrafts on the scale of a few kilometers. ~~There the~~ On the mesoscale, the horizontal gradients of $\dot{\theta}$ become relevant and Eq. 3 generalizes to the full form ~~,~~ (Eq. 2), written here as

$$\frac{D}{Dt}PV = \frac{1}{\rho}\left[(f+\zeta)\frac{\partial\dot{\theta}}{\partial z} + \boldsymbol{\omega}_h\cdot\nabla_h\dot{\theta}\right]\cancel{.} \tag{4}$$

~~In contrast to the WCB, where~~ where $\boldsymbol{\omega_h}$ denotes the horizontal vorticity ($\boldsymbol{\omega_h} = \xi\mathbf{i} + \eta\mathbf{j}$). Previous studies showed that the ~~vertical gradient dominates, the~~ horizontal diabatic heating ~~gradient plays~~ gradients play a major role for the PV modification in isolated ~~(mesoscale)~~ convective updrafts (e.g., Chagnon and Gray, 2009; Weijenborg et al., 2015, 2017) and in narrow smaller-scale heating regions embedded in a larger-scale flow (Harvey et al., 2020). The localized diabatic heating in ~~convective updrafts in~~ a vertically sheared environment generates upper-level horizontal PV dipoles centered around the convective updraft (Fig. 1) and aligned with the horizontal vorticity vector ~~ω_h~~ $\boldsymbol{\omega_h}$ (Eq. 4~~).~~, Fig. 1, green arrow), which is rotated 90° anticlockwise to the vertical wind shear vector $\boldsymbol{v_z}$ (Fig. 1, black arrow). Thereby, the positive PV pole (red shading in Fig. 1) occurs to the right of the ~~direction of the thermal wind vector $\mathbf{v_T}$ (~~vertical wind shear vector $\boldsymbol{v_z}$ [since there, $\nabla_h\dot{\theta}$ (Fig. 1, grey arrows) is parallel to ~~ω_h)~~ $\boldsymbol{\omega_h}$] and the negative pole (blue shading in Fig. 1) occurs to the left of ~~$\mathbf{v_T}$ (~~$\boldsymbol{v_z}$ [where $\nabla_h\dot{\theta}$ and ~~ω_h are antiparallel), as illustrated in~~ $\boldsymbol{\omega_h}$ are antiparallel]. The strongest PV production and destruction (Fig. 1, dark red and dark blue shading, respectively) arise where the horizontal vorticity vector (Fig. 1, green arrow) and the horizontal diabatic heating gradient, which points radially towards the center of the convective updraft (Fig. 1~~. This tilting of the PV dipole from the vertical, as typically observed for large-scale WCB ascent, into the horizontal~~, grey arrows), are quasi-aligned, i.e., where the angle α between both vectors is small, as $\frac{D}{Dt}PV \approx |\boldsymbol{\omega_h}| \cdot |\nabla_h\dot{\theta}| \cdot \cos\alpha$. The PV production and destruction is attenuated where the angle α between $\boldsymbol{\omega_h}$ and $\nabla_h\dot{\theta}$ increases (Fig. 1, orange and light blue shading, respectively). Thus, for smaller-scale diabatic heating, as in convective updrafts, the horizontal components of PV become increasingly dominant and generate an upper-level horizontal PV dipole, whereby one pole can reach negative PV values (Harvey et al., 2020).

This quasi-horizontal PV dipole structure is a robust response of convective updrafts in the presence of vertical wind shear (Chagnon and Gray, 2009; Weijenborg et al., 2015, 2017; Hitchman and Rowe, 2017). Such convectively generated PV dipoles were previously identified in idealized simulations of isolated cumulus-scale convection (Chagnon and Gray, 2009), in case studies of mesoscale convective systems (Davis and Weisman, 1994; Chagnon and Gray, 2009; Hitchman and Rowe, 2017; Clarke et al., 2019), and in mid-latitude convective updrafts with varying large-scale flow conditions (Weijenborg et al., 2015, 2017). The ~~amplitudes~~ amplitude of the horizontal PV dipoles can strongly exceed the typical amplitude of synoptic-scale PV. In strong convective updrafts horizontal PV dipoles of ~~±10PVU~~ ±10 PVU can be generated (Chagnon and Gray, 2009; Weijenborg et al., 2015, 2017), resulting in regions of absolute negative PV~~, which are dynamically unstable~~. These regions can be hydrostatically, inertially or symmetrically unstable ~~(Schultz and Schumacher, 1999)~~ (e.g., Hoskins, 2015) and can form mesoscale circulations associated, e.g., with frontal rainbands (Bennetts and Hoskins, 1979; Schultz and Schumacher, 1999; Siedersleben and Gohm, 2016), sting jets ~~(Clark et al., 2005; Volonté et al., 2018)~~(Clark et al., 2005; Volonté et al., 2018, 2019), enhanced stratosphere-troposphere exchange (Rowe and Hitchman, 2015), and local jet accelerations and northward displacements (Rowe and Hitchman, 2016). The adjustment timescales for the release of these instabilities ~~ranges~~ range from minutes for hydrostatic instability to several hours for inertial instability [~~scales with~~ timescale is proportional to $[-f(f+\zeta)]^{-1/2}$ ~~; Schultz and Schumacher (1999); Thompson et al. (2018)~~(Schultz and Schumacher, 1999; Thompson et al., 2018)]. Thus, while hydrostatic instability is rapidly released and near-neutral conditions are established, inertial instability can prevail for several hours and therefore synoptic-scale regions of inertial instability can be ~~observed~~found, for instance at the anticyclonic shear side of midlatitude ridges (Thompson et al., 2018).

~~Although WCBs are typically described as gradually ascending and mainly stratiform cloud producing airstreams (e.g., Browning, 1986; Madonna et al., 2014), already in 1993 the concept of rapid convective motion embedded in the frontal cloud band of the WCB was proposed (Neiman et al., 1993). Recently, studies suggested that the WCB is, at least in some cases, not a homogeneously ascending airstream: in contrast, the detailed ascent behaviour of the individual WCB trajectories associated with one extratropical cyclone can vary substantially (e.g., Martínez-Alvarado et al., 2014; Rasp et al., 2016; Oertel et al., 2019) and convective activity can be frequently embedded in the large-scale baroclinic region of the WCB. This has been identified, e.g., with remote-sensing data (Binder, 2016; Crespo and Posselt, 2016; Flaounas et al., 2016, 2018), with online trajectories in convection-resolving simulations (Rasp et al., 2016; Oertel et al., 2019) and in coarser simulations with parameterized convection (Agustì-Panareda et al., 2005; Martínez-Alvarado and Plant, 2014). WCBs and convective systems can both lead to forecast errors due to their associated strong diabatic processes (e.g., Martínez-Alvarado et al., 2016b; Clarke et al., 2019). Ocassionally, this might even lead to forecast busts (Rodwell et al., 2013), especially in coarser-scale simulations where the PV anomaly amplitude is underestimated due to the parameterization of convection (Done et al., 2006; Chagnon and Gray, 2009; Clarke et al., 2019).~~

~~Although previous studies~~ Previous studies analysed the PV modification by individual convective updrafts and mesoscale convective systems. However, the PV modification by aggregated convection embedded in the WCB ascent region, which is already subject to strong diabatic PV modification from large-scale WCB ascent, has not yet been investigated. Hence, the contribution of embedded convection in WCBs to the distribution of PV and the formation of mesoscale PV anomalies, which may influence the development of extratropical cyclones, is still unknown. Moreover, the persistence and dynamical relevance of the convectively generated PV dipoles has not yet been analysed. Weijenborg et al. (2017) hypothesized that the convectively formed large-amplitude PV anomalies could be longer-lived than the relatively short-lived convective updrafts and suggested that a more detailed investigation of these PV anomalies might shed light on the dynamical relevance of convection. Related to this is the question whether the convectively generated PV dipoles aggregate to larger-scale PV anomalies and, if yes, whether they feed back on the synoptic-scale flow (Chagnon and Gray, 2009).

1.3 Aim and outline

In this study, we investigate convection embedded in ~~WCBs~~ a WCB case study and systematically analyse the PV modification of this convective activity. Furthermore, we go beyond the identification of convectively produced PV anomalies and evaluate the effect of these mesoscale PV anomalies on the larger-scale flow, thereby emphasizing the dynamical relevance of embedded convection. Therefore, ~~we compute~~ online trajectories in a high-resolution convection-permitting simulation are computed to compare convective and slantwise WCB trajectories and their impact on the cloud and precipitation structure, as well as on the mesoscale and larger-scale dynamics. Together, this study shows how WCB-embedded convection on the one hand influences the local mesoscale dynamics and on the other hand can modify the larger-scale flow evolution – both relevant aspects for predictability. Moreover, this study provides a refined perspective on the relevance of smaller-scale processes for the larger-scale WCB dynamics. Specifically, we ~~adress~~ address the following questions:

1. ~~Where do convective and slantwise WCB trajectories originate from and how does their ascent differ (section 3.4)?~~
2. What is the impact of convective WCB ascent on the cloud and precipitation structure (section 3.2)?
3. What are characteristic thermodynamic properties of convective and slantwise WCB ascent (section 3.3)?
4. Where do convective and slantwise WCB trajectories originate from (section 3.4)?
5. How does convective (vs. slantwise) WCB ascent modify the PV distribution along the ascent and in its environment (section 3.5)?
6. What is the ~~influence~~ impact of convectively modified PV on the local wind speed and circulation in the upper troposphere (section 3.6)?
7. How does convection embedded in WCBs and its associated PV anomalies influence the larger-scale dynamics (section ~~4.1~~4)?

This study is structured in the following way: ~~In section 2 , we explain~~ Section 2 explains the methodology and shortly ~~introduce the~~ introduces the analysed WCB case study. Thereafter, we systematically consider the mesoscale effects of convection embedded in WCBs (questions ~~1-4~~1-5) in a composite analysis (section 3)~~, before discussing an illustrative example of the characteristics and impact of convective ascent embedded in the WCB (section 4.1). To adress~~. To address the question of the dynamical relevance of WCB-embedded convection (question ~~5~~6), we consider ~~the~~ an illustrative example of the characteristics and impact of WCB-embedded convection (section 4.1) and evaluate the influence of the convectively generated PV anomalies on ~~a larger scale and evaluate their influence on~~ the large-scale flow (section 4.1). Finally, we provide a discussion and outlook (section 5) and conclusions (section 6).

2 Data and approach

2.1 COSMO setup and trajectories

The ~~setup of the COSMO simulation and the online trajectories used to address the questions outlined in section 1 is the same as in Oertel et al. (2019). The~~ WCB case study ~~was~~ is simulated with the limited-area nonhydrostatic model COSMO ~~(Baldauf et al., 2011; Doms and Baldauf, 2018)~~ (Consortium for Small-scale Modeling; Baldauf et al., 2011; Doms and Baldauf, 2018) at 0.02° (≈2.2 km) horizontal ~~resolution~~ grid spacing with 60 vertical levels. The ~~simulation was initialised~~ setup of the COSMO simulation and the online trajectories is the same as in Oertel et al. (2019). The simulation is initialized at 00 UTC 22 Sep 2016 in the early phase of the cyclogenesis of ~~"Vladiana"~~ cyclone *Vladiana* (see section 2.2) and ~~run~~ runs for 112 hours (see Oertel et al., 2019). Initial and lateral boundary conditions are taken from the ECMWF analyses with a horizontal resolution of 0.1° every 6 hours. The domain is centered in the eastern North Atlantic and extends from about 50°W to 20°E and 30°N to 70°N. We ~~applied~~ apply the standard COSMO setup of the Swiss National Weather Service, which employs a one-moment six-category cloud microphysics scheme including prognostic water vapour (q_v), liquid (LWC) and ice ~~cloud water content~~ (IWC) cloud water content, rain (LWC), snow (SWC) and graupel (GWC). The graupel category is important for the explicit simulation of deep convection (Baldauf et al., 2011). Deep convection is resolved at 2.2 km (e.g., Ban et al., 2014) while for shallow convection the reduced Tiedtke scheme was applied (Tiedtke, 1989; Baldauf et al., 2011). 3D COSMO fields ~~were~~ are output every 15 minutes, which allows capturing the large temporal and spatial variability of embedded convection.

To identify phases of embedded convective ascent in the WCB, 10 000 online trajectories ~~were~~ are started from a pre-defined ~~starting~~ region at 7 vertical levels (250, 500, 750, 1000, 1500, 2000 and 2500 m a.s.l.) every 2 h during the simulation~~(Miltenberger et al., 2013, 2014)~~. The online trajectory positions are calculated from the resolved 3D wind field at every model time step, i.e. every 20 s, and thus, explicitly capture rapid convective ascent ~~(Miltenberger et al., 2013; Rasp et al., 2016; Oertel et al., 2019)~~(Miltenberger et al., 2013, 2014; Rasp et al., 2016; Oertel et al., 2019). WCB trajectories ~~were calculated~~ are subsequently selected as trajectories with an ascent rate of at least 600 hPa in 48 h (Madonna et al., 2014).

2.2 Overview of WCB case study

The investigated WCB ~~was~~ is associated with the North Atlantic extratropical cyclone ~~"Vladiana" (IOP 3 of NAWDEX, Schäfler et al., 2018) from~~ *Vladiana* that occurred between 22-25~~Sep 2016.~~ Sep 2016 [IOP 3 of the North Atlantic Waveguide and Downstream Impact EXperiment (NAWDEX, Schäfler et al., 2018)]. The cyclone with a ~~maximum intensity~~ minimum sea level pressure of 975 hPa is located below an upper-level trough and ~~travels~~ propagates eastward and northward across the North Atlantic toward Iceland, where it becomes stationary ~~.~~(Fig. 2). The cyclone's WCB ascends in the warm sector predominantly in a narrow band ahead of the cold front and develops a weak cyclonic and a stronger anticyclonic branch (cf. Wernli, 1997; Martínez-Alvarado et al., 2014), which turns into the downstream upper-level ridge and contributes to its amplification ~~. For a~~ (see Fig. 2d-f in Oertel et al., 2019). A more detailed analysis of the cyclone evolution and its WCB ascent ~~see~~ is presented in Oertel et al. (2019).

The WCB trajectories in the baroclinic zone ahead of the cyclone's cold front vary considerably in their ascent rates (Fig. 2a-c; see also the animation in the online supplemental material) and also include phases of embedded convection. These phases are characterized by a rapid ascent of more than 400-600 hPa in 2 h, and they are embedded in a larger region of slower, more gradual WCB ascent ~~(Oertel et al., 2019)~~(red circles in Fig. 2a-c and online supplemental material; cf. Oertel et al., 2019). The region of embedded convective activity is characterized by a very heterogeneous PV field of ~~diabatically-produced~~ diabatically produced small-scale but high-amplitude PV anomalies of ~~±10 PVU~~ ±10 PVU in the upper troposphere ~~(cf. Fig. 9d; Oertel et al., 2019, Appendix)~~(Fig. 2d-f and online supplemental material), suggesting that embedded convection in WCBs can strongly modify the PV distribution. There is, however, no clear separation between convective and slantwise ascent in the WCB of cyclone ~~"Vladiana"~~ *Vladiana* (Oertel et al., 2019). Instead, it is rather a continuum of ascent rates ranging from very rapid convective ascent of more than 600 hPa in 2 h to a slower gradual ascent of approximately 50 hPa in 2 h. Nevertheless, we can meaningfully classify the WCB trajectories into two ~~categories~~ sub-categories based on their ascent rate to compare convective versus slantwise WCB ascent (see section 2.3).

2.3 WCB trajectory ~~categorisation~~ categorization and WCB ascent region

To compare the rapid convective WCB ascent to the "typical" ~~more slowly~~ slower and slantwise WCB ascent, we ~~selected two categories~~ define two sub-categories of coherently ascending WCB trajectories~~from all WCB trajectories associated with the cyclone~~: (i) convectively ascending WCB trajectories that perform a rapid quasi-vertical ascent through the whole tropospheric column, and (ii) slantwise WCB trajectories that ascend more slowly and gradually from the boundary layer into the upper troposphere. The selection criteria are based on the fastest 400-hPa and 600-hPa ascent phases along the WCB trajectories: a WCB trajectory is considered as convective if its fastest 400-hPa and 600-hPa ascent times are shorter than 1 h and 3 h, respectively. These ascent rates correspond to the 10% fastest ascent rates of all trajectories of the considered WCB. Likewise, a WCB trajectory is assigned to the slantwise WCB category if the 400-hPa and 600-hPa ascent times are between 1.5 h to 3.5 h and 6.5 h to 22 h, respectively. These ascent times correspond to the average ascent rates of all WCB trajectories (~~25^{th} to 75^{th}~~ 25^{th} to 75^{th} percentiles). ~~These~~ The selection criteria result in approximately 2000 convective WCB trajectories, and approximately 7000 more slowly ascending slantwise WCB trajectories.

Figure 3a shows the temporal evolution of the WCB trajectory positions at the start of their ascent relative to the approaching cold front ~~for selected time steps and illustrates the~~ at selected times. The main WCB ascent ~~region~~ occurs ahead of the cold front and the upper-level trough ~~. The~~ (see also online supplemental material). The selected convective WCB trajectories perform a rapid and deep ascent through the whole ~~tropospheric column~~ troposphere mostly south of 50°N (Fig. 3a, black outlined circles), and the slantwise WCB trajectories with comparatively slow and gradual ~~WCB ascent~~ ascent rates are located ahead of, and travel northward with, the cold front during their ascent (Fig. 3a, grey outlined triangles). During the 3 days of major WCB ascent from 22 Sep to 24 Sep 2016, ~~the region of ascent shifts~~ a joint evolution and eastward propagation of about 20° ~~eastward with the evolving cycloneand~~ of the cyclone, its cold front ~~(see coloured~~ and the WCB ascent region takes place (see colored symbols in Fig. 3a). Despite the differing ascent ~~behaviour~~ behavior of the WCB categories, the convective WCB ascent is directly embedded in the region of large-scale ascent, i.e., in close proximity to the more slowly ascending WCB trajectories. The convective WCB trajectories start their ascent on average slightly further south at the cold front ($45.2° \pm 3°$) compared to the slantwise WCB trajectories whose ascent region extends further poleward ($47.7° \pm 4°$). Nevertheless, the overall region of origin and ascent overlaps (Figs. 2a-c and 3a) and the convective WCB ascent is indeed embedded in the region of slower WCB ascent. This indicates that although their ascent rates differ, both WCB categories are not spatially separated (Fig. 3a).

3 Characteristics of convective and slantwise WCB ascent

3.1 Composite ~~computation~~analysis

The similarities and differences of the characteristics of convective and slantwise WCB trajectories are systematically compared in a composite analysis. For computing composites for both WCB categories, the selected WCB trajectories ~~were~~ are centered relative to the time of the start of the fastest 400-hPa ascent phase. Composites ~~were~~ are computed based on the trajectory position every ~~15-minutes~~15 minutes, which corresponds to the temporal resolution of the COSMO output.

Three types of composites ~~were~~ are produced for both WCB categories: (i) composites of vertical profiles along the trajectories, i.e. time-height sections along the flow, and (ii) horizontal and (iii) vertical cross-sections centered at the trajectories' geographical position. While the along-flow composites provide a Lagrangian perspective on the local dynamical impact of the WCB trajectories, the horizontal and vertical cross-sections allow analysing ~~their effect on the~~ the mutual interaction between the WCB and its surroundings. Because the trajectories are located in a region with coherent background flow ahead of the upper-level trough (cf. Fig. 2a-c), the fields ~~were~~ are not rotated for the composite computation. This enables a direct interpretation of the atmospheric conditions and perturbations in geographic coordinates.

The number of selected convective and slantwise WCB trajectories is not homogeneous in time; instead pulses of convective and slantwise WCB ascent occur ~~(Fig. 3b and cf. Oertel et al., 2019)~~(Fig. 3a,b and cf. Oertel et al., 2019). In particular, two pulses of increased convective activity occur at around 00 UTC 23 Sep and 00 UTC 24 Sep. Hence, the composite analyses are dominated by these times when large numbers of WCB trajectories are selected for each category.

~~In the following, we first compare the ascent behavior and environment of convective and slantwise WCB trajectories (section 3.4) and subsequently describe the precipitation and cloud structure associated with both WCB categories (section 3.2). Next, the PV structure associated with convective and slantwise WCB ascent is shown (section 3.5) and related to the larger-scale flow anomalies (section 3.6).~~

3.2 ~~Environment for convective and slantwise WCB ascent~~

~~The rapidly ascending~~ The convective WCB trajectories ~~originate from a warmer and moister region ($\overline{T} = 287\,\mathrm{K}, \overline{q_v} = 11.5\,\mathrm{g\,kg^{-1}}$) compared to the more slowly ascending slantwise WCB trajectories ($\overline{T} = 285\mathrm{K}, \overline{q_v} = 10\,\mathrm{g\,kg^{-1}}$), and are thus characterized by substantially higher initial θ_e (Figs. 6a and 5a) than the slantwise WCB trajectories (Figs. 6b and 5b). At the start of the ascent, $\overline{\theta_\mathrm{e}}$ amounts to 330 K for the convective WCB trajectories and to 324 K for the slantwise WCB trajectories (Fig. 5a,b). Although the convective ascent is embedded within the region of slantwise ascent ahead of the cold front (Fig. 3), where θ_e-contours nearly become vertical (Fig. 6c,d), the convective WCB trajectories ascend from a mesoscale, meridionally elongated region characterized by warmer and more humid conditions ahead of a strong localised θ_e-gradient (Fig. 6a). This narrow tongue of very high θ_e air with q_v exceeding $11\,\mathrm{g\,kg^{-1}}$ extends laterally from ahead of the cold front only approximately 50 km into the warm sector and forms a strong horizontal θ_e gradient (Fig. 6a). Moreover, the WCB ascent region ahead of the cold frontal zone coincides with low-level convergence of the horizontal wind (Fig. 6c,d), which is particularly strong for the convective WCB trajectories. The mesoscale frontal θ_e structures ahead of the cold front arise from large θ_e variability in the warm sector. The higher θ_e of the convective WCB trajectories subsequently leads to more intense cloud diabatic processes and a faster and stronger cross-isentropic ascent (Fig. 5a,b).~~

~~The convective WCB trajectories ascend rapidly from the~~ ascend quasi-vertically from the boundary layer to the upper troposphere to on average 10 km height ($\pm$ 1.0 km) in about 1-2 h (Fig. ~~5a) from a region of strong potential instability characterized by vertical θ_e gradients of $-4\,\mathrm{K\,km^{-1}}$ prior to the start of the convective ascent (Fig. 5c), and continue to~~

~~moderately ascend almost isentropically along the upper-level ridge after arriving in the upper troposphere (Fig. 5a). The convective WCB ascent is likely triggered through lifting of the potentially unstable layer in the frontal ageostrophic circulation (cf. quasi-geostrophic omega ahead of cold front, Oertel et al., 2019). During an initial adiabatic ascent the low-level potentially unstable layer in the WCB inflow region remains potentially unstable until saturation is reached at the lifting condensation level. There, the potential instability can be released leading to the observed rapid convective updrafts (Schultz and Schumacher, 1999; Sherwood, 2000; Schultz et al., 2000).~~

4a, black line). In contrast, the ~~slower~~ slantwise WCB trajectories ~~start their ascent from the boundary layer in a region characterized by weaker potential instability and lower relative humidity (Fig. 5d) and ascend on top of the (cold) frontal region characterized by comparatively large potential stability (Fig. 5b,d). After an initially swift ascent (due to the centering relative to the fastest 400-hPa ascent) , the ascent rate decreases and the trajectories~~ are characterized by a substantially slower ascent (in agreement with our selection criteria) and perform a gradual slantwise ascent until they reach their final outflow level at~~on average~~ , on average, 9 km ($\pm$ 1.2 km) height after approximately 18 h~~. Hence,~~ , after an initially swift ascent (due to the centering relative to the fastest 400-hPa ascent) in the lower troposphere (Fig. 4b, black line). Thus, the final WCB outflow height of the slantwise WCB trajectories is on average lower ~~compared to~~ than for the convective WCB trajectories~~that reach on average approximately 10 km height~~.

In the following, we first describe the precipitation and cloud structure associated with the rapid convective and slower slantwise WCB trajectories (section 3.2). Subsequently, we analyse their thermodynamic properties (section 3.3) and compare the environment of both WCB categories (section 3.4). Then, the PV structure associated with convective and slantwise WCB ascent is investigated (section 3.5) and related to the flow anomalies (section 3.6).

3.2 Precipitation and cloud structure

~~During their rapid ascent the convective WCB trajectories locally produce intense surface precipitation (Fig. 4a, c, blue lines) . The precipitation maximum coincides with the strongest ascent phase in the mid-troposphere, where also a local maximum of graupel production occurs (Fig. 4c, magenta contours).~~ The convective cloud formed during the rapid WCB ascent is characterized by ~~a large hydrometeor content~~ large hydrometeor contents of up to 1 g ~~kg^{-1}~~ kg^{-1} (Fig. 4~~c~~a) and the vertically integrated rain, snow and graupel water path in close proximity to the updraft can reach up to 6 kg ~~m^{-2}~~ m^{-2} (Fig. 4~~a~~e), forming a locally dense and vertically extended cloud (Fig. 4~~c~~a). Directly above the convective updraft the cloud top height reaches a local maximum (Fig. 4a). During their rapid ascent the convective WCB trajectories locally produce intense surface precipitation (Fig. 4c,e). The ~~maximum~~ precipitation maximum coincides with the strongest ascent phase in the mid-troposphere (Fig. 4a,c), where also a local maximum of graupel production occurs (Fig. 4a, magenta contours). The maximum surface precipitation is slightly shifted upstream relative to the convective updraft (Fig. 4~~a).~~ e). The upper-level WCB outflow remains inside a ~~comparatively~~ thick cirrus cloud for several hours, which has formed during the convective ascent and is subsequently advected with the upper-level mean flow (Fig. 4~~c, purple~~ a, turquoise contours). This convectively formed cirrus cloud can be considered as a longer-lived convective anvil cloud, suggesting that embedded convection is also relevant for the larger-scale upper-level cloud cover. ~~Cloud top height reaches a local maximum directly above the convective updraft and an injection~~

~~of IWC into the lower (dynamical) stratosphere can be observed, indicating the potential for overshooting convection and moistening of the lower stratosphere with WCBs (Fig. 4c).~~

The cloud formed during the slantwise WCB ascent is comparatively less dense, with ~~reduced~~ lower rain, ice, and snow water content and without graupel production (Fig. 4b,~~d~~f). Accordingly, the cloud structure and cloud top are ~~horizontally~~ more homogeneous and stratiform, and the surface precipitation maximum along the ascent (Fig. 4d) is substantially weaker compared to the convective WCB ascent (peak value reduced by a factor of 3). The vertically integrated rain, snow and graupel water paths for the slantwise WCB trajectories are substantially lower and distributed homogeneously over a larger area (Fig. 4~~b). Interestingly, also for the slantwise WCB trajectories, an intrusion of IWC into the stratosphere occurs in the simulation (Fig. 4d).~~ f). The WCB outflow is surrounded by a cirrus cloud during the entire ascent (Fig. 4b), indicating the relevance of WCBs for the formation and maintenance of the extended upper-level cirrus cloud cover associated with extratropical cyclones (Eckhardt et al., 2004; Madonna et al., 2014; Oertel et al., 2019; Joos, 2019).

~~In comparison to the slantwise WCB, the vertically integrated rain, snow and graupel water path in close proximity to the convective updraft is considerably higher~~ The denser cloud (Fig. 4a,b) ~~. This leads to a denser cloud (Fig. 4c,d)~~ with limited spatial extent (Fig. 4~~a,b~~e,f) in the convective case ~~and~~ implies a pronounced heterogeneity of the large-scale cloud structure if convection is directly embedded in the large-scale WCB ~~ascent.~~ cloud band.

A previous analysis showed that the precipitating region for the considered cyclone is spatially confined to the WCB ascent region (cf. Oertel et al., 2019, Fig. 9b). Indeed, the (normalized) number of convective and slantwise WCB trajectories starting their fastest ascent correlate both well with the evolution of the averaged (non-zero) precipitation in the WCB domain (Fig. 3b). ~~Nevertheless~~In particular, both convective ascent pulses clearly coincide with the domain-averaged precipitation maxima, suggesting that the evolution of embedded convection in the WCB has an impact on ~~precipitation intensity (cf. Oertel et al., 2019)~~the precipitation intensity (cf. Fig. 9 in Oertel et al., 2019).

The distinctly different cloud and precipitation structure between both WCB trajectory categories underlines the rationale of our classification of convective versus slantwise ascent, and agrees with typical characteristics of both precipitation types: The convective WCB ascent produces locally confined, intense precipitation including the formation of graupel, while the precipitation associated with the slantwise WCB ascent is much less intense and distributed over a larger domain whereby the ascent velocity is too slow for graupel production~~and leads to a~~. Hence, the slantwise WCB ascent forms an extended stratiform cloud band.

3.3 Thermodynamic properties

Consistent with the formation of clouds and precipitation, the convective WCB trajectories experience substantial cloud diabatic heating of on average 35 K during the first 3 h~~and~~, and they reach their outflow level at ~~around~~ the 330 K isentrope in agreement with their initial ~~θ_e value .~~ θ_e value of 330 K (Fig. 5a, cf. section 3.4). The averaged total cross-isentropic ascent of the slantwise WCB trajectories with lower θ_e in the inflow is weaker with about 28 K in 18 h when their final outflow level is reached at around 323 K ~~.~~ (Fig. 5b). The strong and localized heating in the convective updrafts leads to a local ~~increase~~ lifting of the melting level ~~height~~ (Fig. 4~~c~~a) and a localized downward deflection of the isentropes in the diabatically heated region (Fig. 6c and 5~~e~~a).

Both convective and slantwise WCB trajectories ascend only approximately along ~~constant θ_e~~ constant-θ_e surfaces (Fig. 5a,b) due to the influence of ice microphysical processes during the ascent. The calculation of ~~θ_e~~ θ_e only considers the heat released during the transition from the vapour to the liquid phase, but does not account for the additional heat release associated with the ice phase ~~(~~[the transition from the vapour to the ice phase releases the latent heat of condensation plus freezing ($L_c + L_f$), and the latter is not accounted for in the calculation of ~~θ_e)~~θ_e]. Hence, the influence of melting from falling hydrometeors and the phase transitions from liquid to ice above the 0°C isotherm are evident ~~for~~ along the WCB ascent. Following the ascent of the convective WCB trajectories, once the melting level is reached in the vicinity of the 0°C isotherm, i.e., where a transition from the solid (~~RWC~~SWC and GWC) to the liquid (~~SWC and GWC~~RWC) phase occurs (Fig. 4c), ~~θ_e~~ θ_e decreases due to melting of snow and graupel falling into the ascending air parcels (Fig. ~~6e~~5a). At higher altitudes, ~~θ_e~~ θ_e increases again due to the additional heat release in the ice phase ~~.~~ (Fig. 5a). This process of decrease and subsequent increase of ~~θ_e~~ θ_e along the ascent is also evident in the more slowly ascending WCB trajectories (Fig. ~~6d). This underlines~~ 5b), underlining the importance of microphysical processes in WCBs (Joos and Wernli, 2012; Joos and Forbes, 2016), whose effect is clearly detectable even after averaging over hundreds of trajectories. [1]

3.4 Environment for convective and slantwise WCB ascent

The rapidly ascending convective WCB trajectories originate from a slightly warmer and substantially moister region ($\theta = 296 \pm 1.3\,\mathrm{K}, q_v = 11.5 \pm 1.2\,\mathrm{g\,kg^{-1}}$) compared to the more slowly ascending slantwise WCB trajectories ($\theta = 295 \pm 1.9\,\mathrm{K}, q_v = 9.9 \pm 1.3\,\mathrm{g\,kg^{-1}}$), and are thus characterized by substantially higher initial θ_e (Figs. 6a and 5a) than the slantwise WCB trajectories (Figs. 6b and 5b). At the start of the ascent, θ_e amounts to 330 K (±4.8 K) for the convective WCB trajectories and to 324 K (±5.9 K) for the slantwise WCB trajectories (Fig. 5a,b). Although the convective ascent is embedded within the region of slantwise ascent ahead of the cold front (Figs. 3 and 6a), where θ_e contours nearly become vertical (Fig. 6c,d), the convective WCB trajectories ascend from a mesoscale, meridionally elongated region characterized by warmer and more humid conditions ahead of a strong localized θ_e gradient (Fig. 6a). This narrow tongue of very high θ_e air with q_v exceeding 11 $\mathrm{g\,kg^{-1}}$ extends laterally from ahead of the cold front only approximately 50 km into the warm sector and forms a strong horizontal θ_e gradient (Fig. 6a). Moreover, the WCB ascent region ahead of the cold frontal zone coincides with enhanced low-level convergence of the horizontal wind (Fig. 6c,d), which is particularly strong for the convective WCB trajectories. The mesoscale frontal θ_e structures ahead of the cold front arise from large θ_e variability in the warm sector. The higher θ_e of the convective WCB trajectories subsequently leads to more intense cloud diabatic processes and a faster and stronger cross-isentropic ascent (Fig. 5a,b).

[1]Note that the non-conservation of ~~θ_e~~ θ_e leads to the non-conservation of the equivalent potential vorticity (EPV) along the ascent, which is often considered to be conserved (e.g., Hitchman and Rowe, 2017) for saturated convective motion (neglecting PV modification through the solenoid effect; for details see Cao and Cho, 1995). EPV is defined as PV but with ~~θ_e~~ θ_e replacing θ (~~$EPV = \frac{1}{\rho}\boldsymbol{\omega}\cdot\nabla\theta_e$~~ $EPV = \frac{1}{\rho}\boldsymbol{\omega}\cdot\nabla\theta_e$).

The rapidly ascending, convective WCB trajectories (Fig. 5a) originate in the boundary layer from a region of strong potential instability characterized by vertical θ_e gradients of -4 K km^{-1} prior to the start of the convective ascent (Fig. 5c). After their rapid ascent from the boundary layer into the upper troposphere, the convective WCB trajectories continue to moderately ascend almost isentropically along the upper-level ridge (Fig. 5a). The convective WCB ascent is likely triggered through lifting of the potentially unstable layer in the frontal ageostrophic circulation (cf. quasi-geostrophic omega ahead of cold front in Fig. 6 and section 5.1.2 in Oertel et al., 2019). During an initial adiabatic ascent the low-level potentially unstable layer in the WCB inflow region remains potentially unstable until saturation is reached at the lifting condensation level (Schultz and Schumacher, 1999; Sherwood, 2000; Schultz et al., 2000). Once the lifting condensation level is reached, the potential instability can be released leading to the identified rapid convective updrafts ahead of the cold front.

In contrast, the slower slantwise WCB trajectories start their ascent from the boundary layer in a region characterized by weaker potential instability and lower relative humidity (Fig. 5d) and ascend on top of the (cold) frontal region characterized by comparatively large potential stability (Fig. 5b,d).

3.5 Vertical and horizontal PV structure

The PV perspective is useful to understand and trace the effect of convection on the atmospheric circulation. In this section, we investigate the 3D PV structure associated with convective and slantwise WCB ascent and describe the mechanisms that lead to the ~~observed PV distribution.~~ differing PV distributions associated with the two types of WCB ascent.

The strong localized diabatic heating during the ascent results in a PV production below and a PV destruction above the strongest ascent phase for both WCB categories (Fig. 5e,f), which is characteristic for WCB ascent (e.g., Wernli and Davies, 1997; Pomroy and Thorpe, 2000; Madonna et al., 2014). In comparison with the more slowly ascending WCB trajectories, in particular the positive PV anomaly formed by convective WCB ascent is much stronger and more localized. The ~~average~~ averaged low-level PV ~~anomaly~~ monopole below the convective WCB ascent reaches values of up to 4.5 PVU, while it remains below 1.5 PVU for the slantwise WCB ascent. In the WCB outflow, the PV values decrease to approximately 0.2 PVU for both WCB categories (Fig. 5e,f). Despite the stronger and vertically more extended positive low-level PV anomaly produced by the convective WCB trajectories, both types of WCB trajectories lead to an extended region of low-PV air ~~in the~~ directly in their outflow in the upper troposphere. In particular the outflow of the convective WCB trajectories is associated with a region of low static stability (~~$\mathrm{d}\theta/\mathrm{d}z \leq 2\,\mathrm{K\,km^{-1}}$~~$\mathrm{d}\theta/\mathrm{d}z \lesssim 2\,\mathrm{K\,km^{-1}}$, Fig. 5e, white hatching).

In the following, we examine the PV structure not only along the ~~ascent~~WCB trajectories, but also in the surroundings of the WCB ascent. Furthermore, we ~~consider the theoretical concept for PV modification as well as~~ confront the results with the theoretical concept of PV modification and consider the vorticity and static stability structure ~~within~~ in the PV anomalies.

3.5.1 Low-level positive PV ~~anomaly~~monopole

Figure 7a shows the PV structure in the lower troposphere below the mean trajectory position 30 minutes after the start of the convective WCB ascent. ~~There~~In this region, below the level of the diabatic heating maximum, the convective WCB ascent leads to the strong positive PV anomaly identified in the along-flow analysis (Fig. 5e). This mesoscale PV monopole with values up to 4 PVU extends horizontally about 30 km around the convective udpraft and is embedded within an environment with a lower-amplitude positive PV anomaly that results from the slower, slantwise WCB ascent (Fig. 7b). In contrast to the strong mesoscale PV ~~anomaly~~ monopole formed by the convective WCB ascent, the ~~PV anomaly~~ increased low-level PV values associated with the slantwise WCB ascent ~~has~~ have a lower magnitude of around 1.5 PVU. However, the PV anomaly occurs on a larger spatial scale of up to 100 km, with decreasing amplitude away from the WCB ascent. Hence, due to the stronger and more ~~localised~~ localized diabatic heating in the convective WCB trajectories (cf. section 3.2), and, as a consequence, stronger PV modification, the mesoscale ~~PV anomaly~~ low-level positive PV produced by convection is superimposed on and embedded in the PV signal resulting from the larger-scale and slower WCB ascent (Figs. 7a,b).

3.5.2 Upper-level PV dipole

In the middle to upper troposphere a coherent mesoscale horizontal PV dipole forms in the vicinity of the convective WCB trajectories, with a positive PV ~~anomaly~~ pole of magnitude 3 PVU to the right of the ~~thermal wind vector~~ vertical wind shear vector (which points in the same direction as the upper-level wind vector) and a negative PV ~~anomaly of magnitude -1.5~~pole of magnitude -1.5 PVU to the left of the ~~thermal wind~~ vertical wind shear vector (Fig. 7c,e). This PV dipole extends vertically from about 3 km (305 K) to about 9 km (330 K). The maximum amplitude of the PV dipole occurs at about 315-320 K (Fig. 7e) and coincides with the diabatic heating maximum associated with the maximum of the formation of snow and graupel (Fig. 4c). Similar to the positive PV monopole at low levels, the upper-level PV dipole also extends to about 30-40 km around the center of the convective updraft (Fig. 7c).

This distinct mesoscale PV signal emphasizes the coherent signature of the individual convective updrafts that are embedded within the complex WCB airstream. The robust mesoscale response can only be identified so clearly in the composite analysis. The large-amplitude, small-scale and, fragmentary PV features that occur in the upper troposphere in the region of embedded convection on instantaneous PV charts ~~(Fig. 9d, cf. Oertel et al., 2019, Fig. A1)~~ (Figs. 2 and 9d; see also online supplemental material) correspond to such mesoscale PV dipoles formed by the individual convective updrafts embedded in the WCB.

The formation of the PV dipole above the low-level PV monopole in our composite analysis is directly comparable to the PV structure of isolated convective updrafts in a sheared environment ~~(cf. Chagnon and Gray, 2009)~~ (cf. Fig. 2 in Chagnon and Gray, 2009) or larger-scale convective systems as discussed in the introduction. It has, however, not yet explicitly been associated with WCBs identified in reanalysis data and coarser-scale simulations, where the vertical PV dipole structure dominates (e.g., Wernli and Davies, 1997; Joos and Wernli, 2012; Madonna et al., 2014).

The composites for the slantwise WCB trajectories reveal the typical PV structure of WCBs (e.g., Wernli and Davies, 1997; Pomroy and Thorpe, 2000) with a wide region of low-PV air with a magnitude of about 0.5 PVU in the upper-tropospheric WCB outflow above the low-level positive PV anomaly (Fig. 7b,d,f and 5f). The poleward ascending low-PV air in the WCB outflow spreads out into the upper tropospheric ridge, potentially leading to its amplification (Grams et al., 2011; Madonna et al., 2014).

3.5.3 Mechanisms leading to the PV structure

~~We now~~ To analyse the mechanisms responsible for the formation of these coherent PV anomalies~~. To do so~~, we consider the material change of PV in the form of Eq. 4, which emphasizes the contributions from the vertical (first term) and horizontal (second term) vorticity components and heating gradients as discussed in the introduction (section 1.2).

The formation of the low-level positive PV anomaly is mainly due to the strong vertical heating gradient in an environment with large cyclonic vertical vorticity (first term in Eq. 4), such that below the diabatic heating maximum PV is increased (e.g., Stoelinga, 1996; Wernli and Davies, 1997; Rossa et al., 2000; Joos and Wernli, 2012; Binder et al., 2016). This mechanism is important for PV modification in both the convective and slantwise WCB trajectories, which ascend near the surface cold front, i.e., in a region where absolute vertical vorticity $f+\zeta$ is particularly large. Due to the stronger and more ~~localised~~ localized diabatic heating in the convective WCB ascent, the vertical heating gradient $\frac{\partial\dot{\theta}}{\partial z}$ is larger and, therefore, the convective WCB ascent leads to a stronger low-level positive PV anomaly. Furthermore, vortex stretching in the convective updraft additionally enhances the low-level absolute vertical vorticity~~(Fig. 8a).~~ . Together, this can lead to a positive feedback mechanism: PV is diabatically produced in the convective updraft with strong diabatic heating gradients $\frac{\partial\dot{\theta}}{\partial z}$. In consequence, the vertical vorticity is enhanced supported by vortex stretching. In the following, the diabatic heating gradient acts on amplified vertical vorticity, and thus still larger PV anomalies are produced. Finally, this results in increased PV production (cf. Joos and Wernli, 2012; Madonna et al., 2014).

The mid- to upper-level convective PV dipole results from the arrangement of horizontal vorticity and the horizontal diabatic heating gradient (second term in Eq. 4, ~~Fig. 1~~cf. Figs. 1 and 7c). Horizontal vorticity is large ahead of the upper-level trough due to strong vertical wind shear below the upper-level jet. In this case, the vertical wind shear vector of magnitude 2-3 $\mathrm{m\,s^{-1}\,km^{-1}}$ between 4-12 km height points in the same direction as the upper-level wind vector, i.e., towards the northeast (Fig. 7c). The horizontal vorticity vector ~~$\boldsymbol{\omega}_\mathrm{h}$~~ $\boldsymbol{\omega_h}$ is rotated 90° anticlockwise relative to the ~~thermal wind~~ vertical wind shear vector and points towards the cold air. Moreover, the horizontal heating gradients ~~$\nabla_\mathrm{h}\dot{\theta}$~~ $\nabla_h\dot{\theta}$ point radially towards the center of the convective updraft~~. This~~ , which coincides with the maximum heating from graupel and snow formation (Fig. 4a,e). As outlined in the introduction (section 1.2), this results in PV production to the right of the ~~thermal wind~~ vertical wind shear vector, where ~~$\nabla_\mathrm{h}\dot{\theta}\parallel\boldsymbol{\omega}_\mathrm{h}$~~$\nabla_h\dot{\theta}\parallel\boldsymbol{\omega_h}$, and PV destruction to the left of the ~~thermal wind~~ vertical wind shear vector, where ~~$\nabla_\mathrm{h}\dot{\theta}\parallel-\boldsymbol{\omega}_\mathrm{h}$.~~$\nabla_h\dot{\theta}\parallel-\boldsymbol{\omega_h}$ (Fig. 7c). The convectively produced heating gradients and the background vorticity are strong enough to form a region of absolutely negative PV. These findings from the convective WCB composites agree with the theoretical considerations in the introduction.

The horizontal diabatic heating gradients for the slantwise WCB ascent are weaker because the diabatic heating is (i) less intense and (ii) spatially more uniform due to a larger-scale gradual ascent (cf. Fig. ~~6b,d~~4d,f). Thus, the vertical component of the PV equation ~~dominates for the~~ is relatively more important than the horizontal component for the large-scale slantwise WCB ascent~~(first term in Eq. 4), where~~ , and continuous heating along the ascent leads to PV reduction above and a transport of low-PV air to the upper troposphere by the trajectories passing through this low-PV region. However, PV values remain positive because PV cannot change sign if the first term in Eq. 4 dominates (Harvey et al., 2020). We conclude that for the slantwise WCB ascent the vertical component of the PV equation is most relevant, while for embedded convection with ~~localised~~ localized and intense heating gradients the horizontal components of the PV equation are essential to explain the resulting upper-level PV dipole structure, which includes negative PV values.

3.5.4 Partitioning of PV anomalies in vorticity and static stability

Negative PV implies either hydrostatic, inertial or symmetric instablility ~~(e.g., Schultz and Schumacher, 1999; Hoskins, 2015)~~(e.g., Hoskins, 2015). In the following, we analyse the partitioning of the PV anomalies in vorticity and static stability and discuss its implication for the expected lifetime of these anomalies. ~~Figure 8b shows that the~~ The PV dipole is associated with a dipole of ~~vertical vorticity~~ absolute vertical vorticity $f+\zeta$ with similar magnitude in both poles (Fig. 8b), and thus, can be understood as the effect of tilting of horizontal vorticity by the convective updraft (cf. Chagnon and Gray, 2009). Moreover, strong heating in the convective updraft leads to increased static stability inside the updraft ($\cancel{\mathrm{d}\theta/\mathrm{dz} = 3-5\,\mathrm{K\,km^{-1}}}$$\mathrm{d}\theta/\mathrm{dz} =$ 3-5 $\mathrm{K\,km^{-1}}$; not shown) and a shallow layer of low static stability ($\cancel{\mathrm{d}\theta/\mathrm{dz} \leq 2\,\mathrm{K\,km^{-1}}}$$\mathrm{d}\theta/\mathrm{dz} \leq 2\,\mathrm{K\,km^{-1}}$, Figs. 5e and 7e) above. ~~Note that~~ The static stability is relatively uniform across both poles. Hence, the PV dipole's horizontal structure is predominantly determined by vorticity and not static stability. This is consistent with Chagnon and Gray (2009), who also found that in convective updrafts the so-called 'latent vorticity' is quickly converted to horizontal dipoles of vertical vorticity that determine the PV dipole structure.

In section 4.1 we will see that the negative PV pole, produced by convective WCB trajectories, persists for several hours. This is consistent with adjustment timescales of several hours (e.g., Thompson et al., 2018) in inertially unstable regions where $f+\zeta<0$. A convectively unstable atmosphere ($\cancel{\mathrm{d}\theta/\mathrm{dz}<0}$$\mathrm{d}\theta/\mathrm{dz}<0$), in contrast, would adjust to stability on a timescale of less than 1 h (Schultz and Schumacher, 1999).

~~For both WCB categories static stability is reduced in the upper troposphere near the WCB outflow (Fig. 7e,f, white hatching).~~ The static stability reduction above the ~~convective WCB is stronger (Fig. 7e)~~slantwise WCB is weaker compared to the convective WCB, but the slantwise WCB leads to a reduced static stability over a larger region (Fig. 7f). In the outflow of the slantwise WCB relative vorticity is weakly negative and absolute vertical vorticity is weakly positive (not shown).

The low-level positive PV anomalies for convective and slantwise WCB ascent are associated with large cyclonic vertical vorticity $f+\zeta$, whereby the convective WCB has higher values, exceeding $\cancel{6\cdot10^{-4}\mathrm{s^{-1}}}$ $6\cdot10^{-4}\,\mathrm{s^{-1}}$ (Fig. 8a), compared to the slantwise WCB with values of $\cancel{(3-4)\cdot10^{-4}\mathrm{s^{-1}}}$ (3-4) $\cdot\,10^{-4}\,\mathrm{s^{-1}}$ (not shown).

3.6 Flow anomalies induced by PV anomalies

In agreement with idealized PV inversions (e.g., Hoskins et al., 1985; Hoskins, 2015), where a positive ~~/negative~~ PV anomaly induces a cyclonic ~~/anticyclonic~~ flow anomaly, and a negative PV anomaly induces an anticyclonic circulation anomaly, respectively, the convectively produced PV ~~anomalies~~ dipoles are associated with coherent horizontal wind anomalies, calculated as the deviation of the current wind vectors from the 2-h centered mean wind vectors. The low-level positive PV ~~anomaly~~ monopole is accompanied by a cyclonic circulation anomaly with about $\cancel{4\,\mathrm{m\,s^{-1}}}$ $4\,\mathrm{m\,s^{-1}}$ higher wind speeds southeast of the convective updraft and smaller values to the northeast (Fig. 7a,e). Despite this relatively strong local wind anomaly, its radius of impact is limited and the effect of the PV anomaly substantially decays beyond 40 km from the updraft. As hypothesized by Raymond and Jiang (1990), the relatively long-lived low-level positive PV anomalies interact with the background shear, and thus could trigger new convective cells through the formation of local convergence lines on the downshear side. In this way convective activity ~~is~~ could be maintained.

The positive PV monopole from the slantwise WCB trajectories also induces a cyclonic low-level circulation anomaly (Fig. 7b). Yet, it hardly exceeds ~~$1\,\mathrm{m\,s^{-1}}$~~ $1\,\mathrm{m\,s^{-1}}$ and occurs on a larger spatial scale, in agreement with the comparatively weaker and larger-scale positive PV anomaly. The initial slantwise WCB ascent occurs directly behind the pronounced low-level jet ahead of the cold front (Fig. 7b,f). This jet, which exceeds ~~$24\,\mathrm{m\,s^{-1}}$, is~~ $24\,\mathrm{m\,s^{-1}}$, is very slightly accelerated by the diabatically produced positive PV and the associated cyclonic circulation anomaly ahead of the WCB ascent region. This pattern agrees with the synoptic situation of early WCB studies ~~(e.g., Wernli, 1997, Fig. 5)~~(e.g., Fig. 5 in Wernli, 1997), where the ascent region of the slantwise WCB is located ahead of the upper-level jet and behind the low-level jet.

The convectively produced upper-level PV ~~dipoles are~~ dipole is associated with a cyclonic and anticyclonic circulation anomaly around the positive and negative PV poles, respectively (Fig. 7c,e). The superposition of these two flows leads to a deceleration of the flow in the center of the PV dipoles and potentially stabilizes the ~~convection against rapid propagation~~ convective cloud against rapid advection with the upper-level flow (cf. Oertel, 2019, Chapter 7). At 320 K, this induced wind anomaly reaches almost ~~$3\,\mathrm{m\,s^{-1}}$~~ $3\,\mathrm{m\,s^{-1}}$ close to the convective updraft.

The weaker negative upper-level PV anomaly of the more slowly ascending WCB trajectories ~~has~~ goes along with a widespread weak anticylonic circulation anomaly (Fig. 7d) with a maximum anticyclonic wind speed anomaly of less than ~~$0.5\,\mathrm{m\,s^{-1}}$~~ $0.5\,\mathrm{m\,s^{-1}}$ northwest of the WCB ascent. The more slowly ascending WCB trajectories arrive in the upper troposphere in the vicinity of the tropopause.

In summary, both WCB categories are associated with a cyclonic low-level circulation anomaly induced by the low-level positive PV anomaly. The wind anomaly in the convective case is stronger but the extent is limited, while the wind anomaly in the slantwise WCB category is substantially weaker but extends to a larger region. In the upper troposphere two different circulation anomalies establish. The slantwise WCB ascent induces a widespread and comparatively weak anticyclonic circulation anomaly. In contrast, the anticyclonic and cyclonic circulation anomalies induced by the convectively generated PV dipole occur on a smaller scale and lead to a deceleration of the flow in the center of the convective updraft.

4 ~~An illustrative example of WCB-embedded convection~~PV anomalies on a larger scale and relevance for large-scale dynamics

Section 3 showed that the individual convective updrafts are associated with mesoscale upper-level PV dipoles that are, however, too small-scale to directly interact with the synoptic-scale balanced flow (cf. Shutts, 2017). Section 4.1 illustrates that these fragmentary PV anomalies can indeed aggregate to larger-scale PV dipole bands. Thereafter, we assess the potential for the interaction of convectively produced PV dipole bands with the synoptic-scale flow. For this, we coarse-grain the PV field with a 60-km smoothing radius (cf. Shutts, 2017; Clarke et al., 2019). More specifically, we project the original 2 km PV field to a coarser grid using a spatial moving average over 60 x 60 km^2 directly on selected isentropes.

4.1 An illustrative example of WCB-embedded convection

Figure 9 shows an instantaneous example of convection embedded in the large-scale WCB cloud structure at 09 UTC 23 Sep 2016 and serves to illustrate the typical properties and characteristics deduced from the ~~composites analysis in the~~ composite analysis in a real synoptic context. Based on this example we will discuss the lifetime of the convectively generated PV dipoles and their potential for the interaction with the larger-scale flow (section 4.1).

The large-scale WCB cloud band (Fig. 9a) is heterogeneously structured with a strong and ~~localised~~ localized production of graupel, snow and rain (Figs. 9b and 10a) ~~produced~~ caused by enhanced updrafts from embedded convection. Embedded convection, identified by rapidly ascending WCB trajectories (Fig. 9c, white contours), is predominantly located in the baroclinic region ahead of the upper-level trough (Fig. 9a and 9c, white contours). Indeed, the online trajectories' ability to identify the convective ascent is confirmed by the vertical cross-section through an embedded convective updraft (Fig. 10a): A substantial amount of hydrometeors is locally produced inside the convective updraft. This spatial coincidence of pronounced hydrometeor production within the updrafts (compare Figs. 9b,c and Fig. 10a) agrees with the results from the composite analysis (Fig. 4a,c)~~and emphasizes the heterogeneous cloud structure arising from WCB-embedded convection (Fig. 9b).~~ .

Although the upper-level PV associated with the convective updrafts is fragmented into many small-scale features (Fig. 9d), the PV structure identified in the composite analysis (cf. Fig. 7e) is clearly discernible in a vertical cross-section through the convective updraft (Fig. 10b): in the lower troposphere a strong positive PV monopole forms, which is replaced by a horizontal PV dipole centered around the convective updraft in the mid- to upper troposphere. The PV dipole extends from around 4 km to 11 km height and the PV ~~anomalies exceed ±10 PVU~~values exceed $\pm$10 PVU, leading to large horizontal PV gradients of up to 1 PVU km^{-1}.

In agreement with the composite analysis, the static stability at the height of maximum diabatic heating at around 320 K is increased (not shown), while above the heating maximum a ~~lense~~ lens of low static stability forms across the negative and positive PV poles (Fig. 10b, white contour and hatching). Thus, the mesoscale PV dipole pattern with an extent of approximately 100 km across both poles originates predominantly from the spatial variability of vertical vorticity~~.~~, in agreement with the composite analysis (Fig. 8b and section 3.5).

The composite analysis (section 3.4) revealed that the convective WCB trajectories ascend in a region characterized by substantially higher θ_e that forms a narrow elongated tongue of warm and moist air ahead of the cold front. Figure 9e emphasizes the strong heterogeneity of ~~θ_e~~ θ_e in the warm sector and confirms the spatial coincidence of rapid WCB ascent (Fig. 9e, white contours) and the ~~localised~~ localized narrow structures of high ~~θ_e~~ θ_e air. This underlines the role of the mesoscale temperature and humidity gradients for triggering convection that is directly embedded within the large-scale slantwise WCB ascent.

In the lower troposphere an elongated zone of horizontal wind convergence concurs with the convective updraft region (Fig. 9f). This low-level convergence line coincides with a band of increased low-level PV (Fig. 9f, contour lines), which ~~are generated and~~ is generated and potentially further enhanced by continuous convective ascent (cf. section 3.5).

On the larger-scale (after a coarse-graining of the PV field to a 60 x 60 ~~km^2 grid, see section 4.1~~km^2 grid), the convective region forms a meridionally elongated and narrow upper-level PV dipole band with an extension of 100 km in the across-front and more than 400 km in the along-front direction, respectively (Fig. 9c). The orientation of this dipole band is aligned with the ~~thermal wind vector.~~ vertical wind shear vector and the elongated narrow band of convective activity ahead of the cold front and the upper-level trough, and is directed to the northeast. Hence, despite the small-scale noise in the PV field formed by the individual convective updrafts (Fig. 9d), the PV anomalies spatially aggregate to a coherent and robust PV structure on the larger scale (Fig. 9c). The formation of this elongated PV dipole band parallel to the convective region is consistent with the composite analysis (Fig. 7c) and theoretical considerations (cf. Eq. 4 and Fig. 1). The formation of these PV dipole bands on either side of elongated convective ascent regions can be observed at various times ahead of the upper-level trough in this WCB case study (not shown).

A larger-scale circulation anomaly establishes around the coarse-grained PV dipole band with cyclonic and anticyclonic wind anomalies around the positive and negative poles, respectively (Fig. 9c). The wind anomalies scale with the amplitude of the PV anomalies and are particularly strong in the region where the coarse-grained PV anomalies exceed ± 2 PVU. Note that the wind anomalies are not coarse-grained, emphasizing that the organized mesoscale PV features aggregate to coherent PV anomalies~~on the large-scale~~, which are directly associated with a dynamical response on the ~~large-scale. This agrees with the electrostatics analogy of PV (Bishop and Thorpe, 1994), which suggests that locally confined PV 'charges' each induce a certain far-field effect on the flow and the superposition can be attributed to the spatially integrated PV anomaly. This implies that the linear superposition principle is applicable to PV, which denotes that the effects of individual PV anomalies on the flow field are additive (Bishop and Thorpe, 1994; Birkett and Thorpe, 1997). Although the linear superposition is only exactly valid for quasi-geostrophic PV, Thorpe and Bishop (1995) and Birkett and Thorpe (1997) suggested that the non-linear contributions for Ertel PV decrease with distance and with decreasing amplitude of the PV anomaly, and can therefore likely be neglected. This study supports their conclusion because the convective PV anomalies aggregate to coherent larger-scale PV anomalies with a distinct effect on the flow field.~~ larger scale.

The associated circulation anomaly leads to an increase of the wind speed to the northwest and southeast of the negative and positive pole, respectively, and to a deceleration of the flow in the PV dipole's center (Fig. 9c,d). Although the far-field effect of the PV anomalies reaches beyond the region where PV is directly modified, the upper-level waveguide is located more than 250 km to the ~~west~~ northwest of the convective band and, therefore, at this particular time when convection forms the PV dipole, the circulation anomaly does not yet directly influence the upper-level waveguide.

In summary, this instantaneous, Eulerian analysis of WCB-embedded convection agrees with the composite analysis in section 3 and illustrates the typical properties of WCB-embedded convection: strong and ~~localised~~ localized diabatic heating inside a dense and precipitating cloud leads to the formation of mesoscale upper-level PV dipoles that are associated with a coherent larger-scale circulation anomaly.

5 ~~PV anomalies on a larger scale and relevance for large-scale dynamics~~

4.1 Temporal evolution of the convectively generated upper-level PV dipole

~~Whereas section 3 showed that the individual convective updrafts are associated with mesoscale upper-level PV dipoles that are, however, too small-scale to directly interact with the synoptic-scale balanced flow (cf. Shutts, 2017), section 4.1 illustrated that these fragmentary PV anomalies can indeed aggregate to larger-scale PV dipole bands. In the following, we assess the potential for the interaction of these convectively produced PV dipole bands with the synoptic-scale flow. For this, the PV field is spatially averaged using a 60-km smoothing radius (cf. Shutts, 2017; Clarke et al., 2019). More specifically, we project the original 2 km PV field to a coarser grid using a spatial moving average over 60 x 60 km^2. This PV coarse-graining is performed on selected isentropes and results in a smoothed isentropic PV field with an effective resolution of 60 km.~~

~~The coarse-graining emphasizes the coherent larger-scale PV anomalies associated with the convective regions (cf. section 4.1 and Figs. 9c,d). They take the form of elongated PV dipole bands (400 x 100 km) aligned with the elongated narrow band of convective activity ahead of the cold front (Figs. 9c,d and 11a), in agreement with the PV dipole composite analysis in section 3.5. We now investigate how these PV dipole bands evolve in time and whether they interact with the large-scale PV waveguide.~~

4.2 ~~Temporal evolution of convectively generated upper-level PV dipoles~~

At the time when the PV dipole bands are formed, the associated circulation anomalies do not reach ~~to~~ the upper-level waveguide and jet stream ~~(Figs. 9c and 11a). The negative PV band is located~~ in 250 km ~~east of the upper-level trough, and the induced wind anomalies~~ distance as they are confined to within about 100 km ~~, and hence, do not directly interact with the waveguide.~~ around the PV dipole band (Figs. 9c and 11a). Yet, the temporal evolution of upper-level PV reveals that, even after the convective updrafts cease, the negative PV band persists (Fig. 11a-d): ~~During~~ The evolution of the negative PV feature under consideration (blue contour in Fig. 11 with pink shading) shows that during its relatively long lifetime of several hours, the negative PV pole is advected by the upper-level wind to the north and toward the dynamical tropopause. The negative PV appears to be approximately conserved and, a couple of hours after the convective updraft ~~ceased~~ceases, the negative PV band has approached the upper-level jet (distance now only ~~around~~ about 150 km) and the adjacent wind speed at the jet ~~has~~ is increased by approximately 5 ~~ms^{-1}~~ m s^{-1} to more than ~~60 ms^{-1}~~ 60 m s^{-1} (Fig. 11c).

To confirm the advection of the negative-PV air by the upper-level flow, forward trajectories are started inside the negative PV anomaly at the time when the PV dipole band is formed by the embedded convection (Fig. 11a, pink shading; for more details about the trajectory computation see below): The positions of these forward trajectories (Fig. 11a-d, pink shading) mostly coincide with a negative PV region, in particular within the first 3-6 h.

After 9 hours, the negative PV pole, distorted in shape due to the influence of strong horizontal wind shear in the jet region, closely approaches the waveguide and thereby strongly increases the isentropic PV gradient near the tropopause (Fig. 11d-e). The strong anticyclonic circulation anomaly associated with the negative PV anomaly accelerates the jet and forms a local jet streak (Figs. 11d,e) that is maintained for 2-3 h. This local jet intensification occurs although during advection of the negative

PV anomaly, its magnitude decreases (Fig. 11f) compared to the initial strength immediately after its formation (Fig. 10b). The area covered by negative PV values, on the other hand, increases on the considered isentrope (Figs. 11a-d, blue contours). This negative PV anomaly in the ridge ahead of the upper-level trough appears to amplify the amplitude of the pre-existing PV pattern at the waveguide. ~~With time~~

With increasing time after the initial PV dipole formation, the negative PV pole overtakes the positive PV pole (Fig. 11a-d, orange and red contours) due to strong horizontal wind shear, i.e., decreasing upper-level wind with increasing distance to the jet. In contrast to the negative PV pole that is advected towards the waveguide, the positive PV anomaly remains in the ridge and away from the waveguide.

4.2 Analysis of trajectories initialized at 09 UTC 23 Sep

The origin and fate of the ~~negative PV~~ negative-PV air is analysed in more detail using offline trajectories with 15-minute temporal resolution. For this, forward and backward trajectories ~~were~~ are computed from a region of convectively produced negative PV (Fig. 11a, pink shading). We only ~~selected~~ select trajectories with negative PV values between 315 K and 325 K that are located within a larger region of spatially averaged negative PV at 09 UTC 23 Sep ~~. At this time, which we will refer to as t=0 h, all trajectories have negative PV values and are located in a larger region of negative PV (Figs. 11a and 12a).~~ (Figs. 11a and 12a).

For the analysis of trajectories starting in the upper troposphere, offline (in contrast to online) trajectories have to be considered because the online trajectories are only started in the lower troposphere to obtain a large number of strongly ascending trajectories. Due to computational costs (memory allocation) the number of online trajectories is limited. As a consequence, online trajectories arriving in the upper toposphere have all performed a deep ascent from lower levels. However, these strongly ascending trajectories do not primarily experience the strongest PV modification (see below). Hence, the amount of available online trajectories in the target region (i.e., the region with negative PV in the upper troposphere) is too small. Finally, the online trajectories can only be computed forward, and not backward.

With the backward trajectories, however, we can infer when, relative to 09 UTC 23 Sep (which we will refer to as t=0 h~~, the negative PV~~), the negative-PV air masses acquired their negative PV and where they originate from (Fig. 12). Six hours before, less than 10% of these trajectories have negative PV values, while 3 h before, this percentage amounts to 30% (Fig. 12b, black curve). ~~At~~ After t=~~-1~~ −1 h more than 40% of trajectories ~~gain~~ additionally acquire a negative PV value through the *remote effect* of localized heating as they pass through a convectively influenced region~~(not shown), resulting in PV destruction~~ , i.e., a region to the left of the ~~thermal wind vector and the convective updraft .~~ convective updraft region and the vertical wind shear vector, where PV is reduced (cf. Fig. 1). Thus, the majority of trajectories acquires their negative PV just within the last hour while passing a convectively influenced region, predominantly located west of the convective updraft region.

From all trajectories with negative PV at t=0 h, almost 70% were previously advected quasi-isentropically with the upper-level flow and a smaller percentage of 30% ascended from the lower to the mid-troposphere (Fig. 12b, grey curves and Fig. 12c), ~~some~~ few of them inside a convective region. The percentage of upper-level trajectories with negative PV advected into the negative-PV region increases with time (Fig. 12b, solid blue curve) because upstream convection produced negative upper-level

PV 1-3 h earlier (not shown). This air mass is then advected and contributes to the larger-scale region of negative PV at t=0 h. The strongest increase of the percentage of upper-level trajectories with a negative PV value occurs at t=-1 h (Fig. 12b, solid blue curve), when strong convection sets in and ~~modifies~~ reduces the PV of the trajectories to the left of the convective updraft. Trajectories that ascend from lower levels (Fig. 12c) and contribute to the larger-scale region of negative PV at t=0 h have PV values of ~~±10PVU~~ ±10 PVU (Fig. 12a). However, the percentage of trajectories with negative PV ascending from the lower troposphere is small and does not exceed 10% (Fig. 12b, dashed blue curve).

These results suggest that the larger-scale region of upper-level negative PV consists of air masses with different origins: (i) a large percentage of trajectories (approximately 30%) with negative PV is formed by upstream convection approximately 3 h earlier and is advected quasi-isentropically by the upper-level flow; (ii) a substantial fraction of air parcels (approximately 40%) originating from the upper troposphere ~~gains negative PV~~ acquires negative PV values only within the last 1 h through local convective influence as they pass the left side of a convective updraft; (iii) only a small fraction of trajectories contributing to the upper-level negative PV at t=0 h originates from the lower to mid-troposphere with positive PV (approximately 10% of the trajectories are located in the lower troposphere and have positive PV values at t=$-$3 h), whereby these rising trajectories ~~gain~~ acquire a negative PV value during their ascent or after arrival in the upper troposphere when they pass through a convectively influenced region; (iv) the smallest fraction of less than 10% contains trajectories that ascend from lower levels with already negative PV 3 h prior to their ascent.

Although there is some uncertainty in the calculation of the offline trajectories with 15-minutes temporal resolution, these results suggest that air masses that ~~gain~~ acquire negative PV originate from a region in close proximity to convection but not necessarily from inside the convective updraft. Moreover, this indicates that the maintenance of convective ascent for at least a few hours helps to generate a larger region of negative PV through advection of ~~negative PV~~ negative-PV air from upstream convection.

Whereas the backward trajectories allowed analysing the PV history of the air parcels, the forward trajectories consider the future evolution of their PV. Within the first 3-6 h, the forward trajectories remain mostly within a negative PV region (Fig. 11a-d, pink shading) and the majority of trajectories keep their negative PV values (Fig. 12a). This emphasizes the persistence of the negative PV and supports the previous finding that the negative PV region is advected by the upper-level flow (Fig. 11). After 6 h, the trajectories spread out spatially and cover a larger region due to the strong horizontal and vertical wind shear, but 57% of the trajectories still have negative PV. The negative PV is retained for a relatively long time, and even after more than 12 h more than 50% of ~~all~~ the trajectories still have negative PV (Fig. 12a) and contribute to some extent to a widespread larger-scale negative PV anomaly (Fig. 11d-e, pink shading), which induces an anticyclonic circulation anomaly in proximity to the tropopause.

Together, these results suggest that air masses in the vicinity of convective updrafts experience strong PV destruction, which contributes to a larger region of negative PV with a coherent anticyclonic circulation anomaly. The convectively generated negative PV is ~~characterised~~ characterized by a relatively long lifetime and is advected northward towards the upper-level jet, where it interacts with the upper-level waveguide, strengthens the isentropic PV gradient and is associated with the formation of a jet streak.

4.3 ~~Convectively generated low-level positive PV anomalies~~

~~The convectively generated positive PV anomalies in the lower troposphere are characterized by a high amplitude of up to 10 PVU, and form an elongated narrow region (not shown). The spatial scale of these low-level PV anomalies is overall smaller than the upper-level PV anomalies (compare Fig. 9d and f), and after coarse-graining to 60 km the PV anomaly is smeared out and its amplitude strongly decreases to approximately 1.5-2 PVU (not shown). If a coarse-graining to 12 km is applied instead, a narrow and elongated PV band with magnitude exceeding 2-5 PVU is found (Fig. 9f). The convectively generated PV bands frequently coincide with low-level convergence lines (Fig. 9f) and are also characterized by a comparatively long lifetime. Thus, before these low-level PV stripes slowly decay, they also propagate poleward (not shown), where the induced cyclonic circulation anomaly can potentially enhance the low-level jet downstream.~~

5 Discussion and open question

In the following we discuss our results~~and~~, remaining open questions~~about the significance of embedded convection in WCBs~~, and limitations of this study. In this WCB case study, embedded convection was frequently observed and consistently associated with elongated upper-level PV dipole bands, whereby the negative PV pole was advected poleward towards the jet where it interacted with the waveguide. However, the analysis of only one case study limits the generality of the key results, i.e., the frequent occurrence of convectively produced PV dipole bands in WCBs ~~. But despite the large variability of WCB ascent behaviour~~and their influence on the upper-level jet. Due to the wide range of synoptic situations that can be associated with WCB ascent, we expect a large case-to-case variability of the resulting PV signal. For example, a case study of a WCB associated with an upper-level PV cut-off in October 2016 in the North Atlantic region generated weaker and less consistent PV dipoles (Oertel, 2019, Chapter 6).

Despite the large variability of WCB ascent behavior, we hypothesize that the WCB ascent regions are generally favorable environments for the production of PV dipole bands and the occurrence of negative PV in proximity to the tropopause ~~. While observations~~ (cf. Harvey et al., 2020), as they frequently ascend in the baroclinic region of extratropical cyclones characterized by substantial vertical wind shear. While the occurrence of negative PV in ridges of mid-latitude cyclones in proximity to the tropopause ~~have~~ has already been reported ~~(e.g., Pomroy and Thorpe, 2000; Grams et al., 2011; Chagnon et al., 2013; Rowe and Hitchman, 2016)~~from model simulations (e.g., Pomroy and Thorpe, 2000; Grams et al., 2011; Chagnon et al., 2013; Rowe and Hitchman, 2016; Harvey et al., 2020) and observations (Harvey et al., 2020), it has not yet been explicitly associated with embedded convection in WCBs. The extension of this analysis to further WCB case studies – including the investigation of embedded convection, its PV signature and its dynamical relevance – would shed light on the generality of our key results. In particular, the identified impact of embedded convection on the dynamics and precipitation pattern requires a climatological quantification of the frequency of convective versus slantwise WCB ascent. However, the investigation of numerous WCB case studies in ~~convection-resolving~~ convection-permitting models is computationally expensive, also because of the large domain covered by the WCB and the ~~inclusion of~~ need for online trajectories.

~~In addition to the increase of the tropopause sharpeness by WCBs (Chagnon et al., 2013; Chagnon and Gray, 2015), the~~ A study of an extratropical cyclone by Chagnon et al. (2013) suggested that diabatic processes do not necessarily alter the PV directly at the tropopause, but rather in its environment, resulting in the steepening of the PV gradient across the tropopause. They showed that negative PV had been diabatically modified within the WCB outflow region at the equatorward side of the upper-level waveguide, and subsequently stretched out in the ridge through non-linear advection, similarly to the behavior of the convectively generated negative PV during poleward advection into the ridge in this case study (section 4.1, Fig. 11). In their case study, the negative PV, resulting from parameterized convection, large-scale microphysical processes and boundary layer processes, was in phase with the meridional PV gradient. This resulted in the amplification of the wave, and thus was associated with faster Rossby wave growth rates and enhanced westward propagation relative to the flow. Similarly, the negative PV bands formed by WCB-embedded convection close to the tropopause are in phase with the meridional PV gradient, and thus also enhance the wave amplitude and steepen the PV gradient. Hence, the advection of the convectively generated negative PV pole towards the waveguide further enhances the horizontal PV gradient ~~in proximity to the tropopause. This~~ at the tropopause, in addition to the increase of the tropopause sharpness by the slantwise WCB ascent as reported by Chagnon et al. (2013) and Chagnon and Gray (2015). This approximation of negative PV and the waveguide also locally accelerates the jet and potentially influences the propagation of Rossby waves (Harvey et al., 2016), both highly relevant aspects for ~~NWP.~~ numerical weather prediction.

During its poleward advection towards the tropopause, the negative PV pole wraps anticyclonically due to the strong wind shear near the jet and expands in the ridge (cf. Chagnon et al., 2013). This expansion increases the influence of PV on the induced velocity, as larger-scale PV anomalies more strongly affect the velocity field (Hoskins et al., 1985). Moreover, this stresses that, although embedded convection locally strongly impacts the precipitation, cloud structure, and the mesoscale flow during the convective updraft, the impact on the large-scale dynamics occurs mostly downstream and several hours after the convective updraft ceases.

~~A study of an extratropical cyclone by Chagnon et al. (2013) showed that diabatic processes do not necessarily alter the PV directly at the tropopause, but that PV in its proximity is diabatically modified, resulting in the steepening of the PV gradient across the tropopause.They showed that negative PV had been diabatically modified within the WCB outflow on the equatorward~~ As discussed in the previous paragraph, the propagation of convectively generated bands of negative PV towards the waveguide is dynamically relevant due its impact on the tropopause sharpness, on the upper-level jet and potentially on the propagation speed of Rossby waves. This interaction of the negative PV pole with the upper-level waveguide can be observed several times during the life cycle of *Vladiana* (e.g., Fig. 11). Based on the analysis of these examples, Fig. 13 schematically illustrates the different stages of convectively generated negative PV embedded in the WCB ascent region from its initial formation to its slow decay at the anticyclonic shear side of the ~~trough, and subsequently stretched out in the ridgethrough non-linear advection, similarly to the behaviour of~~ upper-level ridge.

Initially, the ~~convectively generated negative PV during poleward advection into the ridge in this case study (section 4.1,~~ aggregation of embedded convection parallel to the upper-level jet forms a coherent larger-scale elongated PV dipole band parallel to the upper-level jet (Fig. ~~11). In their case study~~13a). After its initial formation, the negative ~~diabatic PV , resulting from parameterized convection, large-scale microphysical processes and boundary layer processes, was in phase with the meridional PV gradient, which resulted in the amplification of the wave amplitude,~~ PV band overtakes the positive PV band due to the horizontal wind shear near the jet, and ~~thus was associated with faster Rossby wave growth rates and westward propagation. Similarly, the negative~~ gets distorted in shape (Fig. 13b). This results in a re-orientation of the PV ~~band formed by WCB-embedded convection, located in~~ dipole bands, such that the distorted, almost circular negative and positive PV features are meridionally aligned, with the negative PV to the north and the positive PV pole to the south. At this stage, the PV dipoles induce a circulation anomaly towards the west that facilitates the westward propagation of the negative PV relative to the approaching waveguide, which is the prerequisite for the direct interaction between the upper-level jet and the negative PV feature. As the propagation of the negative PV band towards the waveguide is observed several times in this case study (shown exemplarily for one such event in section 4.1), we hypothesize that the induced wind field at this stage is a coherent feature that supports the advection of the negative-PV air westward relative to the approaching trough. Once the negative PV feature is located in close proximity to the ~~tropopause, is in phase with the meridional PV gradient, and thus, also enhances the wave amplitude and steepens the PV gradient.~~waveguide in the northern part of the ridge, it is distorted and stretches out (Fig. 13c), and finally forms a narrow band of negative PV directly at the anticyclonic shear side of the jet (Fig. 13d), where the magnitude of the negative PV slowly decays. Figure 13 also illustrates the acceleration of the upper-level jet (Figure 13b) and the formation of a jet streak (Figure 13c,d), when the negative PV pole approaches the upper-level jet (cf. Harvey et al., 2020).

Currently, global forecast models (e.g., IFS, MetUM, GFS) are run with a coarser resolution unable to explicitly resolve convection. This leads to the ~~questions~~ question if these schemes are able to trigger embedded convection at the right place and time and with the correct amplitude, and if the PV dipoles generated by localized ~~parameterized heating~~ heating from the convection parameterization scheme have the correct magnitude. For instance, previous studies showed that the PV anomaly's amplitude generated by the convection scheme is weaker compared to the amplitude in high-resolution ~~convection-resolving~~ convection-permitting simulations (Done et al., 2006; Clarke et al., 2019), which, in the case of a large mesoscale convective system, subsequently influenced the downstream flow evolution and decreased the forecast quality (Clarke et al., 2019). To explicitly simulate the mesoscale upper-level PV dipoles, a horizontal ~~resolution of at least 10~~grid spacing of approximately 2 km would be required to resolve the individual convective updrafts.

The organized mesoscale PV features in the convective ascent region on the original 2 km grid can aggregate to coherent PV anomalies on the large-scale, which are directly associated with a dynamical response on the large-scale. This agrees with the electrostatics analogy of PV (Bishop and Thorpe, 1994), which suggests that locally confined PV 'charges' each induce a certain far-field effect on the flow and the superposition can be attributed to the spatially integrated PV anomaly. This implies that the linear superposition principle is applicable to PV, which denotes that the effects of individual PV anomalies on the flow field are additive (Bishop and Thorpe, 1994; Birkett and Thorpe, 1997). Although the linear superposition is only exactly valid for quasi-geostrophic PV, Thorpe and Bishop (1995) and Birkett and Thorpe (1997) suggested that the non-linear contributions for Ertel-PV decrease with distance and with decreasing amplitude of the PV anomaly, and can therefore likely be neglected.

This study supports their conclusion because the convective PV anomalies aggregate to coherent larger-scale PV anomalies with a distinct effect on the flow field.

While embedded convection is directly relevant for ~~NWP~~ numerical weather prediction due to its potential impact on surface precipitation, mesoscale winds, jet speed and Rossby wave propagation, the relevance of correctly representing embedded convection in climate simulations is less obvious. Nevertheless, the misrepresentation of embedded convection in WCBs could underestimate the projected surface precipitation extremes associated with extratropical cyclones. Moreover, the large-scale cloud band of WCBs is known to modify the radiative balance (Joos, 2019), which is still a highly uncertain process in climate simulations (e.g., Boucher et al., 2013; Vial et al., 2013; Bony et al., 2015; Caldwell et al., 2016). A systematic underestimation of embedded convection and its influence on the cloud structure could potentially influence the radiative balance, because, on the one hand, convection results in a substantially denser cloud band. On the other hand, convectively generated liquid-origin cirrus clouds (cf. Krämer et al., 2016; Luebke et al., 2016; Wernli et al., 2016) spread out in the WCB outflow and travel poleward. The formation pathway of cirrus clouds leads to different microphysical and macrophysical properties (e.g., Krämer et al., 2016; Luebke et al., 2016), which can influence the cirrus cloud radiative forcing (Zhang et al., 1999; Joos et al., 2014).

~~We~~ Finally, we showed that the formation of the PV dipole through embedded convection is a relatively fast processes, while the decay of the (dynamically unstable) negative PV pole, with a lifetime of several hours, is comparatively slow. It is not yet clear which non-conservative processes, e.g., turbulence, microphysics or radiation, lead to the destruction of the negative PV in the ridge, i.e., the production of PV in regions of negative PV, and if other non-conservative processes additionally decrease PV resulting in the maintenance of the negative PV feature. A novel diagnostic to analyse the PV tendencies from each parameterization scheme available for the ECMWF's Integrated Forecasting System (Spreitzer et al., 2019; Attinger et al., 2019) would enable a detailed and systematic analysis of the processes that govern the destruction of negative PV~~, and would~~. It would also potentially shed more light on the approximate lifetime and properties of the negative PV in the upper-level ridge. In addition, idealised high-resolution simulations might provide new insights into the integral lifecycle of negative PV.

6 Conclusions

We analysed the ~~effects~~ influence of embedded convection in the WCB of the North Atlantic cyclone ~~"Vladiana"~~ *Vladiana* in Sep 2016 on the precipitation and cloud structure, and on the local mesoscale dynamics and larger-scale circulation features. For this, two categories of online WCB trajectories ~~,~~ – very rapidly ascending "convective" WCB trajectories and more slowly ascending "slantwise" WCB trajectories ~~,~~ – were identified in a convection-permitting COSMO simulation, and their impact was investigated in a composite analysis and, in more detail for a representative example. As expected from previous studies, the slantwise WCB ascent influences the large-scale precipitation pattern ~~,~~ and the hydrometeor and PV ~~distribution~~ distributions in a wide region. The specific signatures of embedded convection are superimposed on these larger-scale ~~pattern~~ patterns from the slantwise WCB ascent. Based on the composite analysis and the investigation of a representative example of embedded convection in the WCB we conclude the following:

~~The convective WCB trajectories originate from a region with higher θ_e and increased potential instability ($\mathrm{d}\theta_e/\mathrm{dz}$) at approximately 900 hPa compared to their environment, which allows for the rapid quasi-vertical convective ascent through the whole troposphere. Although convective WCB ascent is embedded within the larger-scale region of slantwise WCB ascent, mesoscale θ_e variability and strong localised θ_e gradients in the warm sector give rise to the higher initial θ_e of the convective compared to the slantwise WCB trajectories, which subsequently leads to the more intense cloud diabatic processes and the stronger cross-isentropic ascent (cf. section 1 question 1).~~

Convective WCB ascent leads to substantially stronger surface precipitation during the ascent with on average more than twice the intensity compared to the slantwise WCB ascent (cf. Oertel et al., 2019). The occurrence of embedded convection is ~~, therefore ,~~ therefore relevant for the mesoscale precipitation pattern in cyclones and for extreme surface precipitation associated with WCBs (Pfahl et al., 2014). Moreover, the strong convective updrafts allow for graupel formation, which is absent in the slantwise WCB ascent. Likewise, convective WCB ascent leads to a denser cloud structure in the convective updraft that is embedded within a larger-scale and less dense cloud band (cf. section 1 question ~~2~~1).

~~Convective WCB ascent leads to stronger low-level positive PV anomalies along the ascent~~ The convective WCB trajectories originate from a region with higher θ_e and increased potential instability ($\mathrm{d}\theta_e/\mathrm{dz}$) at approximately 900 hPa compared to their environment, which allows for the rapid quasi-vertical convective ascent through the whole troposphere. Although convective WCB ascent is embedded within the larger-scale region of slantwise WCB ascent, mesoscale θ_e variability and strong localized θ_e gradients in the warm sector give rise to the higher initial θ_e of the convective compared to the slantwise ~~and more slowly ascending WCB trajectories. The~~ WCB trajectories, which subsequently leads to more intense cloud diabatic processes and stronger cross-isentropic ascent (cf. section 1 questions 2 and 3).

The strong horizontal diabatic heating gradients associated with the localised convective WCB ascent results in the formation of mid- to upper-level horizontal PV dipoles on both sides of the convective updraft, where the negative pole (with a diameter of approximately 30 km) occurs to the left of the ~~thermal wind vector~~vertical wind shear vector (cf. Harvey et al., 2020), i.e., relatively close to the upper-level jet (cf. section 1 question ~~3~~4). The level of maximum amplitude of the PV dipole at around 315-320 K coincides approximately with the diabatic heating maximum associated with the maximum of snow and graupel formation. These convectively produced PV ~~anomalies~~ dipoles are predominantly anomalies of absolute vertical vorticity. Static stability inside the convective updraft and ~~in~~ across both poles is slightly increased compared to the environment due to strong latent heat release in the updraft. Above the updraft, at about 10 km height, a shallow region of low static stability located inside a cirrus cloud spreads out horizontally.

The low-level and upper-level ~~mesocale PV anomalies~~ mesoscale PV features of the convective WCB trajectories are associated with a coherent circulation anomaly, indicating that PV invertibility is qualitatively also valid at this scale. The positive low-level PV monopole below the convective updraft center induces a cyclonic wind anomaly resulting in a local increase ~~(decrease)~~ of the low-level wind velocity to the right ~~(left) of the thermal wind vector~~of the vertical wind shear vector, and a decrease to the left, respectively. The upper-level PV dipole is associated with cyclonic and anticyclonic circulation anomalies around the positive and negative poles, respectively ~~.~~ (cf. section 1 question 5). The superposition of the circulation anomalies induced by these PV anomalies ~~leads to a deceleration of~~ decelerates the flow near the convective updraft and potentially stabilizes the convectively generated PV dipole against the background flow ~~(cf. section 1 question 4).~~ (cf. Oertel, 2019, Chapter 7).

On the ~~larger-scale~~larger scale, the individual mesoscale PV ~~anomalies can~~dipoles can, in certain synoptic situations as in this case, aggregate to elongated PV dipole bands downstream of the convective updraft region, which are associated with coherent larger-scale circulation anomalies. The negative PV pole is characterized by a relatively long lifetime of several hours. During its lifetime it is advected close to the upper-level waveguide, where it strengthens the isentropic PV gradient. Its anticyclonic circulation anomaly can contribute to the formation of a jet streak more than 1300 km downstream of the convective updraft and the initial formation of the PV dipole. This suggests that the mesoscale PV anomalies produced by embedded convection upstream can ~~influence~~ interact with the synoptic-scale circulation, ~~and~~ the upper-level jet, and potentially influence the downstream flow evolution, and are thus dynamically relevant (cf. section 1 question ~~5).~~ 6).

Finally, our mesoscale view on the WCB reveals its heterogeneity~~and the~~. The distinction between slantwise and convective WCB trajectories emphasizes the significantly different impacts on the cloud and precipitation structure and the local mesoscale and larger-scale dynamics, whereby the convective WCB trajectories are accountable for distinct properties, such as the formation of graupel and an upper-level PV dipole, which are absent for purely slantwise ascending WCB trajectories.

Data availability. All data are available from the authors upon request.

Video supplement. Supplemental information related to this paper is available from the ETH research collection at https://doi.org/10.3929/ethz-b-000392157.

Author contributions. AO performed the simulation and the data analysis, and prepared a first version of the paper. All authors continuously discussed the results and contributed to the final manuscript.

Competing interests. The authors declare that they have no conflict of interest.

Acknowledgements. AO and MB acknowledge funding by the Swiss National Science Foundation (Project 165941). The COSMO simulations were performed at the Swiss National Supercomputing Centre (CSCS), as part of the project sm08 (2017–2019). We appreciate the data from EUMETSAT for the visualization of the WCB cloud band and would like to thank Annette K. Miltenberger for her support with the COSMO online trajectory module. Finally, we greatly appreciate the constructive and detailed feedback by Florian Pantillon and Jeffrey Chagnon which helped to further improve the quality of this article.

References

Agustì-Panareda, A., Gray, S. L., and Methven, J.: Numerical modeling study of boundary-layer ventilation by a cold front over Europe, J. Geophys. Res. Atmos., 110, D18 304, https://doi.org/10.1029/2004JD005555, 2005.

Anthes, R. A., Kuo, Y.-H., and Gyakum, J. R.: Numerical simulations of a case of explosive marine cyclogenesis, Mon. Wea. Rev., 111, 1174–1188, https://doi.org/10.1175/1520-0493(1983)111<1174:NSOACO>2.0.CO;2, 1983.

Attinger, R., Spreitzer, E., Boettcher, M., Forbes, R., Wernli, H., and Joos, H.: Quantifying the role of individual diabatic processes for the formation of PV anomalies in a North Pacific cyclone, Q. J. R. Meteorol. Soc., 145, https://doi.org/10.1002/qj.3573, 2019.

Baldauf, M., Seifert, A., Förstner, J., Majewski, D., Raschendorfer, M., and Reinhardt, T.: Operational convective-scale numerical weather prediction with the COSMO model: Description and sensitivities, Mon. Wea. Rev., 139, 3887–3905, https://doi.org/10.1175/MWR-D-10-05013.1, 2011.

Ban, N., Schmidli, J., and Schär, C.: Evaluation of the convection-resolving regional climate modeling approach in decade-long simulations, J. Geophys. Res. Atmos., 119, 7889–7907, https://doi.org/10.1002/2014JD021478, 2014.

Baumgart, M., Ghinassi, P., Wirth, V., Selz, T., Craig, G. C., and Riemer, M.: Quantitative view on the processes governing the upscale error growth up to the planetary scale using a stochastic convection scheme, Mon. Wea. Rev., 147, 1713–1731, https://doi.org/10.1175/MWR-D-18-0292.1, 2019.

Bennetts, D. A. and Hoskins, B. J.: Conditional symmetric instability - a possible explanation for frontal rainbands, Q. J. R. Meteorol. Soc., 105, 945–962, https://doi.org/10.1002/qj.49710544615, 1979.

Berman, J. D. and Torn, R. D.: The impact of initial condition and warm conveyor belt forecast uncertainty on variability in the downstream waveguide in an ECWMF case Study, Mon. Wea. Rev., 147, 4071–4089, https://doi.org/10.1175/MWR-D-18-0333.1, 2019.

Binder, H.: Warm conveyor belts: cloud structure and role for cyclone dynamics and extreme events, Ph.D. thesis No.24016, ETH Zürich, [available from www.research-collection.ethz.ch/handle/20.500.11850/164982], 2016.

Binder, H., Boettcher, M., Joos, H., and Wernli, H.: The role of warm conveyor belts for the intensification of extratropical cyclones in Northern Hemisphere winter, J. Atmos. Sci., 73, 3997–4020, https://doi.org/10.1175/JAS-D-15-0302.1, 2016.

Birkett, H. R. and Thorpe, A. J.: Superposing semi-geostrophic potential-vorticity anomalies, Q. J. R. Meteorol. Soc., 123, 2157–2163, https://doi.org/10.1002/qj.49712354318, 1997.

Bishop, C. H. and Thorpe, A. J.: Potential vorticity and the electrostatics analogy: Quasi-geostrophic theory, Q. J. R. Meteorol. Soc., 120, 713–731, https://doi.org/10.1002/qj.49712051710, 1994.

Bony, S., Stevens, B., Frierson, D. M. W., Jakob, C., Kageyama, M., Pincus, R., Shepherd, T. G., Sherwood, S. C., Siebesma, A. P., Sobel, A. H., Watanabe, M., and Webb, M. J.: Clouds, circulation and climate sensitivity, Nature Geoscience, 8, 261–268, https://doi.org/10.1038/ngeo2398, 2015.

Boucher, O., Randall, D., Artaxo, P., Bretherton, C., Feingold, G., Forster, P., Kerminen, V.-M., Kondo, Y., Liao, H., Lohmann, U., Rasch, P., Satheesh, S. K., Sherwood, S., Stevens, B., and Zhang, X. Y.: Clouds and aerosols, pp. 571–657, Cambridge University Press, Cambridge, UK, https://doi.org/10.1017/CBO9781107415324.016, 2013.

Browning, K.: Conceptual models of precipitation systems, Wea. Forecasting, 1, 23–41, https://doi.org/10.1175/1520-0434(1986)001<0023:CMOPS>2.0.CO;2, 1986.

Browning, K.: Mesoscale aspects of extratropical cyclones: An observational perspective, in: The life cycles of extratropical cyclones, edited by Shapiro, M. A. and Grønås, S., pp. 265–283, Amer. Meteorol. Soc., Boston, MA, 1999.

Caldwell, P. M., Zelinka, M. D., Taylor, K. E., and Marvel, K.: Quantifying the sources of intermodel spread in equilibrium climate sensitivity, J. Climate, 29, 513–524, https://doi.org/10.1175/JCLI-D-15-0352.1, 2016.

Cao, Z. and Cho, H.-R.: Generation of moist potential vorticity in extratropical cyclones, J. Atmos. Sci., 52, 3263–3282, https://doi.org/10.1175/1520-0469(1995)052<3263:GOMPVI>2.0.CO;2, 1995.

Chagnon, J. M. and Gray, S. L.: Horizontal potential vorticity dipoles on the convective storm scale, Q. J. R. Meteorol. Soc., 135, 1392–1408, https://doi.org/10.1002/qj.468, 2009.

Chagnon, J. M. and Gray, S. L.: A diabatically generated potential vorticity structure near the extratropical tropopause in three simulated extratropical cyclones, Mon. Wea. Rev., 143, 2337–2347, https://doi.org/10.1175/MWR-D-14-00092.1, 2015.

Chagnon, J. M., Gray, S. L., and Methven, J.: Diabatic processes modifying potential vorticity in a North Atlantic cyclone, Q. J. R. Meteorol. Soc., 139, 1270–1282, https://doi.org/10.1002/qj.2037, 2013.

Clark, P. A., Browning, K. A., and Wang, C.: The sting at the end of the tail: Model diagnostics of fine-scale three-dimensional structure of the cloud head, Q. J. R. Meteorol. Soc., 131, 2263–2292, https://doi.org/10.1256/qj.04.36, 2005.

Clarke, S. J., Gray, S. L., and Roberts, N. M.: Downstream influence of mesoscale convective systems: Part 1: influence on forecast evolution, Q. J. R. Meteorol. Soc., 145, 2933–2952, https://doi.org/10.1002/qj.3593, 2019.

Conzemius, R. J. and Montgomery, M. T.: Clarification on the generation of absolute and potential vorticity in mesoscale convective vortices, Atmos. Chem. Phys., 9, 7591–7605, https://doi.org/10.5194/acp-9-7591-2009, 2009.

Crespo, J. A. and Posselt, D. J.: A-Train-based case study of stratiform - convective transition within a warm conveyor belt, Mon. Wea. Rev., 144, 2069–2084, https://doi.org/10.1175/MWR-D-15-0435.1, 2016.

Davies, H. and Didone, M.: Diagnosis and dynamics of forecast error growth, Mon. Wea. Rev., 141, 2483–2501, https://doi.org/10.1175/MWR-D-12-00242.1, 2013.

Davis, C. A. and Weisman, M. L.: Balanced dynamics of mesoscale vortices produced in simulated convective systems, J. Atmos. Sci., 51, 2005–2030, https://doi.org/10.1175/1520-0469(1994)051<2005:BDOMVP>2.0.CO;2, 1994.

Doms, G. and Baldauf, M.: A description of the non-hydrostatic regional COSMO model. Part I: Dynamics and numerics, Report COSMO-Model 5.5, Deutscher Wetterdienst, Offenbach, Germany, [available from www2.cosmo-model.org/content/model/documentation/core/cosmoDyncsNumcs.pdf], 2018.

Done, J. M., Craig, G. C., Gray, S. L., Clark, P. A., and Gray, M. E. B.: Mesoscale simulations of organized convection: Importance of convective equilibrium, Q. J. R. Meteorol. Soc., 132, 737–756, https://doi.org/10.1256/qj.04.84, 2006.

Eckhardt, S., Stohl, A., Wernli, H., James, P., Forster, C., and Spichtinger, N.: A 15-year climatology of warm conveyor belts, J. Climate, 17, 218–237, https://doi.org/10.1175/1520-0442(2004)017<0218:AYCOWC>2.0.CO;2, 2004.

Ertel, H.: Ein neuer hydrodynamischer Wirbelsatz, Meteorol. Z., 59, 277–281, 1942.

Flaounas, E., Lagouvardos, K., Kotroni, V., Claud, C., Delanoe, J., Flamant, C., Madonna, E., and Wernli, H.: Processes leading to heavy precipitation associated with two Mediterranean cyclones observed during the HyMeX SOP1, Q. J. R. Meteorol. Soc., 142, 275–286, https://doi.org/10.1002/qj.2618, 2016.

Flaounas, E., Kotroni, V., Lagouvardos, K., Gray, S. L., Rysman, J.-F., and Claud, C.: Heavy rainfall in Mediterranean cyclones. Part 1: contribution of deep convection and warm conveyor belt, Clim. Dyn., 50, 2935–2949, https://doi.org/10.1007/s00382-017-3783-x, 2018.

Grams, C. M., Wernli, H., Boettcher, M., Čampa, J., Corsmeier, U., Jones, S. C., Keller, J. H., Lenz, C.-J., and Wiegand, L.: The key role of diabatic processes in modifying the upper-tropospheric wave guide: a North Atlantic case-study, Q. J. R. Meteor. Soc., 137, 2174–2193, https://doi.org/10.1002/qj.891, 2011.

Grams, C. M., Magnusson, L., and Madonna, E.: An atmospheric dynamics perspective on the amplification and propagation of forecast error in numerical weather prediction models: A case study, Q. J. R. Meteor. Soc., 144, 2577–2591, https://doi.org/10.1002/qj.3353, 2018.

Harrold, T. W.: Mechanisms influencing the distribution of precipitation within baroclinic disturbances, Q. J. R. Meteor. Soc., 99, 232–251, https://doi.org/10.1002/qj.49709942003, 1973.

Harvey, B., Methven, J., Sanchez, C., and Schäfler, A.: Diabatic generation of negative potential vorticity and its impact on the North Atlantic jet stream, Q. J. R. Meteorol. Soc., https://doi.org/10.1002/qj.3747, 2020.

Harvey, B. J., Methven, J., and Ambaum, M. H. P.: Rossby wave propagation on potential vorticity fronts with finite width, J. Fluid Mech., 794, 775–797, https://doi.org/10.1017/jfm.2016.180, 2016.

Hitchman, M. H. and Rowe, S. M.: On the similarity of lower-stratospheric potential vorticity dipoles above tropical and midlatitude deep convection, J. Atmos. Sci., 74, 2593–2613, https://doi.org/10.1175/JAS-D-16-0239.1, 2017.

Hoskins, B.: Potential vorticity and the PV perspective, Adv. Atmos. Sci., 32, 2–9, https://doi.org/10.1007/s00376-014-0007-8, 2015.

Hoskins, B. J., McIntyre, M. E., and Robertson, A. W.: On the use and significance of isentropic potential vorticity maps, Q. J. R. Meteorol. Soc., 111, 877–946, https://doi.org/10.1002/qj.49711147002, 1985.

Joos, H.: Warm conveyor belts and their role for cloud radiative forcing in the extratropical storm tracks, J. Climate, 32, 5325–5343, https://doi.org/10.1175/JCLI-D-18-0802.1, 2019.

Joos, H. and Forbes, R. M.: Impact of different IFS microphysics on a warm conveyor belt and the downstream flow evolution, Q. J. R. Meteorol. Soc., 142, 2727–2739, https://doi.org/10.1002/qj.2863, 2016.

Joos, H. and Wernli, H.: Influence of microphysical processes on the potential vorticity development in a warm conveyor belt: a case-study with the limited-area model COSMO, Q. J. R. Meteorol. Soc., 138, 407–418, https://doi.org/10.1002/qj.934, 2012.

Joos, H., Spichtinger, P., Reutter, P., and Fusina, F.: Influence of heterogeneous freezing on the microphysical and radiative properties of orographic cirrus clouds, Atmos. Chem. Phys., 14, 6835–6852, https://doi.org/10.5194/acp-14-6835-2014, 2014.

Krämer, M., Rolf, C., Luebke, A., Afchine, A., Spelten, N., Costa, A., Meyer, J., Zöger, M., Smith, J., Herman, R. L., Buchholz, B., Ebert, V., Baumgardner, D., Borrmann, S., Klingebiel, M., and Avallone, L.: A microphysics guide to cirrus clouds – Part 1: Cirrus types, Atmos. Chem. Phys., 16, 3463–3483, https://doi.org/10.5194/acp-16-3463-2016, 2016.

Kuo, Y.-H., Shapiro, M. A., and Donall, E. G.: The interaction between baroclinic and diabatic processes in a numerical simulation of a rapidly intensifying extratropical marine cyclone, Mon. Wea. Rev., 119, 368–384, https://doi.org/10.1175/1520-0493(1991)119<0368:TIBBAD>2.0.CO;2, 1991.

Luebke, A. E., Afchine, A., Costa, A., Grooß, J.-U., Meyer, J., Rolf, C., Spelten, N., Avallone, L. M., Baumgardner, D., and Krämer, M.: The origin of midlatitude ice clouds and the resulting influence on their microphysical properties, Atmos. Chem. Phys., 16, 5793–5809, https://doi.org/10.5194/acp-16-5793-2016, 2016.

Madonna, E., Wernli, H., Joos, H., and Martius, O.: Warm conveyor belts in the ERA-Interim dataset (1979-2010). Part I: Climatology and potential vorticity evolution, J. Climate, 27, 3–26, https://doi.org/10.1175/JCLI-D-12-00720.1, 2014.

Martínez-Alvarado, O. and Plant, R. S.: Parametrized diabatic processes in numerical simulations of an extratropical cyclone, Q. J. R. Meteorol. Soc., 140, 1742–1755, https://doi.org/10.1002/qj.2254, 2014.

Martínez-Alvarado, O., Joos, H., Chagnon, J., Boettcher, M., Gray, S. L., Plant, R. S., Methven, J., and Wernli, H.: The dichotomous structure of the warm conveyor belt, Q. J. R. Meteorol. Soc., 140, 1809–1824, https://doi.org/10.1002/qj.2276, 2014.

Martínez-Alvarado, O., Gray, S. L., and Methven, J.: Diabatic processes and the evolution of two contrasting summer extratropical cyclones, Mon. Wea. Rev., 144, 3251–3276, https://doi.org/10.1175/MWR-D-15-0395.1, 2016a.

Martínez-Alvarado, O., Madonna, E., Gray, S. L., and Joos, H.: A route to systematic error in forecasts of Rossby waves, Q. J. R. Meteorol. Soc., 142, 196–210, https://doi.org/10.1002/qj.2645, 2016b.

Miltenberger, A. K., Pfahl, S., and Wernli, H.: An online trajectory module (version 1.0) for the nonhydrostatic numerical weather prediction model COSMO, Geosci. Model Dev., 6, 1989–2004, https://doi.org/10.5194/gmd-6-1989-2013, 2013.

Miltenberger, A. K., Roches, A., Pfahl, S., and Wernli, H.: Online trajectory module in COSMO: A short user guide, COSMO Technical Report 24, 2014.

Neiman, P. J., Shapiro, M. A., and Fedor, L. S.: The life cycle of an extratropical marine cyclone. Part II: Mesoscale structure and diagnostics, Mon. Wea. Rev., 121, 2177–2199, https://doi.org/10.1175/1520-0493(1993)121<2177:TLCOAE>2.0.CO;2, 1993.

Oertel, A.: Embedded convection in warm conveyor belts, Ph.D. thesis No. 26554, ETH Zürich, 2019.

Oertel, A., Boettcher, M., Joos, H., Sprenger, M., Konow, H., Hagen, M., and Wernli, H.: Convective activity in an extratropical cyclone and its warm conveyor belt - a case-study combining observations and a convection-permitting model simulation, Q. J. R. Meteorol. Soc., 145, 1406–1426, https://doi.org/10.1002/qj.3500, 2019.

Pfahl, S., Madonna, E., Boettcher, M., Joos, H., and Wernli, H.: Warm conveyor belts in the ERA-Interim data set (1979-2010). Part II: Moisture origin and relevance for precipitation, J. Climate, 27, 27–40, https://doi.org/10.1175/JCLI-D-13-00223.1, 2014.

Pomroy, H. R. and Thorpe, A. J.: The evolution and dynamical role of reduced upper-tropospheric potential vorticity in intensive observing period one of FASTEX, Mon. Wea. Rev., 128, 1817–1834, https://doi.org/10.1175/1520-0493(2000)128<1817:TEADRO>2.0.CO;2, 2000.

Rasp, S., Selz, T., and Craig, G.: Convective and slantwise trajectory ascent in convection-permitting simulations of midlatitude cyclones, Mon. Wea. Rev., 144, 3961–3976, https://doi.org/10.1175/MWR-D-16-0112.1, 2016.

Raymond, D. J. and Jiang, H.: A theory for long-lived mesoscale convective systems, J. Atmos. Sci., 47, 3067–3077, https://doi.org/10.1175/1520-0469(1990)047<3067:ATFLLM>2.0.CO;2, 1990.

Rodwell, M. J., Magnusson, L., Bauer, P., Bechtold, P., Bonavita, M., Cardinali, C., Diamantakis, M., Earnshaw, P., Garcia-Mendez, A., Isaksen, L., Källén, E., Klocke, D., Lopez, P., McNally, T., Persson, A., Prates, F., and Wedi, N.: Characteristics of occasional poor medium-range weather forecasts for Europe, Bull. Am. Meteor. Soc., 94, 1393–1405, https://doi.org/10.1175/BAMS-D-12-00099.1, 2013.

Rossa, A., Wernli, H., and Davies, H. C.: Growth and decay of an extra-tropical cyclone's PV-tower, Meteorol. Atmos. Phys., 73, 139–156, https://doi.org/10.1007/s007030050070, 2000.

Rowe, S. M. and Hitchman, M. H.: On the role of inertial instability in stratosphere - troposphere exchange near midlatitude cyclones, J. Atmos. Sci., 72, 2131–2151, https://doi.org/10.1175/JAS-D-14-0210.1, 2015.

Rowe, S. M. and Hitchman, M. H.: On the relationship between inertial instability, poleward momentum surges, and jet intensifications near midlatitude cyclones, J. Atmos. Sci., 73, 2299–2315, https://doi.org/10.1175/JAS-D-15-0183.1, 2016.

Schäfler, A. and Harnisch, F.: Impact of the inflow moisture on the evolution of a warm conveyor belt, Q. J. R. Meteorol. Soc., 141, 299–310, https://doi.org/10.1002/qj.2360, 2015.

Schäfler, A., Craig, C., Wernli, H., Arbogast, P., Doyle, J. D., McTaggart-Cowan, R., Methven, J., Rivière, G., Ament, F., Boettcher, M., Bramberger, M., Cazenave, Q., Cotton, R., Crewell, S., Delanoë, J., Dörnbrack, A., Ehrlich, A., Ewald, F., Fix, A., Grams, C. M., Gray, S. L., Grob, H., Groß, S., Hagen, M., Harvey, B., Hirsch, L., Jacob, M., Kölling, T., Konow, H., Lemmerz, C., Lux, O., Magnusson, L., Mayer, B., Mech, M., Moore, R., Pelon, J., Quinting, J., Rahm, S., Rapp, M., Rautenhaus, M., Reitebuch, O., Reynolds, C. A., Sodemann, H., Spengler, T., Vaughan, G., Wendisch, M., Wirth, M., Witschas, B., Wolf, K., and Zinner, T.: The North Atlantic Waveguide and Downstream Impact Experiment, Bull. Am. Meteor. Soc., 99, 1607–1637, https://doi.org/10.1175/BAMS-D-17-0003.1, 2018.

Schemm, S.: Conveyor belts in idealized moist baroclinic wave life cycles, Ph.D. thesis No.20940, ETH Zürich, https://doi.org/10.3929/ethz-a-7632512, [https://www.research-collection.ethz.ch/handle/20.500.11850/65088], 2013.

Schmetz, J., Pili, P., Tjemkes, S., Just, D., Kerkmann, J., Rota, S., and Ratier, A.: An introduction to Meteosat Second Generation (MSG), Bull. Am. Meteor. Soc., 83, 977–992, https://doi.org/10.1175/1520-0477(2002)083<0977:AITMSG>2.3.CO;2, 2002.

Schultz, D. M. and Schumacher, P. N.: The use and misuse of conditional symmetric instability, Mon. Wea. Rev., 127, 2709–2732, https://doi.org/10.1175/1520-0493(1999)127<2709:TUAMOC>2.0.CO;2, 1999.

Schultz, D. M., Schumacher, P. N., and Doswell, C. A.: The intricacies of instabilities, Mon. Wea. Rev., 128, 4143–4148, https://doi.org/10.1175/1520-0493(2000)129<4143:TIOI>2.0.CO;2, 2000.

Selz, T. and Craig, G.: Upscale error growth in a high-resolution simulation of a summertime weather event over Europe, Mon. Wea. Rev., 143, 813–827, 2015.

Sherwood, S. C.: On moist instability, Mon. Wea. Rev., 128, 4139–4142, https://doi.org/10.1175/1520-0493(2000)129<4139:OMI>2.0.CO;2, 2000.

Shutts, G.: Idealized numerical simulations of mesoscale convective systems and their implications for forecast error, Q. J. R. Meteorol. Soc., 143, 1608–1619, https://doi.org/10.1002/qj.3031, 2017.

Siedersleben, S. K. and Gohm, A.: The missing link between terrain-induced potential vorticity banners and banded convection, Mon. Wea. Rev., 144, 4063–4080, https://doi.org/10.1175/MWR-D-16-0042.1, 2016.

Spreitzer, E., Attinger, R., Boettcher, M., Forbes, R., Wernli, H., and Joos, H.: Modification of potential vorticity near the tropopause by nonconservative processes in the ECMWF model, J. Atmos. Sci., 76, 1709–1726, https://doi.org/10.1175/JAS-D-18-0295.1, 2019.

Stoelinga, M. T.: A potential vorticity-based study of the role of diabatic heating and friction in a numerically simulated baroclinic cyclone, Mon. Wea. Rev., 124, 849–874, https://doi.org/10.1175/1520-0493(1996)124<0849:APVBSO>2.0.CO;2, 1996.

Thompson, C. F., Schultz, D. M., and Vaughan, G.: A global climatology of tropospheric inertial instability, J. Atmos. Sci., 75, 805–825, https://doi.org/10.1175/JAS-D-17-0062.1, 2018.

Thorpe, A. J. and Bishop, C. H.: Potential vorticity and the electrostatics analogy: Ertel-Rossby formulation, Q. J. R. Meteorol. Soc., 121, 1477–1495, https://doi.org/10.1002/qj.49712152612, 1995.

Tiedtke, M.: A comprehensive mass flux scheme for cumulus parameterization in large-scale models, Mon. Wea. Rev., 117, 1779–1800, https://doi.org/10.1175/1520-0493(1989)117,1779:ACMFSF.2.0.CO;2, 1989.

Vial, J., Dufresne, J.-L., and Bony, S.: On the interpretation of inter-model spread in CMIP5 climate sensitivity estimates, Clim. Dyn., 41, 3339–3362, https://doi.org/10.1007/s00382-013-1725-9, 2013.

Volonté, A., Clark, P. A., and Gray, S. L.: The role of mesoscale instabilities in the sting-jet dynamics of windstorm Tini, Q. J. R. Meteorol. Soc., 144, 877–899, https://doi.org/10.1002/qj.3264, 2018.

Volonté, A., Clark, P. A., and Gray, S. L.: Idealised simulations of cyclones with robust symmetrically-unstable sting jets, Weather Clim. Dynam. Discuss., pp. 1–38, https://doi.org/10.5194/wcd-2019-8, 2019.

Weijenborg, C., Friederichs, P., and Hense, A.: Organisation of potential vorticity on the mesoscale during deep moist convection, Tellus, 67, 25 705, https://doi.org/10.3402/tellusa.v67.25705, 2015.

Weijenborg, C., Chagnon, J. M., Friederichs, P., Gray, S. L., and Hense, A.: Coherent evolution of potential vorticity anomalies associated with deep moist convection, Q. J. R. Meteorol. Soc., 143, 1254–1267, https://doi.org/10.1002/qj.3000, 2017.

Wernli, H.: A Lagrangian-based analysis of extratropical cyclones. II: A detailed case-study, Q. J. R. Meteor. Soc., 123, 1677–1706, https://doi.org/10.1002/qj.49712354211, 1997.

Wernli, H. and Davies, H. C.: A Lagrangian-based analysis of extratropical cyclones. I: The method and some applications, Q. J. R. Meteor. Soc., 123, 467–489, https://doi.org/10.1256/smsqj.53810, 1997.

Wernli, H., Dirren, S., Liniger, M. A., and Zillig, M.: Dynamical aspects of the life cycle of the winter storm 'Lothar' (24 – 26 December 1999), Q. J. R. Meteor. Soc., 128, 405–429, https://doi.org/10.1256/003590002321042036, 2002.

Wernli, H., Boettcher, M., Joos, H., Miltenberger, A. K., and Spichtinger, P.: A trajectory-based classification of ERA-Interim ice clouds in the region of the North Atlantic storm track, Geophys. Res. Letters, 43, 6657–6664, https://doi.org/10.1002/2016GL068922, 2016.

Zhang, Y., Macke, A., and Albers, F.: Effect of crystal size spectrum and crystal shape on stratiform cirrus radiative forcing, Atmos. Res., 52, 59–75, https://doi.org/10.1016/S0169-8095(99)00026-5, 1999.

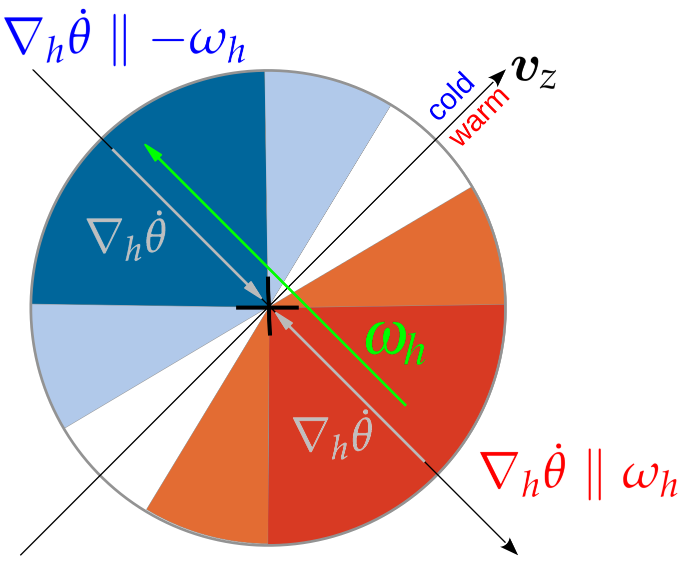

Figure 1. Conceptual model of upper-level PV modification by a convective updraft (+) that is located in an environment with background horizontal vorticity. Shown are ~~thermal~~ vertical wind shear vector ($\cancel{\mathbf{v_T}}$ $\boldsymbol{v_z}$, black) with the cold air on the left, the horizontal vorticity vector ($\cancel{\boldsymbol{\omega}_\mathrm{h}}$ $\boldsymbol{\omega_h}$, green), the diabatic heating gradients pointing radially toward the convective updraft ($\cancel{\nabla_\mathrm{h}\dot{\theta}}$ $\nabla_h\dot{\theta}$, ~~red~~grey), and the regions where PV is destroyed (blue ~~hatching~~shading) and where PV is generated (red ~~hatching~~shading), because $\cancel{\nabla_\mathrm{h}\dot{\theta} \parallel -\boldsymbol{\omega}_\mathrm{h}}$ $\nabla_h\dot{\theta} \parallel -\boldsymbol{\omega_h}$ and $\cancel{\nabla_\mathrm{h}\dot{\theta} \parallel \boldsymbol{\omega}_\mathrm{h}}$ $\nabla_h\dot{\theta} \parallel \boldsymbol{\omega_h}$, respectively ~~(~~[cf. ~~eq~~Eq. 4 ~~)~~and Schemm (2013)]. The ~~density~~ intensity of the ~~hatching~~ blue and red shading schematically ~~represents~~ represent the degree of PV change. See text for details. Note that the orientation of the vertical wind shear vector and the PV dipole schematically represents the synoptic situation shown in Fig. 7c.

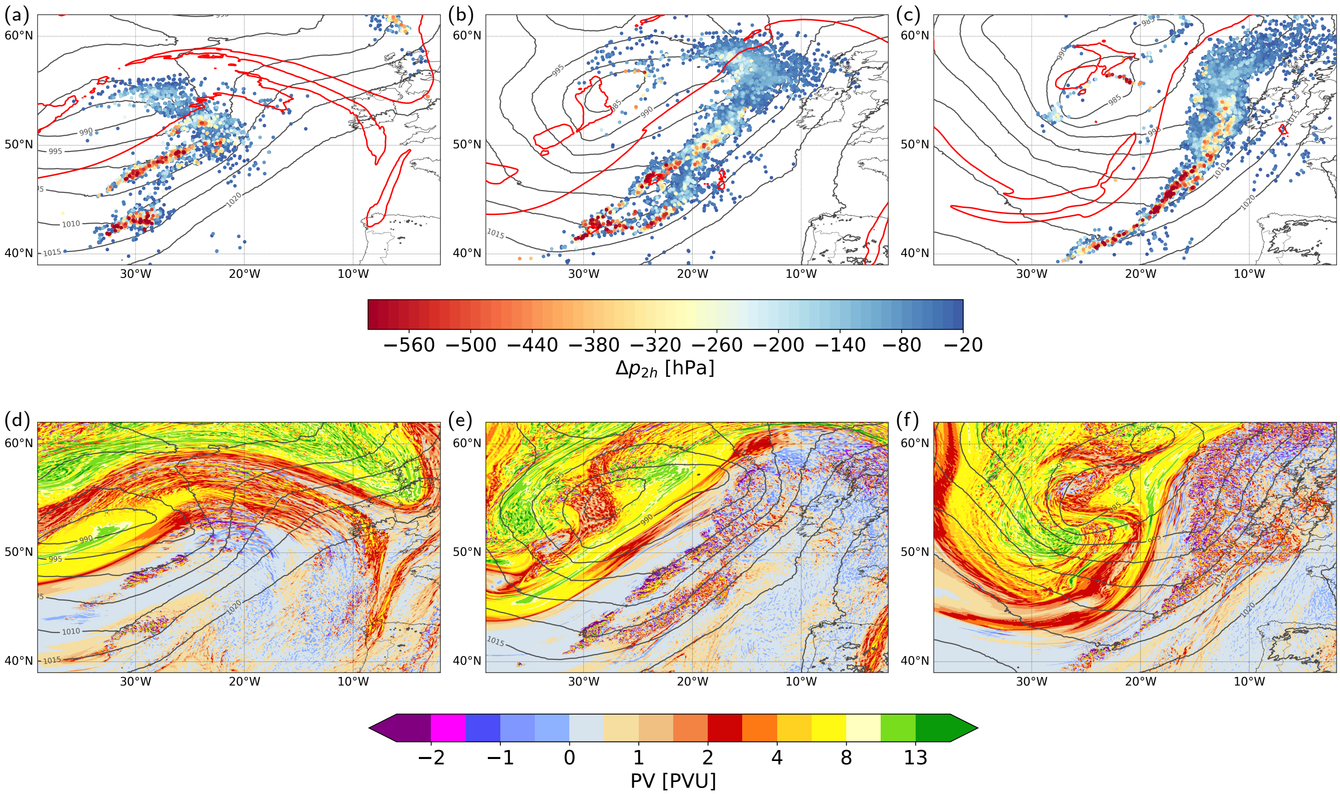

Figure 2. Overview of the WCB ascent for cyclone *Vladiana*: **(a-c)** locations of WCB air parcel ascent (circles; colors indicate centered 2-h pressure change (Δp_{2h}) along all ascending WCB trajectories, in hPa), SLP (grey contours, in hPa) and 2-PVU at 320 K (red line) for (from **a** to **c**) 22 UTC 22 Sep, 10 UTC 23 Sep, and 22 UTC 23 Sep. **(d-f)** PV at 320 K and SLP (grey contours, in hPa) for the same times as **(a-c)**.

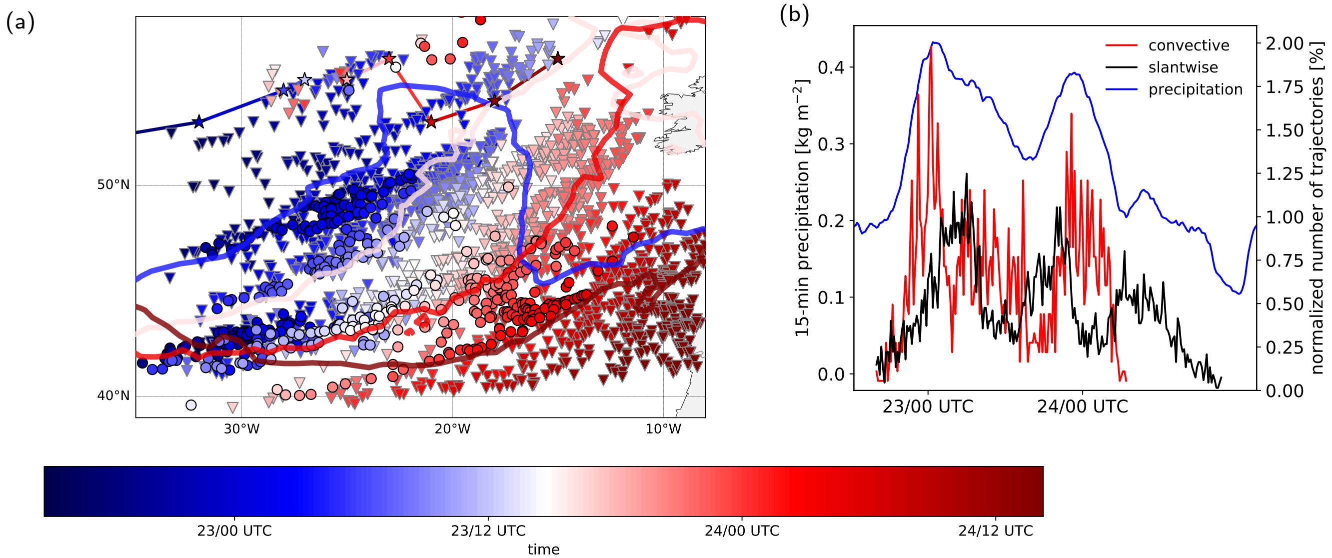

Figure 3. (a) Location of convective (black outlined circles) and slantwise (grey outlined ~~triangle~~triangles) WCB trajectories at the start of the fastest 400-hPa ascent phase. ~~Color indicates~~ Colors indicate the according time ~~evolution~~ of the WCB air parcel position (blue 23 Sep, red 24 Sep). Only every 4^{th} trajectory is shown. The evolution of the frontal ~~structure~~ structures is indicated by θ=293 K at 850 hPa (~~contours, every 0.5 K starting at 292 K) of~~ lines are colored according to the selected times ~~(10~~at 04 UTC 23 Sep, 16 UTC 23 Sep, 04 UTC 24 Sep and ~~22~~16 UTC 24 Sep). The asterisks indicate the location of the surface cyclone every 6 h (colored according to time). **(b)** Temporal evolution of the number of selected convective (red) and slantwise (black) WCB trajectories at the start of the fastest 400-hPa ascent phase normalized by the absolute number of selected trajectories in each category and evolution of 15-minute accumulated precipitation averaged over the WCB domain shown in **(a)**. Note that for the domain-averaged precipitation only grid points with non-zero precipitation were considered.

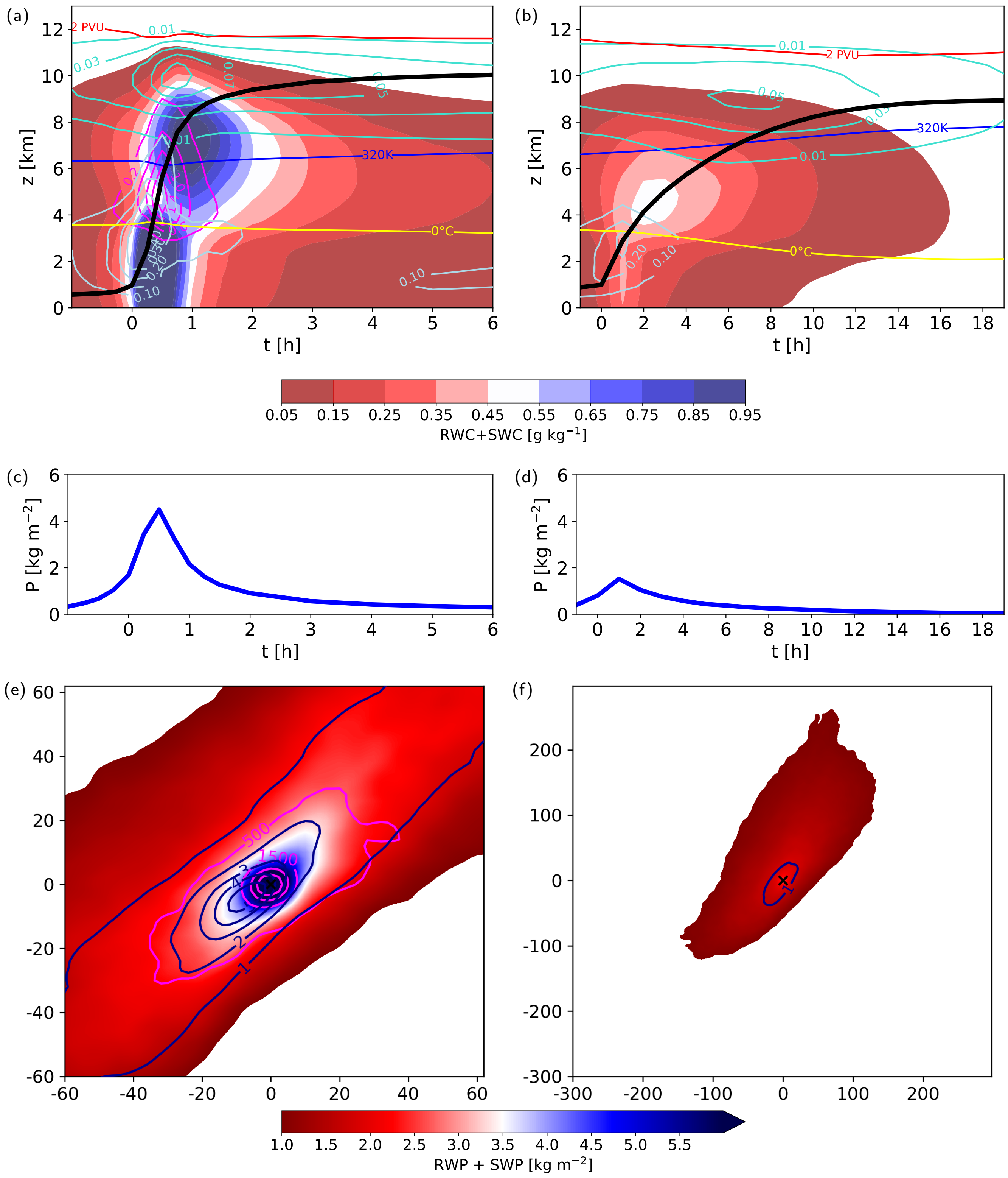

(a)
(b)
2 PVU
0.01
0.03
0.05
0.07
320K
0°C
0.10
0.20
z [km]
t [h]
RWC+SWC [g kg^{-1}]
0.05
0.15
0.25
0.35
0.45
0.55
0.65
0.75
0.85
0.95
(c)
(d)
P [kg m^{-2}]
(e)
(f)
500
1500
RWP + SWP [kg m^{-2}]
1.0
1.5
2.0
2.5
3.0
3.5
4.0
4.5
5.0
5.5

Figure 4. (a,b) Composites of vertical profiles following the motion of the trajectories (black line shows the mean ascent of all WCB trajectories) for **(a)** convective WCB trajectories and **(b)** slantwise WCB trajectories for hydrometeors [sum of rain and snow water content (RWC + SWC, colors, in $\mathrm{g\,kg^{-1}}$), ice water content (IWC, turquoise contours, every $0.02\,\mathrm{g\,kg^{-1}}$), liquid water content (LWC, light blue contours, every $0.1\,\mathrm{g\,kg^{-1}}$), graupel water content (GWC, magenta contours, every $0.4\,\mathrm{g\,kg^{-1}}$), 0°C-isotherm (yellow line), 320-K isentrope (blue line) and the 2-PVU tropopause (red line). **(c,d)** 15-minute accumulated surface precipitation along the ascent of the **(c)** convective and **(d)** slantwise WCB trajectories (blue line, in $\mathrm{kg\,m^{-2}}$). **(e,f)** Horizontal cross-section composites of vertically integrated rain and snow water content (RWP + SWP, colors, in $\mathrm{kg\,m^{-2}}$), vertically integrated graupel water content (magenta contours, every $500\,\mathrm{g\,m^{-2}}$) and 15-minute accumulated surface precipitation (blue contours, every $1\,\mathrm{kg\,m^{-2}}$) for **(a)** convective WCB trajectories 30 minutes and **(b)** slantwise WCB trajectories 1 h after the start of the fastest 400-hPa ascent (corresponding to the respective times of maximum surface precipitation). The axes' dimensions denote the distance from the WCB air parcel locations marked as '×' (in km). Note the different time axis of **(a,c)** and **(b,d)** and the different horizontal dimensions of **(e)** and **(f)**.

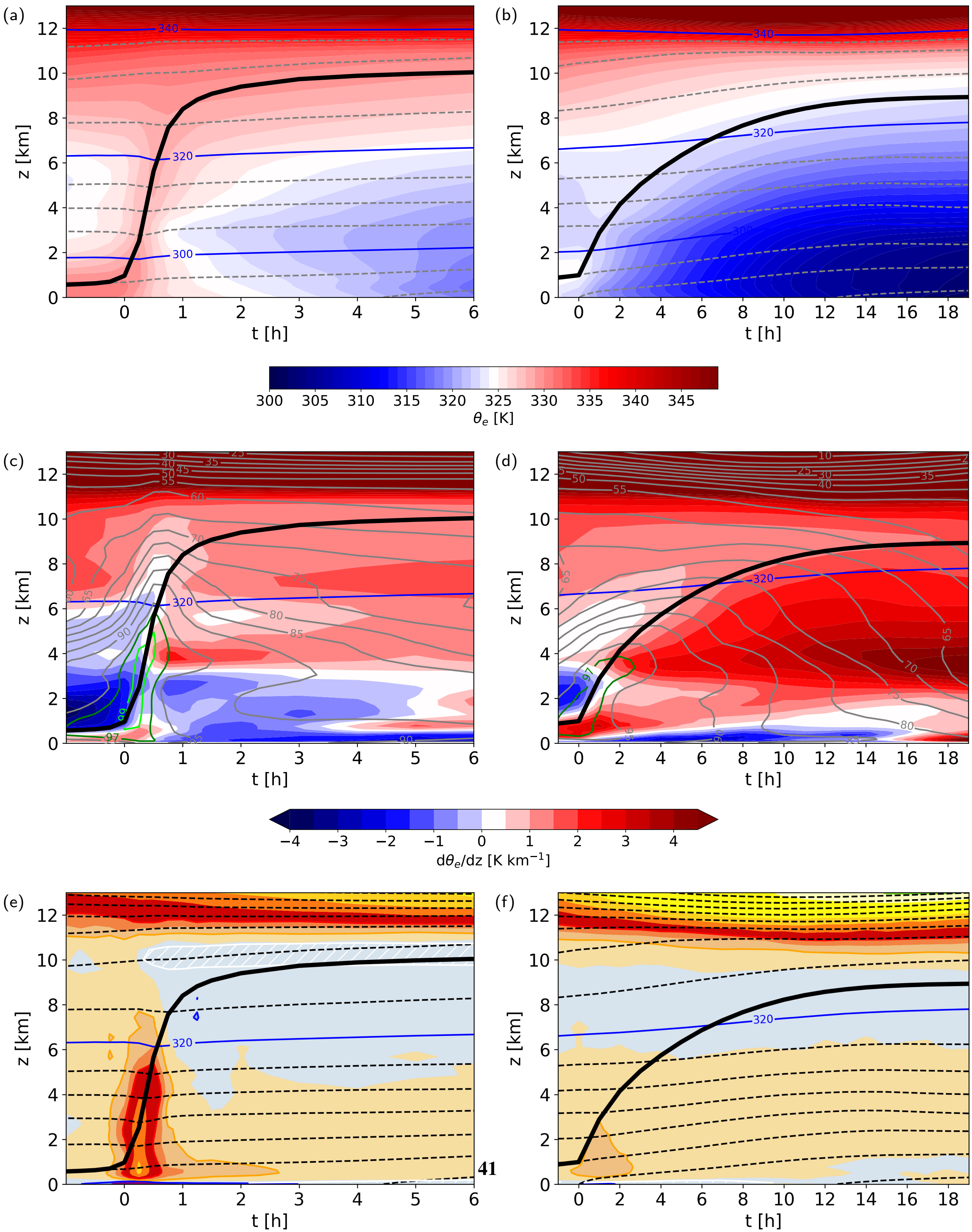
(a)
(b)
(c)
(d)
(e)
(f)
z [km]
t [h]
θe [K]
300 305 310 315 320 325 330 335 340 345
dθe/dz [K km−1]
−4 −3 −2 −1 0 1 2 3 4
340
320
300

Figure 5. Composites of vertical profiles following the motion of the trajectories (black line shows the mean ascent of all WCB trajectories) for **(a,c,e)** convective WCB trajectories and **(b,d,f)** slantwise WCB trajectories for **(a,b)** equivalent potential temperature (θ_e, colors, in K), potential temperature (θ, grey dashed lines, every 5 K) and the 300, 320 and 340-K isentrope (blue lines); **(c,d)** moist stability ($\mathrm{d}\theta_e/\mathrm{dz}$, colors, in $\mathrm{K\,km^{-1}}$), the 320-K isentrope (blue line), and relative humidity (RH, grey contours, in %; 97% and 99% RH contours are highlighted in green and lime); **(e,f)** PV (colors, in PVU), isentropes (dashed lines, every 5 K), the 320-K isentrope (blue line), and in **(e)** low static stability layers ($\mathrm{d}\theta/\mathrm{dz} \leq 2\,\mathrm{K\,km^{-1}}$, white contour and hatching). Note the different time axis in **(a,c,e)** and **(b,d,f)**.

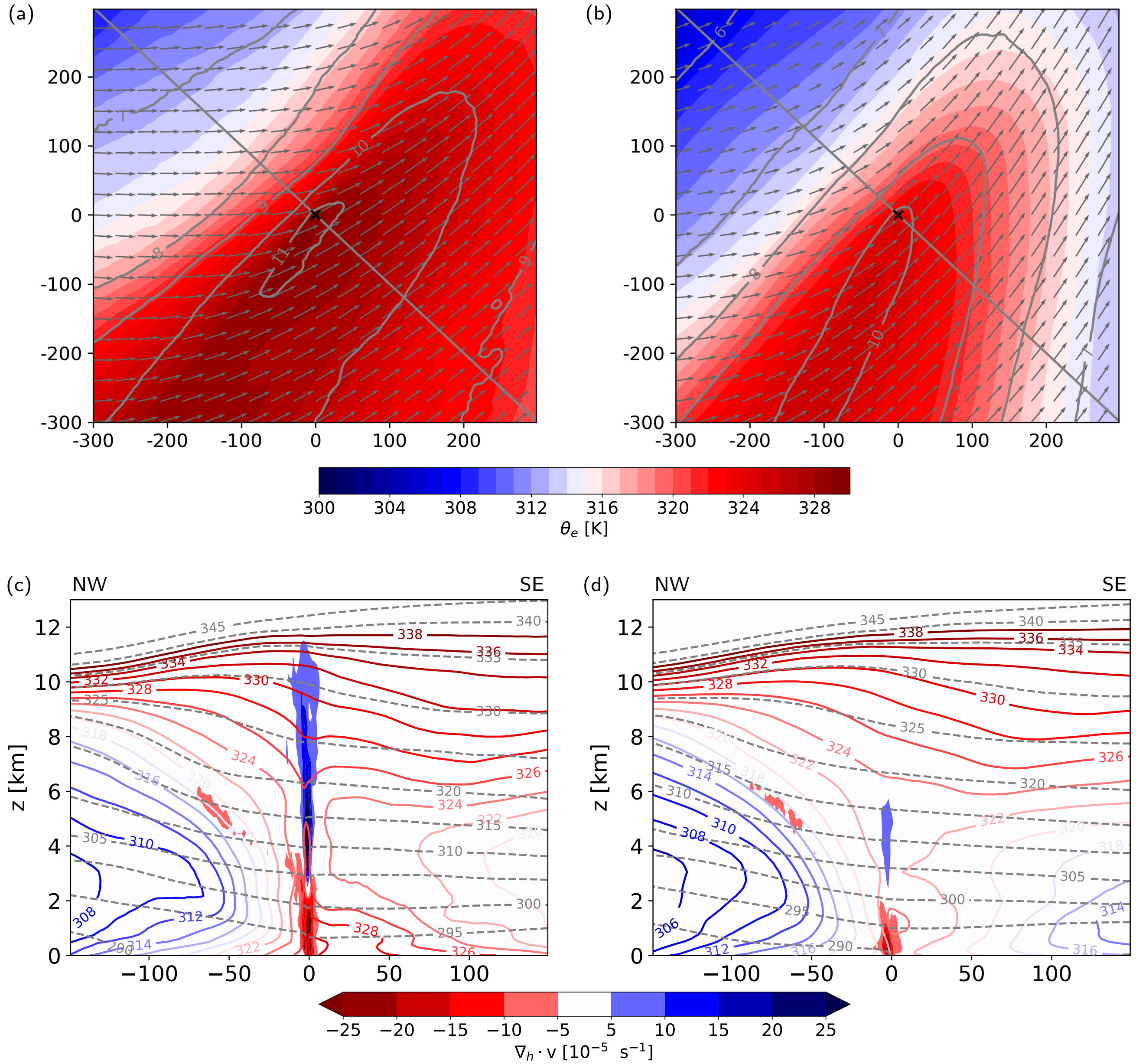

Figure 6. (a,b) Horizontal cross-section composites of θ_e at 900 hPa (colors, in K), specific humidity (grey contours, every 1 g kg^{-1}) and wind at 900 hPa (arrows) for **(a)** convective WCB trajectories and **(b)** slantwise WCB trajectories at the start of the fastest 400 hPa-ascent. The axes' dimensions denote the distance from the WCB air parcel locations marked as '$\times$' (in km). **(c,d)** Vertical cross-section composite along the northwest-southeast orientated lines shown in **(a,b)** for horizontal wind divergence (colors, in s^{-1}), equivalent potential temperature (θ_e, red - blue lines, every 2 K) and potential temperature (θ, grey dashed lines, every 5 K) for **(c)** convective and **(d)** slantwise WCB trajectories at the start of the fastest 400-hPa ascent. The x-axis denotes the zonal distance from the WCB air parcel locations (in km).

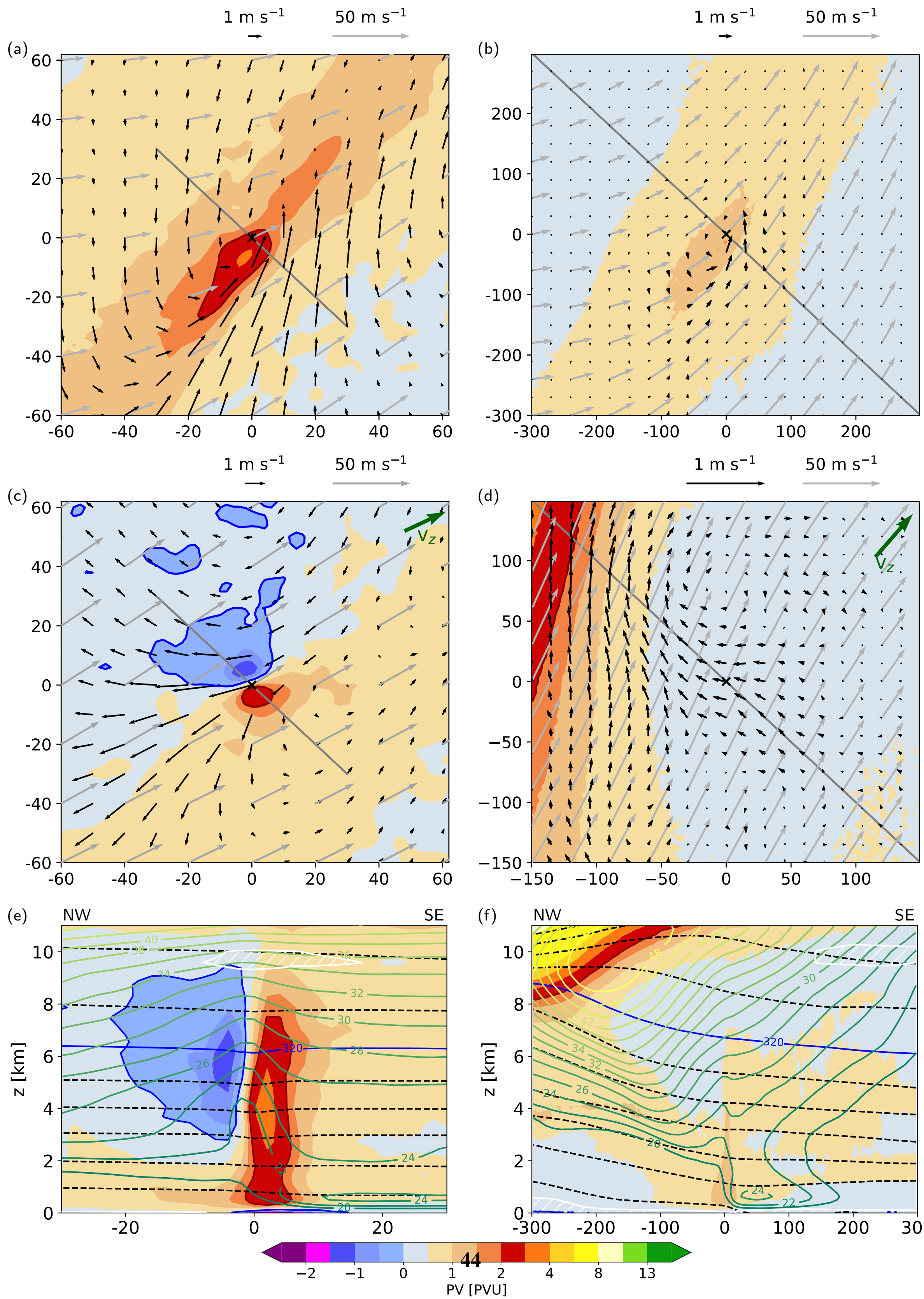

(a)
(b)
(c)
(d)
(e)
(f)
1 m s^{-1}
50 m s^{-1}
v_z
NW
SE
z [km]
PV [PVU]

Figure 7. **(a-d)** Horizontal cross-section composites of PV (colors, in PVU), wind speed (grey arrows, in $\mathrm{m\,s^{-1}}$) and 2-h circulation anomalies (black arrows, in $\mathrm{m\,s^{-1}}$) at **(a,b)** 800 m and **(c,d)** 320 K for **(a,c)** convective WCB trajectories 30 minutes after the start of the fastest 400-hPa ascent, and for **(b,d)** slantwise WCB trajectories **(b)** 1 h and **(d)** 10 h after the start of the fastest 400-hPa ascent. The green arrow in **(c,d)** shows the direction of the vertical wind shear vector ($\boldsymbol{v_z}$) between 4 and 10 km height at the location of WCB ascent. The axes' dimensions denote the distance from the WCB air parcel locations marked as '$\times$' (in km). **(e,f)** Vertical cross-section composites along the northwest-southeast orientated lines shown in **(a,b)** of PV (colors, in PVU), wind speed (green contours, every $2\,\mathrm{m\,s^{-1}}$), isentropes (dashed lines, every 5 K), the 320-K isentrope (blue line) and low static stability layers ($\mathrm{d}\theta/\mathrm{dz} \leq 2\,\mathrm{K\,km^{-1}}$, white contour and hatching) for **(e)** convective WCB trajectories 30 minutes and **(f)** slantwise WCB trajectories 1 h after the start of the fastest 400-hPa ascent. The x-axis denotes the zonal distance from the WCB air parcel locations (in km). Note the different spatial dimensions for the convective and slantwise WCB trajectories.

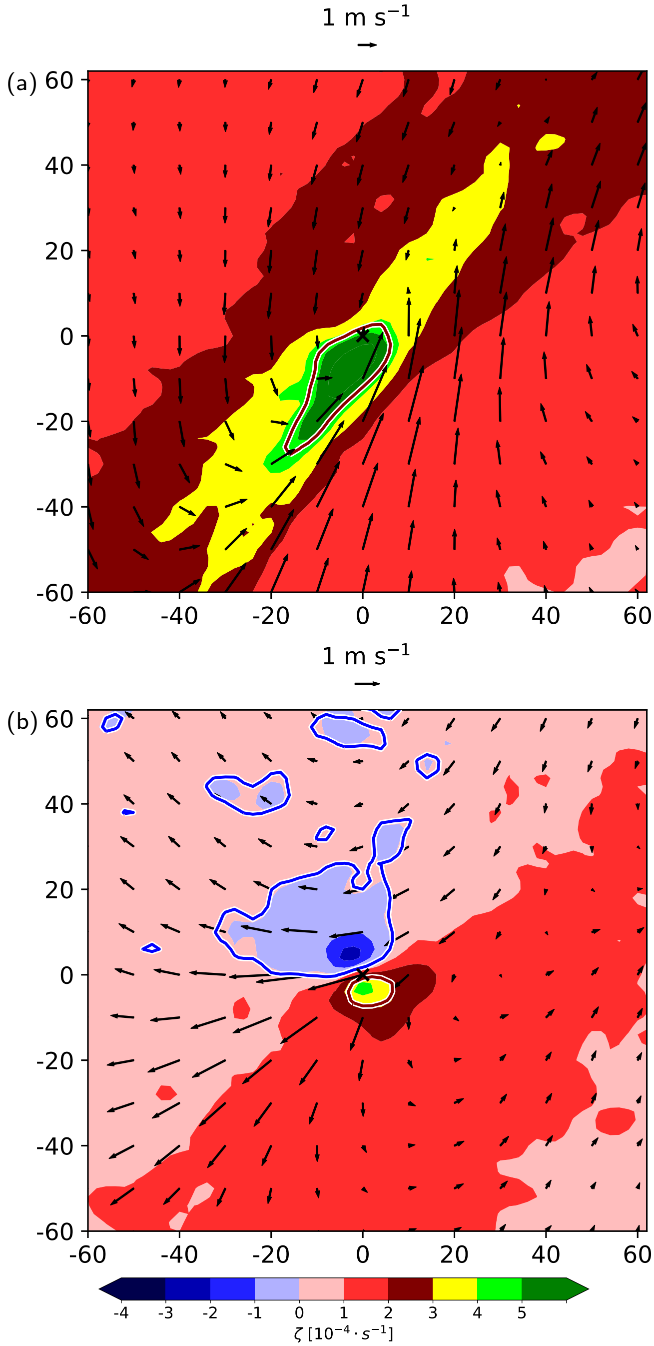

Figure 8. As Fig. 7a,c but for absolute vertical vorticity ($f+\zeta$, colors, in s^{-1}) and 2-h circulation anomalies (black arrows, in m s^{-1}) at **(a)** 800 m and **(b)** 320 K for convective WCB trajectories 30 minutes after the start of the fastest 400-hPa ascent. The 0 and 2-PVU contour lines are shown in blue and red, respectively.

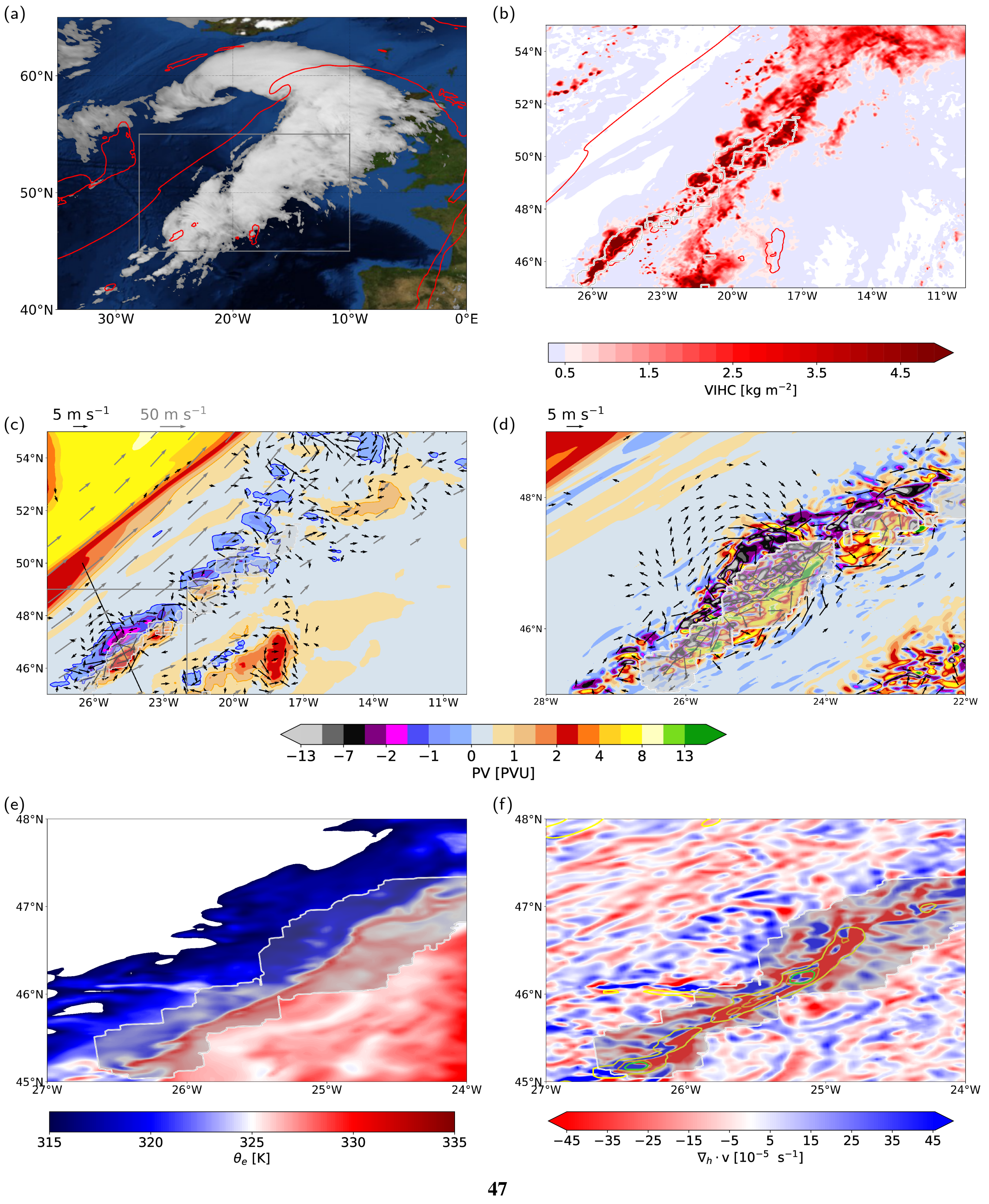
(a)
(b)
VIHC [kg m^{-2}]
(c)
5 m s^{-1}
50 m s^{-1}
(d)
5 m s^{-1}
PV [PVU]
(e)
θ_e [K]
(f)
$\nabla_h \cdot v$ [10^{-5} s^{-1}]

Figure 9. Example of embedded convection in the WCB at 09 UTC 23 Sep 2016. **(a)** Pseudo-IR satellite image of the large-scale cloud structure [data from 10.8 μm channel, EUMETSAT, Schmetz et al. (2002)] and 2-PVU contour at 320 K (red line); **(b)** vertically integrated hydrometeor content (VIHC, in kg m^{-2}, colors for VIHC>5 g m^{-2}) for the region outlined in **(a)** (grey box), envelope of rapid WCB ascent (white outline, WCB trajectory ascent $>$320 hPa in 2 h) and 2-PVU contour at 320 K (red line); **(c)** coarse-grained PV at 320 K (colors, in PVU; purple, blue, orange and red contour lines show -1, 0, 1 and 2 PVU; see text for details), 2-h circulation anomalies at 320 K (black arrows), wind speed at 320 K (grey arrows) and envelope of rapid WCB ascent (white outline); **(d)** enlargement of embedded convection shown in **(c)** (grey box) with PV at 320 K from the original 2-km model grid, 2-h circulation anomalies at 320 K (black arrows) and envelope of rapid WCB ascent (white outline); **(e)** enlargement of embedded convection shown in **(c)** with equivalent potential temperature at 900 hPa (θ_e, colors, in K) and envelope for rapid WCB ascent (white outline); **(f)** as **(e)** but for low-level wind divergence at 295 K (colors, in s^{-1}), PV (coarse-grained to 12 km) at 295 K (yellow, lime and magenta contour lines at 2, 4, and 5 PVU) and envelope of rapid WCB ascent (white outline).

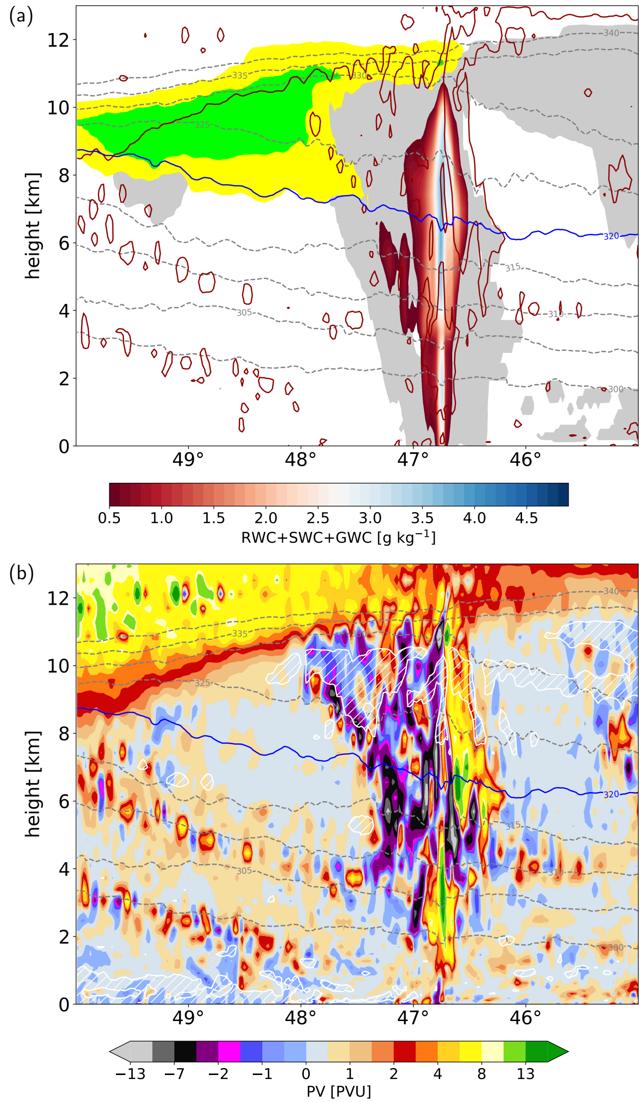

Figure 10. Vertical cross-section through the PV dipole shown in Fig. 9c (black line) at 09 UTC 23 Sep 2016 for **(a)** sum of rain, snow and graupel water content (RWC + SWC + GWC, colors, in $\mathrm{g\,kg^{-1}}$), cloudy region (grey shading, hydrometeor content $> 1\,\mathrm{mg\,kg^{-1}}$), upper-level jet (yellow and green shading at 55 and $60\,\mathrm{m\,s^{-1}}$) and 2-PVU contour (dark red line), and **(b)** PV (colors, in PVU) and low static stability layers ($d\theta/dz \leq 2\,\mathrm{K\,km^{-1}}$, white contour and hatching). Isentropes (dashed contours, every 5 K) and the 320-K isentrope (blue line) are shown in both panels.

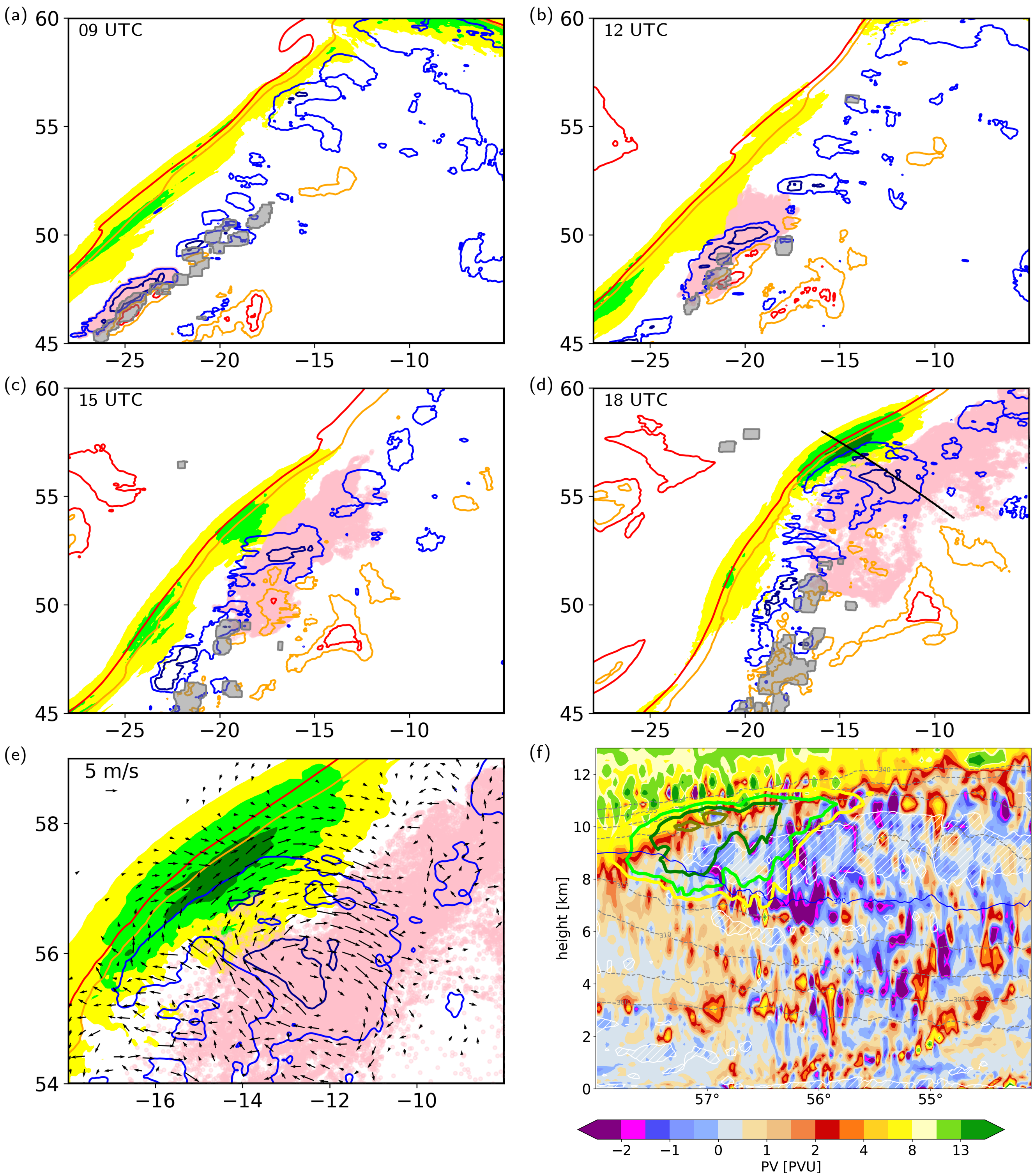

(a)
09 UTC
(b)
12 UTC
(c)
15 UTC
(d)
18 UTC
(e)
5 m/s
(f)
height [km]
57°
56°
55°
PV [PVU]

Figure 11. Spatially averaged upper-level PV at 320 K (dark blue, blue, orange and red contours at -1, 0, 1 and 2 PVU), upper-level jet at 320 K (yellow and green colors at 55, 60 and 65 $\mathrm{m\,s^{-1}}$) and envelope of rapid WCB ascent (grey contour and shading) at **(a)** 09 UTC, **(b)** 12 UTC, **(c)** 15 UTC and **(d)** 18 UTC 23 Sep 2016. The pink shading shows the positions of forward trajectories initialized in a region of convectively produced negative PV between 315 and 325 K at 09 UTC; **(e)** is an enlargement of **(d)** and additionally shows the 2-h circulation anomaly (black arrows); **(f)** Vertical cross-section along the line shown in **(d)** for PV (colors, in PVU), potential temperature (grey dashed lines, every 5 K), 320-K isentrope (blue line), and jet (yellow and green contours, at 55, 60, 65 and 70 $\mathrm{m\,s^{-1}}$). Low static stability layers ($\mathrm{d}\theta/\mathrm{dz} \leq 2\,\mathrm{K\,km^{-1}}$) are indicated by the white contour and hatching.

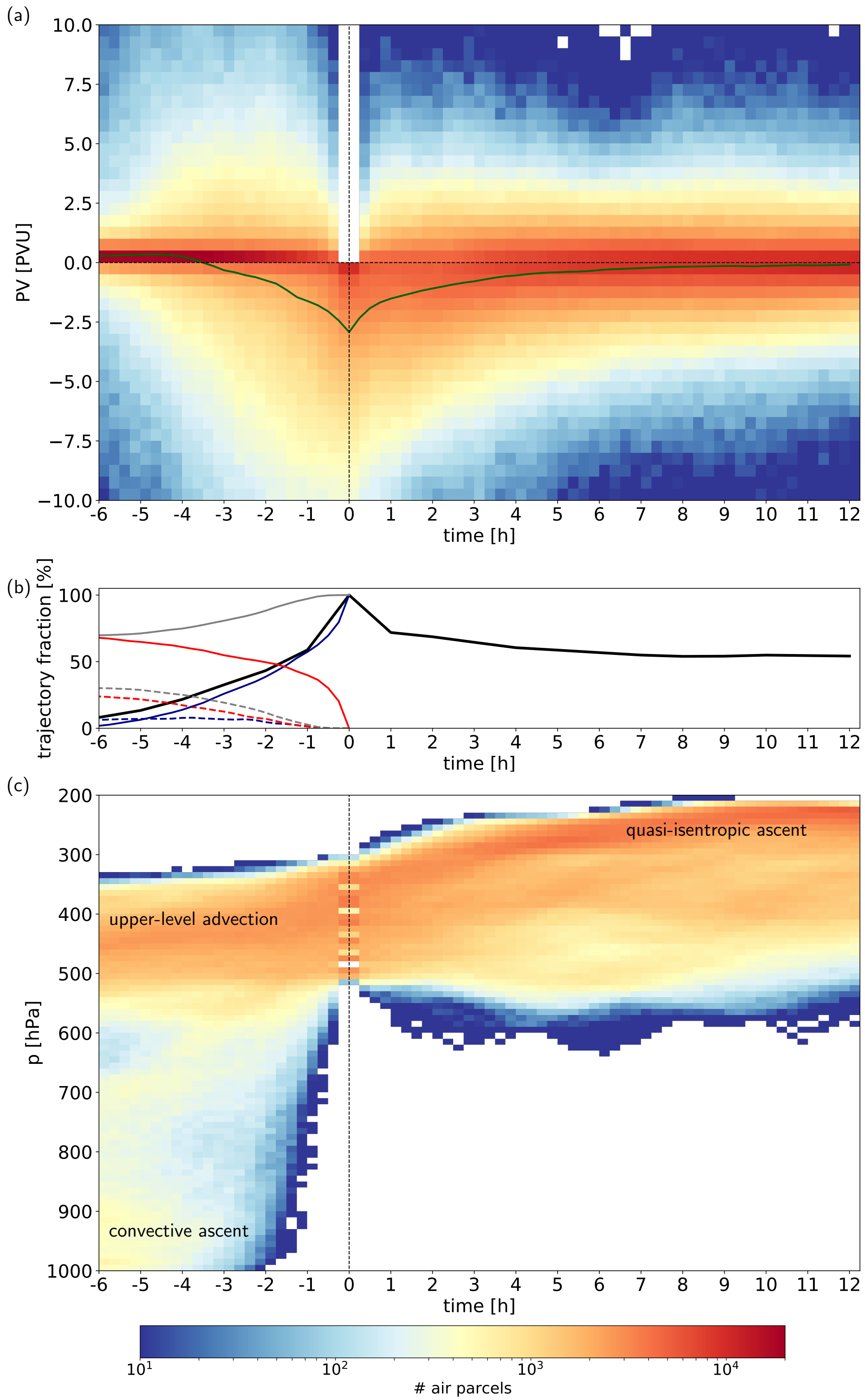
(a)
10.0
7.5
5.0
2.5
0.0
−2.5
−5.0
−7.5
−10.0
PV [PVU]
-6 -5 -4 -3 -2 -1 0 1 2 3 4 5 6 7 8 9 10 11 12
time [h]
(b)
trajectory fraction [%]
100
50
0
-6 -5 -4 -3 -2 -1 0 1 2 3 4 5 6 7 8 9 10 11 12
time [h]
(c)
200
300
400
500
600
700
800
900
1000
p [hPa]
upper-level advection
quasi-isentropic ascent
convective ascent
-6 -5 -4 -3 -2 -1 0 1 2 3 4 5 6 7 8 9 10 11 12
time [h]
10^1
10^2
10^3
10^4
air parcels

Figure 12. **(a)** 2D histogram of temporal evolution of PV (in PVU) for forward and backward trajectories initialized in a region of convectively produced negative PV between 315 and 325 K at 09 UTC as shown in Fig. 11a (pink shading). The time is given relative to the trajectory start at 09 UTC. The green line shows PV averaged over all trajectories (in PVU). **(b)** Fraction of trajectories with a negative PV value (black, in %), the fraction of trajectories located above 600 hPa (solid grey, in %) and below 600 hPa (dashed grey, in %). Additionally, the fraction of trajectories with negative PV above 600 hPa (blue solid, in %) and below 600 hPa (blue dashed, in %), as well as the fraction of trajectories with positive PV above 600 hPa (red solid, in %) and below 600 hPa (red dashed, in %) are shown. Note that after t=0 h the majority of trajectories is located above 600 hPa. **(c)** As **(a)** but for pressure (in hPa).

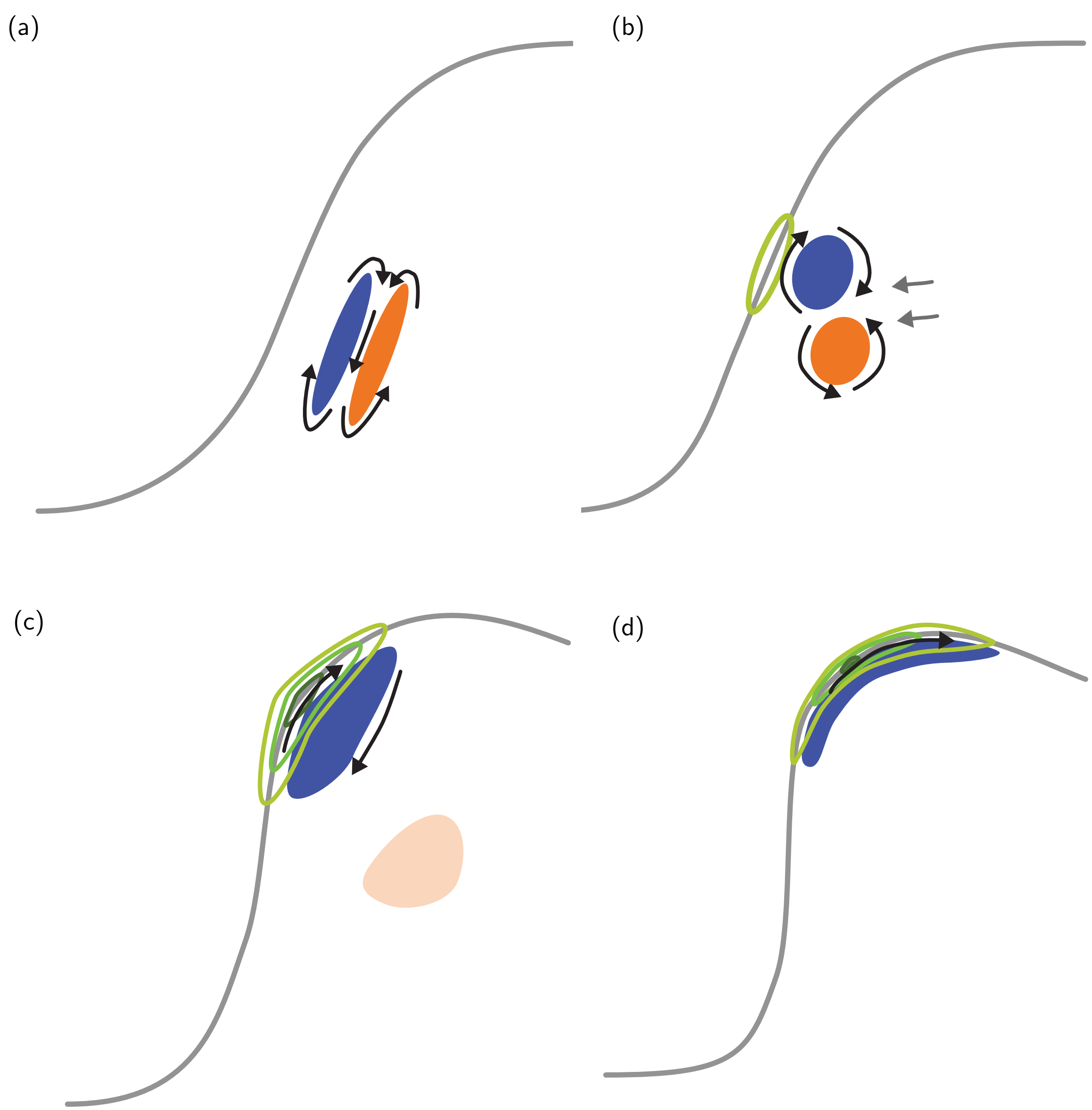

Figure 13. Schematic illustration of different stages of convectively generated PV (orange and blue colors for the positive and negative PV poles, respectively) and the associated jet structure (green contours); **(a)** PV dipole band; **(b)** meridional alignment; **(c)** distorted negative PV and weakend positive PV (light orange); **(d)** stretched negative PV band. See text for details.